A SEARCH FOR PROMPT LEPTON JETS IN THE ATLAS DETECTOR

by

Harisankar Namasivayam

APPROVED BY SUPERVISORY COMMITTEE:

Dr. Joseph M. Izen, Chair

Dr. XinChou Lou

Dr. Mustapha Ishak-Boushaki

Dr. Robert Glosser

Dr. Jason D. Slinker

This dissertation is dedicated to
my parents who brought me up with a curious mind,
and to my wife for her constant support and encouragement.

A SEARCH FOR PROMPT LEPTON JETS IN THE ATLAS DETECTOR

by

HARISANKAR NAMASIVAYAM, BE, MS

DISSERTATION

Presented to the Faculty of

The University of Texas at Dallas

in Partial Fulfillment

of the Requirements

for the Degree of

DOCTOR OF PHILOSOPHY IN

PHYSICS

THE UNIVERSITY OF TEXAS AT DALLAS

May 2015

ACKNOWLEDGMENTS

I would like to thank my advisor Dr. Joseph (Joe) Izen for supporting and advising me for the past five years. Joe is the most interesting advisor one can have. His knowledge and wittiness are the two main aspects that are hard to miss when working with him. Joe not only taught me physics, but also persistence and perseverance during hard times. Naively, at times I felt his workarounds and suggestions for finer details are taking too much of my effort, but the end results were always worth that effort.

My colleague Dr. Mahsana Haleem played a key role in my PhD research work by helping me understand the finer details of the ATLAS data, and by helping me learn the tools and software necessary for the analysis. She gracefully extended herself whenever I needed her expertise.

I thank my PhD committee for the time they took reading through my dissertation and for their support throughout my PhD processes.

I am grateful for the funding provided by the US Department of Energy (DOE) for my PhD work. I would also like to acknowledge my fellow ATLAS collaboration members for constantly verifying my research work and their suggestions for improvements.

Finally, I would like to thank my family members for their constant support and wishes: my wife, Aruna, for supporting me in my ups and downs and encouraging me to pursue what I love the most, Physics, and my parents, Namasivayam and Thaillammal, for their guidance and understanding throughout my life. Without them, this dissertation would not have happened.

March 2015

A SEARCH FOR PROMPT LEPTON JETS IN THE ATLAS DETECTOR

Publication No. ____________________

Harisankar Namasivayam, PhD
The University of Texas at Dallas, 2015

Supervising Professor: Dr. Joseph M. Izen

A search is performed for pairs of energetic lepton jets, which themselves are a collimated electron-positron(e^-e^+) or muon-antimuon($\mu^-\mu^+$) pair. The analysis is performed on the 20.3 fb^{-1} data collected with the ATLAS detector at the Large Hadron Collider (LHC) operating at a center-of-mass energy collision of 8 TeV. A proposed source of lepton jets is the decay of a Standard Model or a dark sector Higgs boson, producing dark sector gauge bosons (dark photons). Should dark photons mix kinetically with a virtual electromagnetic photons, could be detected through the virtual photon coupling to a boosted lepton-antilepton pair. Another possible source is found in supersymmetry(SUSY)-mediated models with decays to the dark sector that lead to lepton jets.

TABLE OF CONTENTS

LIST OF FIGURES

LIST OF TABLES

CHAPTER 1

THE STANDARD MODEL OF PARTICLES AND INTERACTIONS

The Standard Model of particles is a theoretical framework that explains the properties of fundamental and composite particles and their interactions. Fundamental particles in the Standard Model (SM) are point-like particles with no internal structure, while composite particles are made up of fundamental particles. The Standard Model successfully describes three out of the four know fundamental interactions of nature: electromagnetism, the weak force, and the strong force. A major limitation of the Standard Model is that it does not describe gravity.
All particles in the Standard Model fall into two categories, fermions and bosons. The fundamental fermions, shown in the first three columns in Figure 1.1 are half-integer spin particles. Fermions are half integer spin particles ($1/2\hbar, 3/2\hbar...$), and they obey Fermi-Dirac statistics. Gauge bosons and the Higgs are integer spin particle, and they obey Bose-Einstein statistics.

1.1 Standard Model

1.1.1 Fermions

Quarks and leptons, as well as composite particles such as protons and neutrons are fermions. Fundamental fermions come in three generations, they obey the Pauli Exclusion Principle and, therefore, no two identical fermions may occupy the same quantum state simultaneously.

<u>Leptons</u>
Leptons are fermions that are thought to be point-like particles with no internal structure. There are three charged leptons: electron (e), muon (μ), tau (τ) plus their corresponding antileptons. There are three neutral leptons(ν_e, ν_μ, ν_τ,) plus their corresponding antileptons. The electron (e^-), muon (μ^-) and tau (τ^-) have a charge of -1e (-1.6×10^{-19}C), while the positron (e^+), antimuon (μ^+) and antitau (τ^+) have a charge of +1e. Charged leptons participate in the electromagnetic and the weak interactions. Neutral leptons, the neutrinos are nearly massless and interact only through the weak interaction [31].

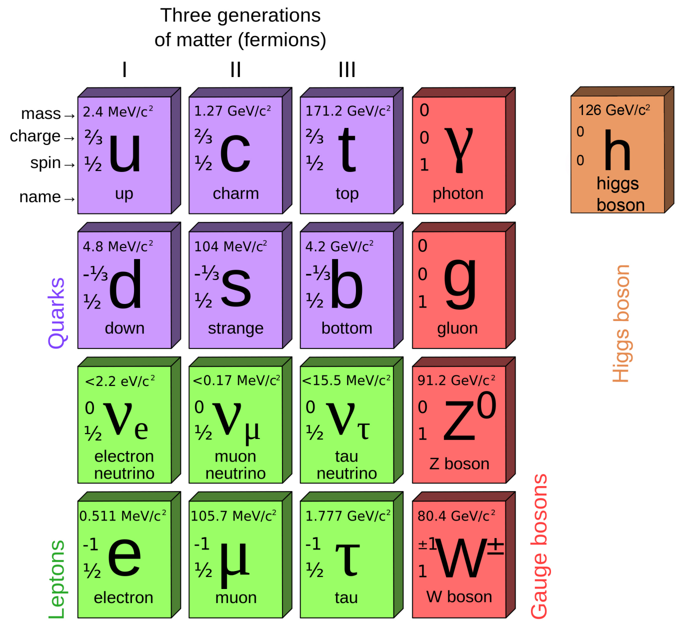

Figure 1.1. Fundamental particles and their classification in the Standard Model.

Table 1.1. Lepton masses.

Leptons	Mass MeV/c^2
Electron (e)	$m_e = 0.511$
Muon (μ)	$m_\mu = 105.6$
Tau (τ)	$m_\tau = 1776.8$

Quarks

Quarks are fermions and point-like particles. There are six quarks that are grouped into three generations [31]:

- First generation: up (u) and down (d)
- Second generation: charm (c) and strange (s)
- Third generation: top (t) and bottom (b)

Quarks carry a fractional electric charge and one unit of color charge (red, green, or blue). Quarks interact through the strong force in addition to the electromagnetic and the weak forces. Up, charm, and top quarks carry +2/3 times the charge of an electron, while down, strange and bottom quarks carry -1/3 times the charge of an electron. Quarks combine to form composite particles called hadrons. Most common hadrons are mesons and baryons. Quarks within the mesons and the baryons are bound by the strong force. A meson is made up of a quark-antiquark pair, and a baryon is made up of three quarks (or three antiquarks). Isolated quarks are not observed as they always bound together in color singlet states, *e.g.* red+green+blue in the case of baryons and red+antired, green+antigreen... in the case of mesons. A proton contains two up and one down quarks. The sum of the quarks' electric charges in a proton add up to +1 (+2/3 +2/3 -1/3 = 1), and the color charges in the quarks combine to make the proton a color singlet.

1.1.2 Boson

Gauge bosons

A gauge boson is a mediator for a fundamental interaction in nature. Each fundamental force has its own gauge boson(s) as listed in Table 1.2

Table 1.2. Fundamental interactions and their gauge bosons.

Fundamental Interactions	Gauge Bosons	Mass	Electric Charge	Range (m)	Spin
Electromagnetic interaction	Photon (γ)	0	0	$\frac{1}{r^2}$	1
Weak interaction	$W^{\pm}$ Z	$80.4 GeV/c^2$ $91.1 GeV/c^2$	$\pm$ 0	10^{-17}	1
Strong interaction	Gluons (8)	0	0	10^{-15}	1

Photons are massless and mediate electromagnetic interaction. The strength of the electromagnetic interactions follows inverse square law. The W and Z are massive and they mediate the weak interaction between left-handed component of fermions and right-handed component of antifermions. The range of the weak interaction is on the order of 10^{-17}m. Gluons are massless bosons that mediate the strong interaction between all color-charged particles (quarks). There are eight types of gluons in the strong interaction. The range of the strong interaction is limited to distances on the order of 10^{-15}m because of gluon self-coupling [51].

Higgs bosons

The Higgs boson is a fundamental particle in the SM. It is a spin-0 boson with no charge. It was the most elusive component of the SM, and it was only discovered at the Large Hadron Collider (LHC) in 2012. Unlike gauge bosons, the Higgs boson is not a force carrier. Through the Higgs mechanism [46, 52] the Higgs boson gives mass to all fundamental fermions and the W and Z bosons.

1.2 Limitations of the Standard Model

The Standard Model of particle physics presents a remarkably comprehensive explanation of particle phenomena up to scales of a few-hundred GeV, but it is not the "Theory of Everything" that physicists strive to determine. Limitations of the SM provide motivation for searching for physics Beyond the SM (BSM). The SM also fails to describe the non-luminous dark matter that is detected gravitationally on galactic and super-galactic scales. Luminous matter composed of protons, neutrons and electrons comprised only 15% of the mass of galaxies. Beyond the Standard Model (BSM) theories attempt to patch the SM. This work reports the result of a search for a possible signature of a force between dark matter particles.

CHAPTER 2

DARK MATTER

2.1 Dark Matter and its Astronomical Observation

Dark matter is believed to account for nearly 27% of the universe, while dark energy constitutes for 68% and visible stuff like stars and galaxies constitute for the remaining 5% [61]. Dark matter is thought not to participate in the electromagnetic force and the strong force, but it may interact through the weak force. The existence of dark matter is inferred through its gravitational interaction.

2.1.1 Galactic rotation curves

In the 1930s Fritz Zwicky observed the speed of galaxies around the center of the cluster of galaxies[68]. He observed that the speed of the galaxies at the outer edge of the cluster is faster than what he had calculated. His calculations used the total mass of the visible matter within the cluster. He hypothesized that there was non-luminous dark matter present within galactic clusters.

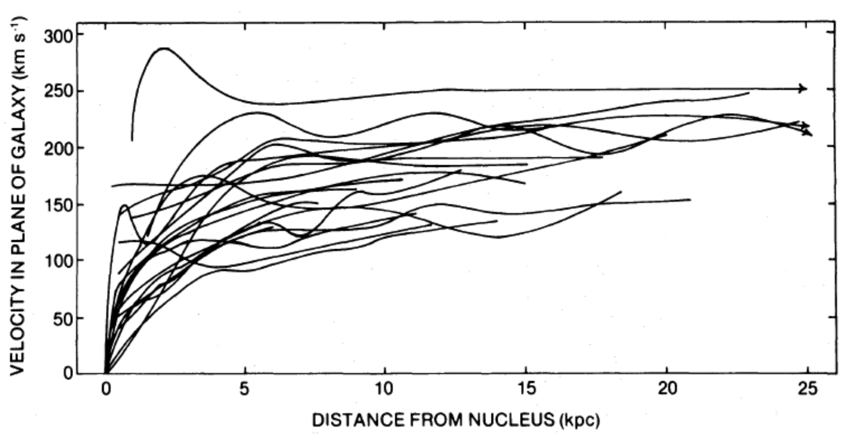

Figure 2.1. Rotations curve of a 21 Sc galaxies. [67]

Later in the 1960s and 1970s, Vera Rubin *et.al.* showed that stars in the outer edge of spiral galaxies have almost the same velocities of stars present near the center of the galaxy

[67]. Figure 2.1 from [67] shows the rotation curves of 21 Sc galaxies. As the distance from the nucleus increases the velocity of stars stays constant. This provides evidence for the existence of dark matter within galaxies.

2.1.2 Galaxy clusters and gravitational lensing

According to general relativity, a massive object distorts space. When light travels past a massive object(s), that massive objects gravitational field deflects it. The bending of light rays by a massive object is known as 'gravitational lensing'. Lensing is illustrated in Figure 2.2, where the massive object bends light from a distant quasar en route to an observer creating multiple images in characteristic arcs.

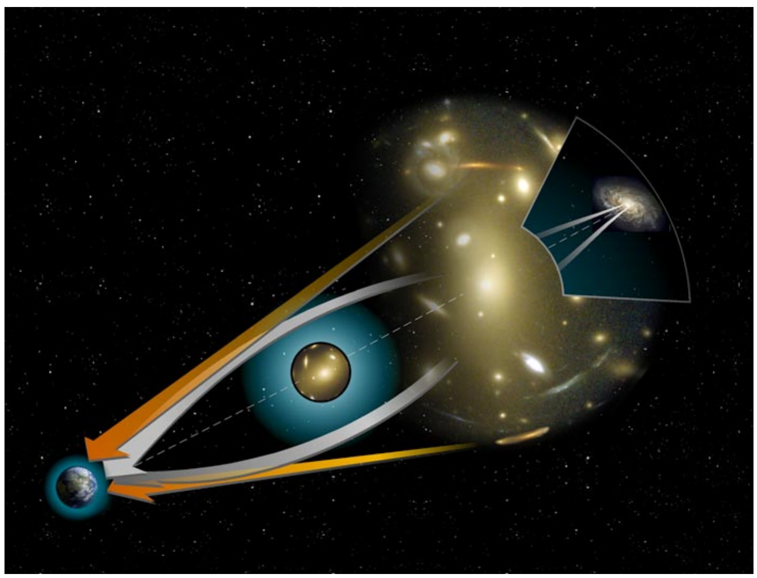

Figure 2.2. Gravitational lensing. Bending of light rays in a distorted space-time fabric

Since the amount of bending of light depends on intervening mass, the mass can be calculated using gravitational lensing [53]. Gravitational lensing is sensitive to the mass of luminous matter, dust, and the mass of dark matter in galaxies or clusters of galaxies.

2.1.3 Collisions of galactic clusters

The Bullet Cluster consists of two colliding clusters of galaxies. Figure 2.3 shows the Bullet Cluster, where two clusters of galaxies collided. The red hue represents the distribution of dust and gas in the clusters as detected by Chandra X-ray telescope, and the blue hue represents the distribution of dark matter, which has been measured using gravitational lensing. Gravitational lensing studies of the Bullet Cluster provide evidence for the existence of dark matter [57]. When two clusters of galaxies collide, the stars in those galaxies are not greatly affected by the collision due to their sparse distribution, and most of them pass undisturbed. The dust in the galaxies is distributed and interacts through gravity and electromagnetism. It is slowed much more than the stars. Dark matter appears to interact only through gravity, and perhaps through the weak interaction, or perhaps unknown weak dark-sector interaction that are not affected by the collision and pass right through without any hindrance. [57]

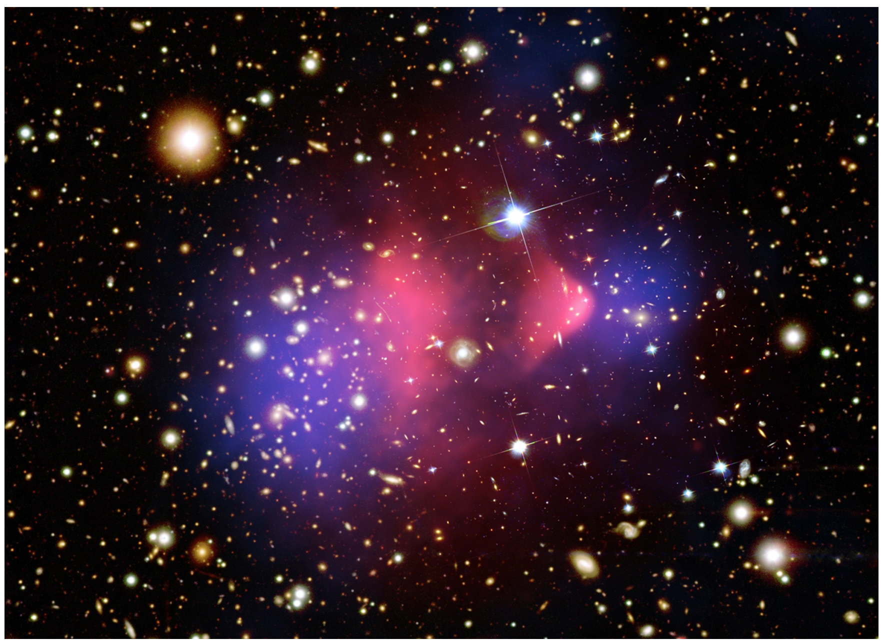

Figure 2.3. Bullet cluster after collision. [59]

2.1.4 Data from satellite borne experiments

Experiments like the Payload for Antimatter Matter Exploration and Light nuclei Astrophysics (PAMELA) [60] and the Alpha Magnetic Spectrometer [17] show signals that may be attributed to the existence of dark matter. The PAMELA experiment is a satellite-based experiment dedicated to the detection of cosmic rays, with a particular focus on the antimatter components in the cosmic rays. The Alpha Magnetic Spectrometer (AMS-02) is a satellite-borne experiment based at the International Space Station. The AMS uses the atmosphere-free environment of space to study the universe and its origin by searching

for antimatter and dark matter, while performing precision measurements of cosmic rays composition and flux [17].
The PAMELA experiment observed excess positrons compared to the know sources. Antiproton to proton ratio measurements (Figure 2.4a) show no excess of antiprotons [13].

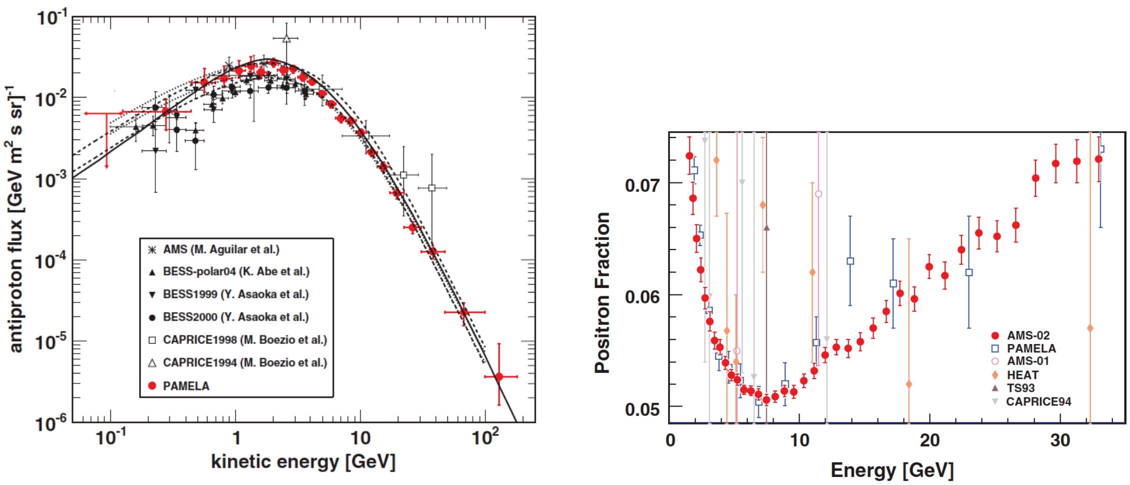

(a) (b)

Figure 2.4. (a) The PAMELA observation of no excess of anti-proton flux as expected from the know sources. (b) Measurement of the rise of the fraction of positron compared to the total electron and position above 8 GeV from the AMS experiment.

The AMS experiment also observed an excess of positrons (Figure 2.4b) compared to the expectation from known sources like nuclei interactions in the interstellar medium. [19] [18]. If dark sector particles interact with the SM particles through a kinetic mixing term, as discussed in Chapter 4, the dark sector particle's mass would have to be more than twice the electron mass and less than twice the proton mass to be kinematically consistent with the PAMELA measurement.

CHAPTER 3

EXPERIMENTAL APPARATUS

3.1 Large Hadron Collider (LHC)

The Large Hadron Collider (LHC) is a proton-proton collider, situated on the Swiss-French border and operated by CERN. The collider tunnel is 27 km in circumference, and it is located 100m below the surface of the Earth. Two beams of protons bunches, circle in opposite directions in the LHC rings. These proton bunches are collided at four points in the LHC tunnel where detectors are located. The four detectors in the LHC are, ATLAS [1], CMS [38], ALICE [15], and LHCb [56]. ATLAS (A Toroidal LHC ApparatuS) and CMS (Compact Muon System) are general-purpose detectors with a broad physics program. ALICE (A Large Ion Collider Experiment) is optimized for observing heavy ions collisions where track density is high, and LHCb is optimized for B meson physics. My research work is based on the data collected with the ATLAS detector during 2012 in which the Large Hadron Collider (LHC) was operating at a center-of-mass energy $\sqrt{s} = 8$ TeV.

3.1.1 LHC operations in 2012

The LHC is designed to collide proton bunches at $\sqrt{s} = 14$ TeV with as many as 2808 bunches of protons in a ring, circulating in each direction. Each bunch has $\approx 10^{11}$ protons and are designed to collide at the center of a detector at 25 ns interval. However, starting from the year 2009, LHC increases its collision energy from 2.36 TeV to 8 TeV in three years. The amount of data collected by the detectors in the collider experiment is denoted by the term Luminosity $\mathcal{L}$. The luminosity of a collider can be expressed as

$$\mathcal{L} = \frac{n_b f_r n_1 n_2}{2\pi\sigma_x\sigma_y} \tag{3.1}$$

where n_1 and n_2 are the numbers of particles in the two colliding bunches, σ_x and σ_y characterize the widths of the horizontal and vertical beam profiles, f_r is the revolution frequency and n_b is the number of bunches cross the interaction point [26].

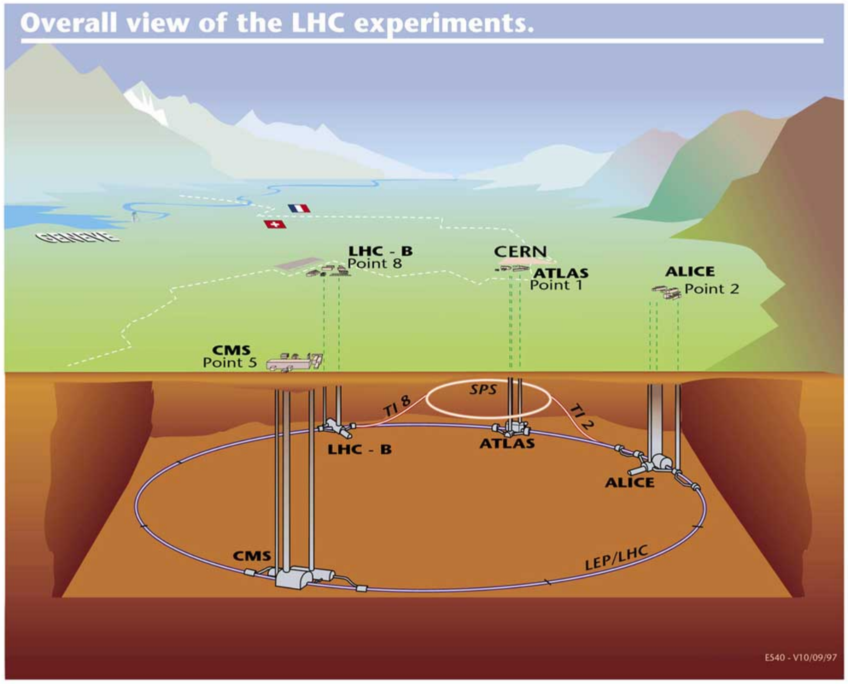

Figure 3.1. Underground LHC ring and the location of the four main detectors.

The LHC's operating condition during the 2012 data taking period is shown in Table 3.1. The total integrated luminosity delivered by the LHC and collected by the ATLAS detector are shown in Figure 3.2

Table 3.1. Operating conditions of the LHC during 2012 data taking period.

Parameters	Values
$\sqrt{s}$ $[TeV]$	8
Number of colliding bunches	1380
Bunch spacing [ns]	50
Peak stable luminosity $[cm^{-2}s^{-1}]$	7.73×10^{33}
Maximum events per bunch crossing	70

Pile-up

Number of interactions per bunch crossing is called pile-up. Figure 3.3 shows the distribution of the number of interactions per bunch crossing for the 2011 and 2012 data taking periods. The mean number of interactions per crossing is calculated from the instantaneous per bunch luminosity as $\mu = \mathcal{L}_{bunch} \times \sigma_{inel}/f_r$ where $\mathcal{L}_{bunch}$ is the per bunch instantaneous luminosity,

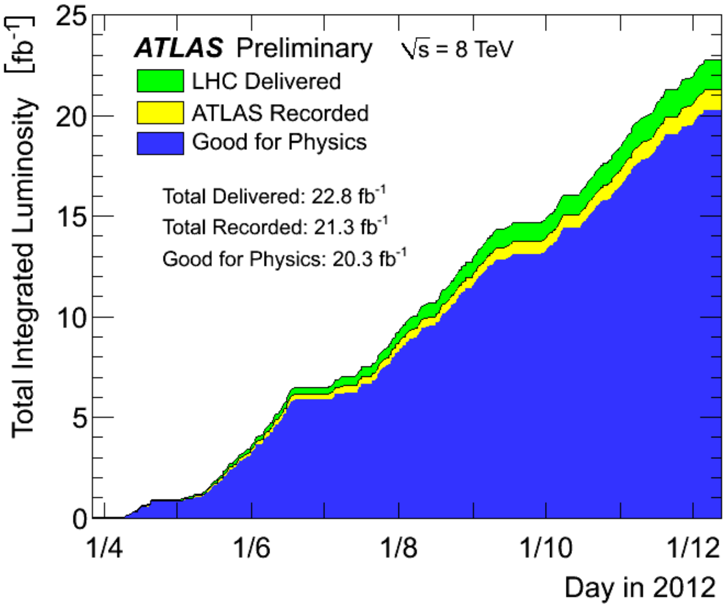

Figure 3.2. Total integrated luminosity delivered by LHC (green), recorded by ATLAS (yellow), and after selecting good quality data for physics analyses (blue) in 2012

σ_{inel} is the inelastic cross section which was taken to be 71.5 millibarn (1 barn = $10^{-24}cm^2$) for 7 TeV collisions and 73.0 millibarn for 8 TeV collisions.

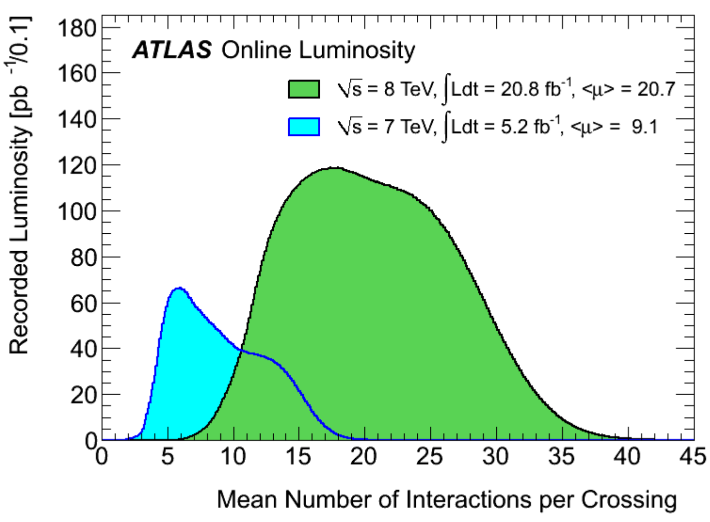

Figure 3.3. Average number of interactions per bunch crossing in 2011 at $\sqrt{s} = 7\ TeV$ and in 2012 at $\sqrt{s} = 8\ TeV$ data taking periods.

3.2 ATLAS Detector

3.2.1 Overview

The ATLAS is the largest detector at the Large Hadron Collider, with a width of $42m$ and a height of $25m$. ATLAS weighs nearly 7000 tons. The layers of the ATLAS detector are nested like the layers of an onion with complete 4π steradian solid angle coverage. The ATLAS detector is comprised of tracking system, calorimeters, magnet system, and muon system.

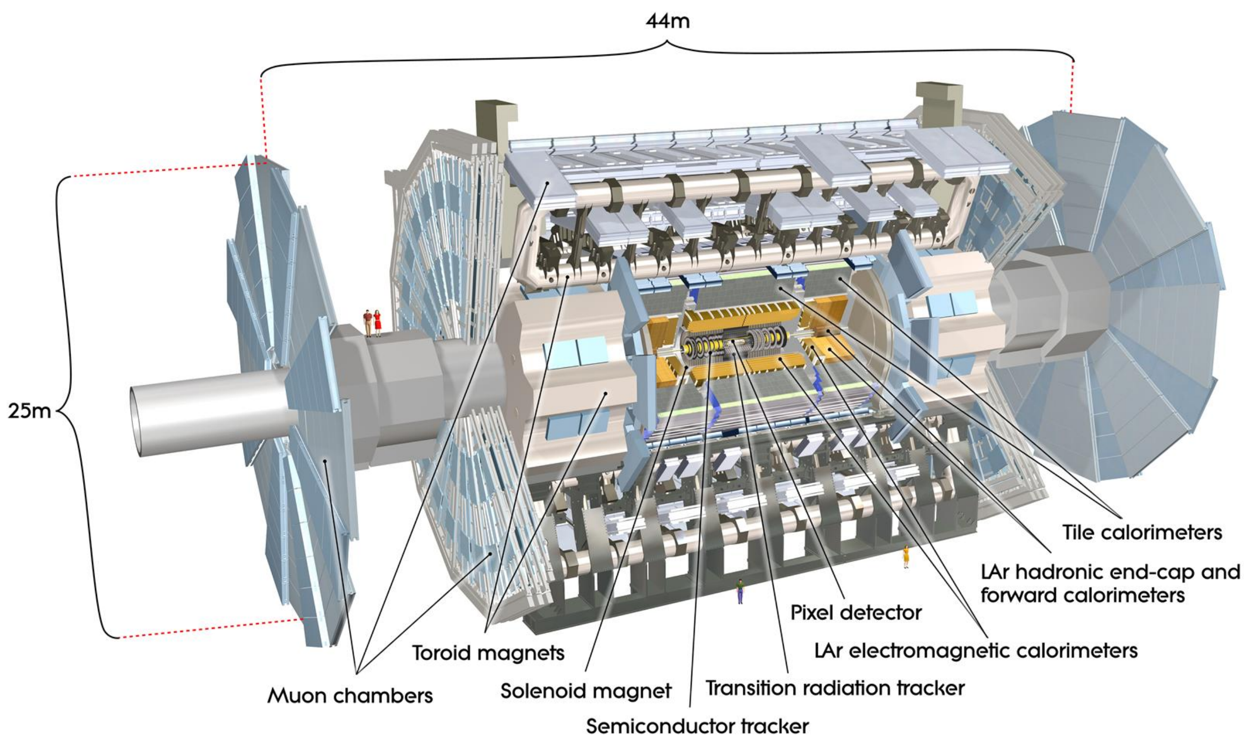

Figure 3.4. The ATLAS Detector

3.2.2 Tracking System

The innermost layers of the ATLAS are for charge particle tracking, they are collectively known as Inner Detector (ID) with three sub detectors; the Pixel detector, the Semiconductor Tracker (SCT), and the Transition Radiation Tracker (TRT). The ATLAS inner detector is designed to provide hermetic coverage, excellent tracking resolution, excellent momentum resolution, and vertex resolution [1]. The inner detector is positioned within the cylinder of a 2T solenoidal magnet. The dimensions of each sub-detector are listed in Table 3.2. Figure 3.5 shows a detailed view of the inner detector in the barrel region. [1]

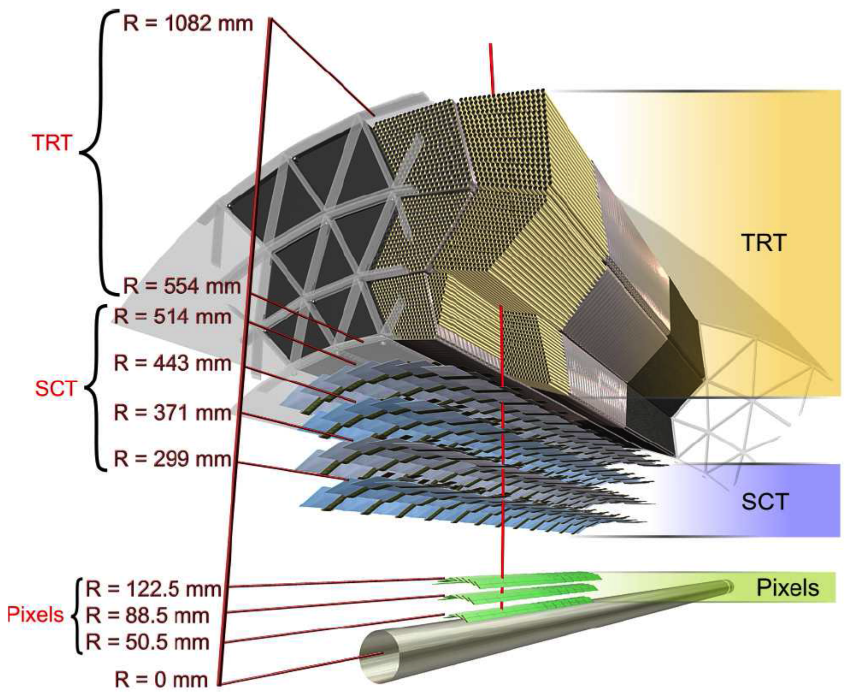

Figure 3.5. Detailed layer view of the inner detector, and their distance from the center of the beam pipe.

<u>Pixel Detector</u>

The Pixel Detector contains a total of 1744 silicon pixel modules arranged in three concentric barrel layers and two end caps of three disks each. Each module contains 47232 pixels, where the size of the pixels are $50 \times 400 \mu m$. The Pixel detector extends radially from 45.5 mm to 242 mm and from -3092 mm to +3092 mm in the z[1] direction. In the barrel, 3 cylindrical layers are located at radial positions of 50.5 mm, 88.5 mm, and 122.5 mm (Figure 3.5). The Pixel detector typically provides three measured space points along the path of charged particles originating in the beam-interaction region. When a charged particle traverses the Pixel detector, it ionizes the semiconductor and the ionization charges are collected by the readout electronics, which are bump bonded with the silicon. The total number of readout channels for the Pixel detector is 80.4 million. [24]

[1] z axis points along the direction of the proton beams.

Table 3.2. Inner detector dimensions.

Items	Radial extension (mm)	Length (mm)
Overall ID envelope	$0 < R < 1150$	$0 < \|z\| < 3512$
Beam-pipe	$29 < R < 36$	
Pixel	$45.5 < R < 242$	$0 < \|z\| < 3092$
SCT	$255 < R < 549$ (barrel)	$0 < \|z\| < 805$
	$251 < R < 610$ (end-cap)	$810 < \|z\| < 2797$
TRT	$554 < R < 1082$ (barrel)	$0 < \|z\| < 780$
	$617 < R < 1106$ (end-cap)	$827 < \|z\| < 2744$

Semi-Conducting Tracker (SCT)

The SCT detector contains a total of 4088 modules of silicon-strips arranged in four concentric barrels and two end caps of nine disks each. The SCT detector extends radially from 255 mm to 549 mm and from -2797 mm to +2797 mm in the z direction. The SCT detector typically provides eight measured space points (each layer has two semiconductor strips) along the path of charged particles originating in the beam-interaction region. When a charged particle traverses through the SCT, it ionizes the semiconductor and the strips collect the ionization charges. Front-end chips read out the signal. Each chip reads out 128 channels. The total number of readout channels is 6.3 million. [24]

Transition Radiation Tracker (TRT)

The TRT detector consists of 298304 drift tubes (straws). Each straw is 4 mm in diameter. The overall dimension of the TRT extends radially from 554 mm to 1106 mm and from -2744 mm to +2744 mm in the z direction. The anode (central wire) in the tube is electrically split in the middle by an insulating material and each end is readout independently. This arrangement reduces the occupancy of the TRT tubes [1] [24]. Tubes of the TRT are filled with 70% Xe, 27% CO_2 and 3% O_2. The spaces in between the tubes are filled with polypropylene fibers that serve as a transition radiation material. The cathode and the anode in each tube are maintained at a potential difference of 1530V to give a gas gain 2.5×10^4 for the chosen gas mixture. When an electron traverses through the Transition Radiation Tracker, it radiates photons and these photons along with the electron ionize the gas in the tube. When any other charged particle traverse through the TRT it ionizes the gas and hardly radiates. The ionization charges liberated due to ionization in the gas drift towards the anode and are collected. Based on the collected charges from each tube, the

TRT hit is classified as a low threshold (LT) or a high threshold (HT) hit. [24]. For an electron, the fraction of high threshold hits (f_{HT}) is higher than any other charged particles, *e.g.* pions.

$$f_{HT} = \frac{Number\ of\ high\ threshold\ hits\ in\ the\ TRT}{Total\ number\ of\ hits\ in\ the\ TRT}$$

The tracking system provides a position resolution of 10, 17 and 130 μm (in $R - \phi$ plane) in the Pixel, SCT and TRT respectively.

3.2.3 Magnets

The ATLAS magnets (Figure 3.6) consist of a central solenoid, a barrel toroid magnet and two end cap toroids. The magnet system is 26m long and with a diameter of 20m. The central solenoid is 5.3m long and 2.4m in diameter. It provides a magnetic field of 2T to the inner detector, and the field is parallel to the z-axis. The coil mass is 5.4 metric tons, and its stored energy is 0.04 GJ.

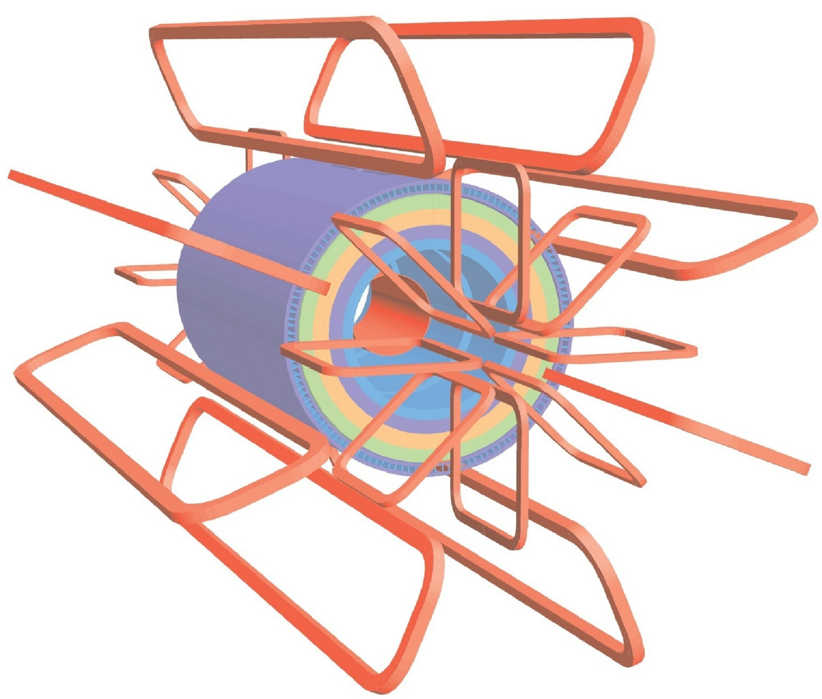

Figure 3.6. ATLAS magnets. The solid structure at the center is the central solenoid and the outer rings are the eight toroidal windings.

The toroid magnet system has one barrel toroid and two end-cap toroids at each end of the solenoid. The toroids generate a magnetic field for the muon system, and the field runs along the circular direction of the cylinder. The magnetic field of the barrel toroid and the end cap toroids is 4T. The barrel toroid consists of eight coils encased in individual stainless-steel vacuum vessels. Eight inner and eight outer rings of struts support the coil assembly. The total mass of the barrel and end cap toroid system is 550 metric tons, and its stored energy is 1.58 GJ.

3.2.4 Calorimeter System

The calorimeter system is the next layer in the ATLAS detector situated outside the tracking system. The calorimeter system is comprised of two sections: the Electromagnetic Calorimeter and the Hadronic Calorimeter.

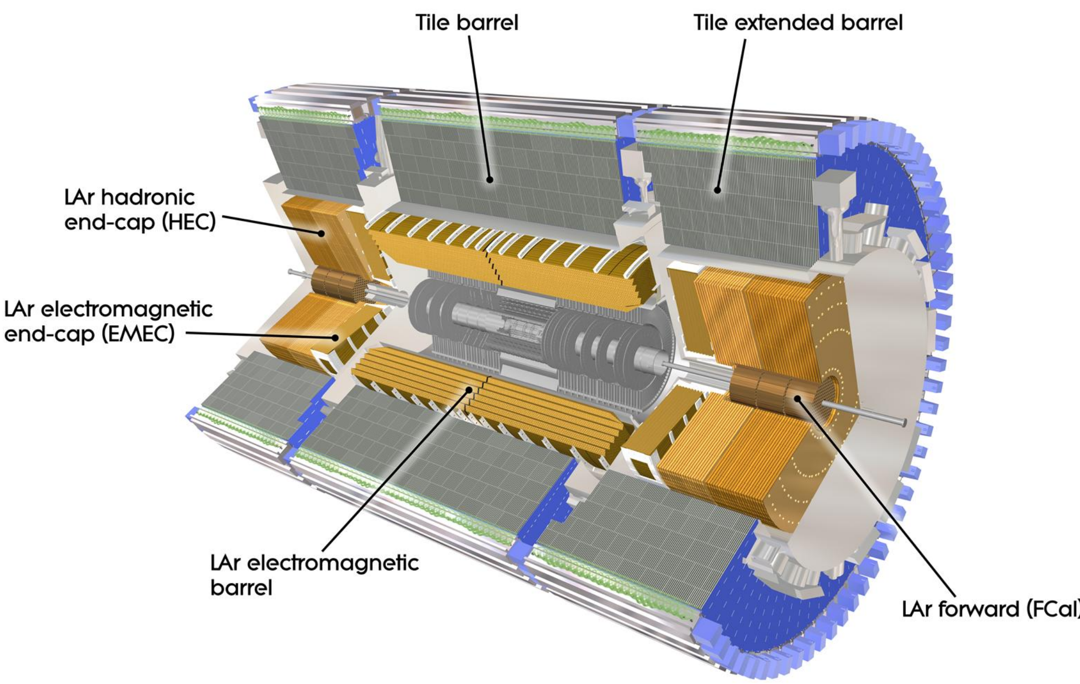

Figure 3.7. ATLAS electromagnetic calorimeter and hadronic calorimeter.

The electromagnetic (EM) calorimeter contains accordion-shaped layers of lead absorber, immersed in liquid argon (LAr). When electrons or photons reach the electromagnetic calorimeter, they interact with the absorber material and produce more electrons, positrons, and photons. These secondary electrons, positrons, and photons ionize the LAr and the calorimeter electrodes collect the charges. This process of producing secondary particles that then ionize the liquid continues until the primary energetic electron stops in the calorimeter. This is known as showering (Figure 3.8). By measuring the ionization charge collected by the electrodes, it is possible to deduce the energy of the original electron.

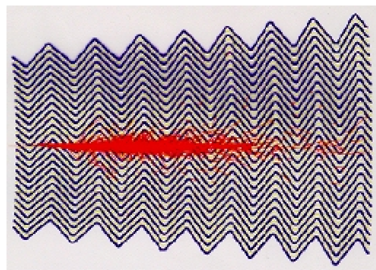

Figure 3.8. Showering in the electromagnetic calorimeter.

The electromagnetic calorimeter (shown in Figure 3.7) is composed of sampling electrodes with full azimuthal symmetry. The pseudorapidity range of the full electromagnetic calorimeter is $|\eta| < 3.2$ (where $\eta = -log(tan\frac{\theta}{2})$). For $|\eta| < 1.8$, a presampler, with an active LAr layer installed directly in front of the electromagnetic calorimeter, provides a measurement of the energy from showering induced as photons and electrons traverse the inner detector. A Liquid Argon electromagnetic end cap calorimeter is located on either side of the ID. The electromagnetic calorimeter is segmented into cells in the η and ϕ directions (Figure 3.9), and each cell is read out separately. The total thickness of the EM calorimeter is > 24 radiation lengths (X_0) in the barrel and $> 26X_0$ in the end-caps.
The hadronic (or tile) calorimeter surrounds the electromagnetic calorimeter, as shown in Figure 3.10. It is made up of plastic scintillator as the active material and steel as the absorber with full azimuthal symmetry. The hadronic calorimeter covers the pseudorapidity region $-1.7 < \eta < 1.7$. It contains the central long barrel (LB), in the region ($-1.0 < \eta < 1.0$) and the two extended barrels (EB) on both sides ($0.8 < |\eta| < 1.7$) of the central barrel, as shown in Figure 3.7. Both the barrel and the extended barrel cylinders are segmented into 64 modules in ϕ, corresponding to a $\Delta\phi$ granularity of 0.1 radians. The $\Delta\eta$ segmentation for each module is 0.1 in the first two radial layers and 0.2 in the third layer. The ϕ, η and radial segmentation define the three dimensional calorimeter cells. Each cell volume is made of dozens of iron plates and scintillating tiles. Fiber optic cables on either ϕ edge of the scintillating tiles collect light and are read out through light guides by photomultiplier tubes (PMTs) (Figure 3.10).

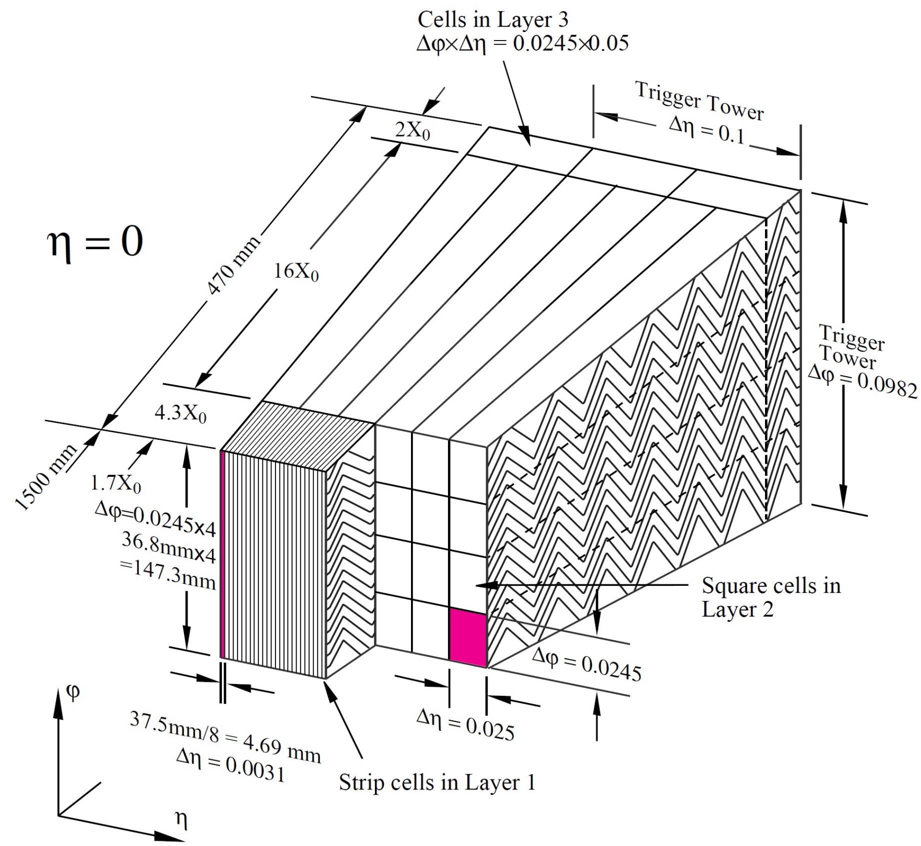

Figure 3.9. Cutaway view of the electromagnetic calorimeter.

Resolution of the calorimeter system improves with energy. With every increase in the energy of the cluster, the resolution in measuring its energy gets better.

3.2.5 Muon System

The muon system forms the outer layer of the ATLAS detector. Precision-tracking chambers in the barrel region are located within the field of the eight coils of the superconducting barrel toroid magnet. The end-cap chambers are in front and behind the two end-cap toroid magnets. The chambers in the barrel are arranged in three concentric cylindrical shells around the beam axis at radii of approximately 5 m, 7.5 m, and 10 m. In the two end-cap regions, muon chambers form large wheels, perpendicular to the z-axis and located at distances of $|z| \approx 7.4$ m, 10.8 m, 14 m, and 21.5m.

Monitored Drift Tube (MDT) chambers perform a precision momentum measurement. The pseudorapidity range of MDT is $|\eta| < 2.7$. The MDT chambers consist of three to eight

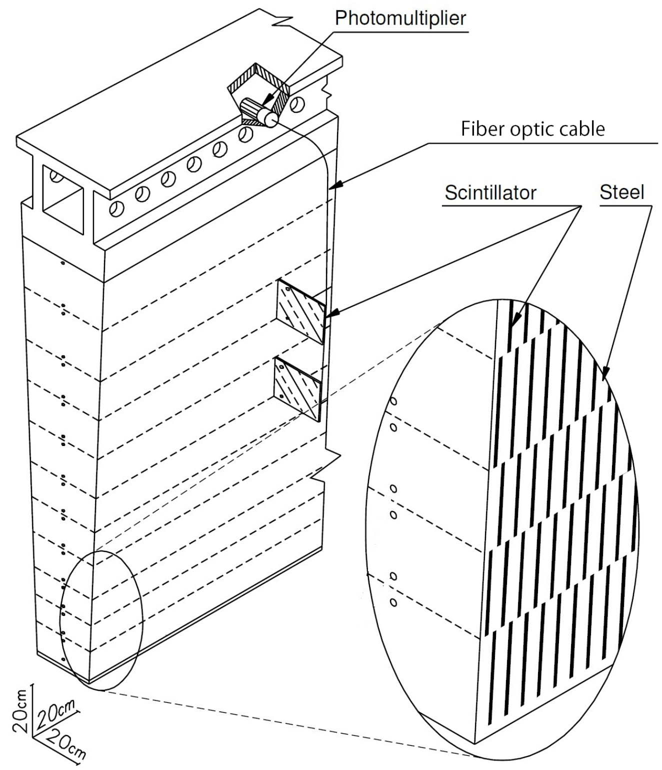

Figure 3.10. Cutaway view of the hadronic calorimeter.

layers of drift tubes, and offer an average spatial resolution of $80\mu m$ per tube in the $R-\eta$ plane. In the forward region ($2 < |\eta| < 2.7$), Cathode-Strip Chambers (CSC) are used. The CSCs are multi-wire proportional chambers with cathode planes segmented into strips in orthogonal directions. The resolution of a chamber is $40\mu m$ in the $R-\eta$ plane. The precision-tracking chambers have been complemented by a system of fast trigger chambers capable of delivering track information within a few tens of nanoseconds after the passage of the particle. In the barrel region ($|\eta| < 1.05$), Resistive Plate Chambers (RPC) are used, while in the end-cap ($1.05 < |\eta| < 2.4$) Thin Gap Chambers (TGC) are used. Both chambers deliver signals within $1525ns$, thus providing the ability to tag the beam-crossing.

Muons are the only particle that reach the muon system. Electrons and photons lose almost all their energy in the electromagnetic calorimeter. Hadrons lose their energy in the hadronic calorimeter.The toroid magnets provide magnetic field to the muon spectrometer in the ϕ direction, circle around the detector like a cylinder.

Figure 3.11 shows an 8 TeV collision in the ATLAS detector. The top left section of the plot shows the transverse plane of the detector with tracks emerging from the center interaction point. The two yellow lines are the muons reaching the muon system. The bottom section of the plot shows the zoomed in lengthwise view of the detector at the interaction point, where multiple interaction (pileup) of the protons or vertices are visible.

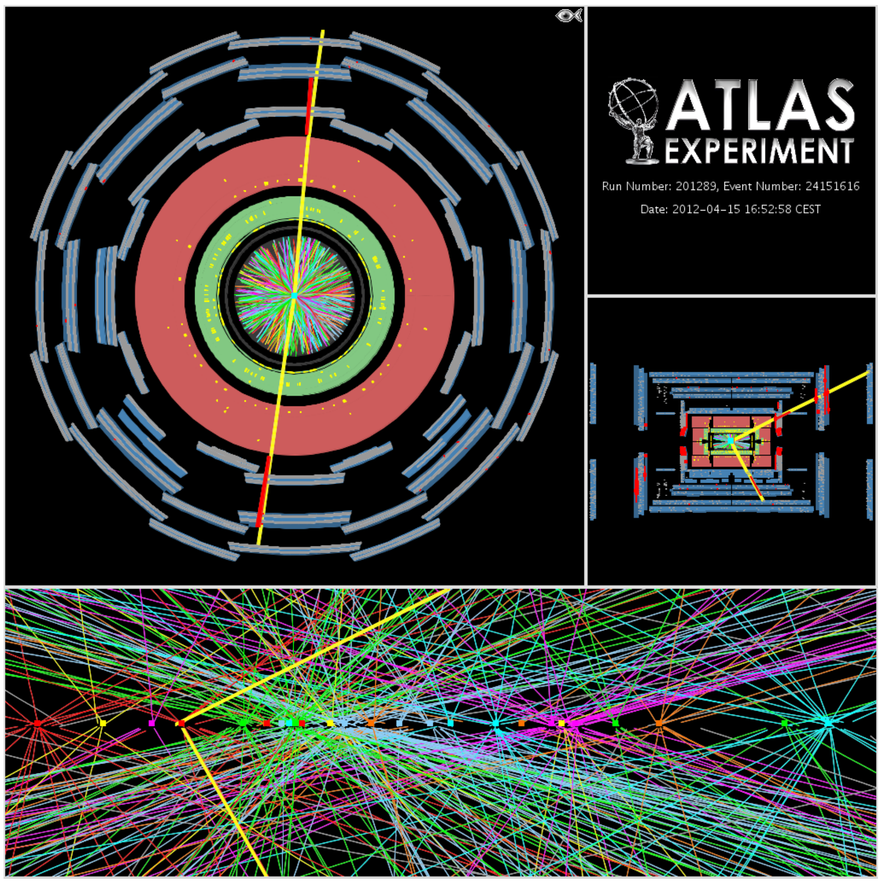

Figure 3.11. A 8 TeV proton-proton collision with nearly 20 interactions per bunch crossing.

3.3 Trigger and Data Acquisition

The ATLAS is designed for a collision rate of 40MHz with a bunch spacing of 25ns. Handling this enormous event rate is the primary task of the trigger and data acquisition software. Trigger and data acquisition system efficiently chooses the physics events and rejects uninteresting events. The main task of ATLAS trigger logic is to reduce the event rate from 40MHz to 200Hz.

The trigger system consists of three levels. Level-1 is a hardware trigger, which depends on calorimeter and muon spectrometer information. Level-1 has a latency of 2.5 microseconds. The event rate is reduced to a maximum of 75 KHz. If the event is accepted, the Level-1 data is added to the readout stream through dedicated Read-Out Drivers (RODs). In addition to performing the initial selection step, the Level-1 trigger identifies Regions of Interest (RoIs) within the detector to be investigated by the High Level Trigger (HLT).

The High Level Trigger (HLT) is a software trigger and it is a combination of the Level-2 trigger and the Event Filter (EF). When an event is accepted by the Level-1 trigger, data from each sub-detector is transferred to the detector-specific Readout Buffers (ROB). As the processing time of Level-2 triggers is higher than the collision rate, an event which pass the Level-1 trigger has to be buffered while the Level-2 triggers processes it. One or more Readout buffers are grouped into Readout Systems (ROSs), which are connected to the High Level Trigger network. The Level-2 selection is based on fast custom algorithms that process the event data within the Region of Interest identified by the Level-1. The Level-2 trigger algorithm reconstructs the momentum of tracks and the energy of showers in the calorimeters. The Level-2 triggers reduce the output rate to 3 kHz with an average processing time of 40 ms/event.

The event builder assembles all event information from the readout buffers for events accepted by the Level-2 trigger to the Event Filter (EF). The Event Filter has complete event information and can determine parameters like the missing energy of an event. The event filter is designed to reduce the rate from 3kHz to 200 Hz [25]

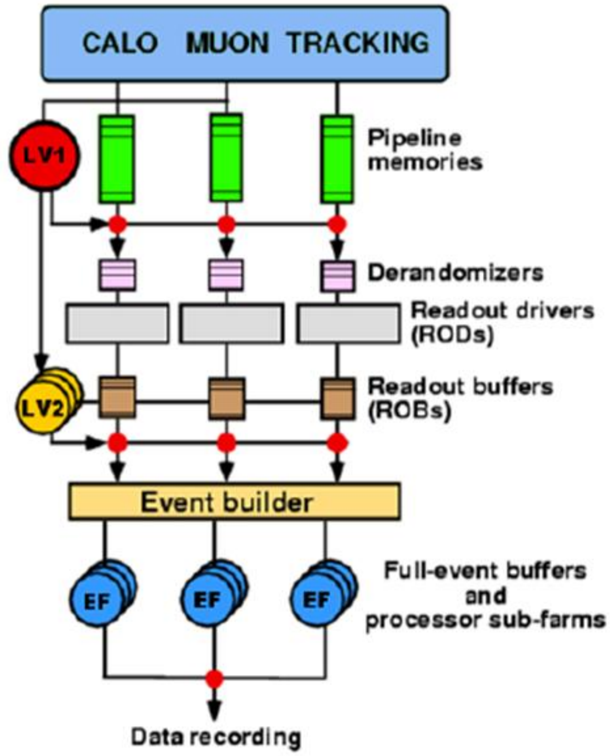

Figure 3.12. ATLAS trigger system. [25]

CHAPTER 4

DARK MATTER IN THE LARGE HADRON COLLIDER

In this chapter, a class of well-motivated dark sector theories that accounts for the existence of dark matter is discussed. The theories also describe dark matter production mechanisms in the LHC and how it can be detected in the ATLAS detector.

4.1 Dark Sector Theory

The existence of dark matter is supported by several direct and indirect experiments [6, 9, 12, 18, 19, 20, 28, 32, 36]. Theories [22, 23] of dark matter are motivated by the unexpected excess of cosmic-ray positron at high energies [9, 12, 18, 19, 28]. Several dark sector models[11, 29, 37, 48] are proposed exploiting the theory that predict signatures, which can be tested at the Large Hadron Collider (LHC). The dark sector, through its dark gauge boson, the dark photon γ_d, kinetically mixes with the Standard Model photon through the kinetic mixing parameter ϵ [54], as shown in Figure 4.1. This work considers two sets of theories providing explanations of how dark particles can be produced in the LHC, one through Supersymmetric (SUSY) portal (Section 4.1.2), and the other through the Higgs portal (Section 4.1.3).

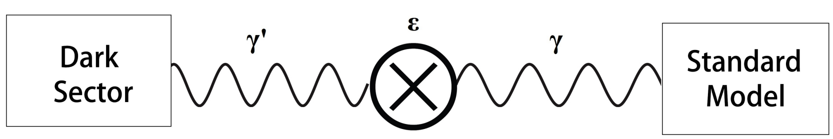

Figure 4.1. Coupling between dark sector and the Standard Model through the kinetic mixing parameter ϵ.

In this work, a search for dark photons decaying promptly to a pair of electron-positron or muon-antimuon is performed. The search uses the ATLAS data collected during the 2012 data taking period, where the center-of-mass energy of the collision $\sqrt{s} = 8$ TeV. A prompt decay within few nanoseconds in the rest frame of the dark photon after its production implies the kinetic mixing parameter, ϵ, lies typically above 10^{-5}.

A previous search at ATLAS $\sqrt{s} = 7$ TeV was carried out. No signal was found and upper limits were placed on the production cross section[2, 4]. Other hadron collider experiments such as CMS and D0 also set upper limits on prompt lepton-jets production [7, 8, 39, 40]. Related searches for non-prompt lepton-jets productions [3, 5] have been performed at ATLAS and limits were placed for smaller values of kinetic mixing parameter, $\epsilon \leq 10^{-5}$.

4.1.1 Dark photon branching fraction

The branching fraction of dark photons to e^+e^-, $\mu^+\mu^-$ and $\pi^+\pi^-$ is determined by the mass of the dark photon, m_{γ_d}. Figure 4.2 shows the branching fraction of dark photon to e^+e^-, $\mu^+\mu^-$, and hadrons. Table 4.1 show a detailed list of dark photon branching fractions to various channels. If $2m_e < m_{\gamma_d} < 2m_\mu$, the branching fraction of dark photons that goes to e^+e^- is 100%, if $2m_\mu < m_{\gamma_d} < 2m_\pi$, the dark photons decay into a pair of muon-antimuon and electron-positron, about equally. For $m_{\gamma_d} > 2m_\pi$, the branching fraction of dark photon is inferred from the ratio between the production cross section of hadrons and the production cross-section of muons in e^+e^- collision data [31, 65].

No excess of anti-protons is observed over protons in the astrophysical data [13, 30]. Therefore, the region with a dark photon mass below 2 GeV is the most interesting.

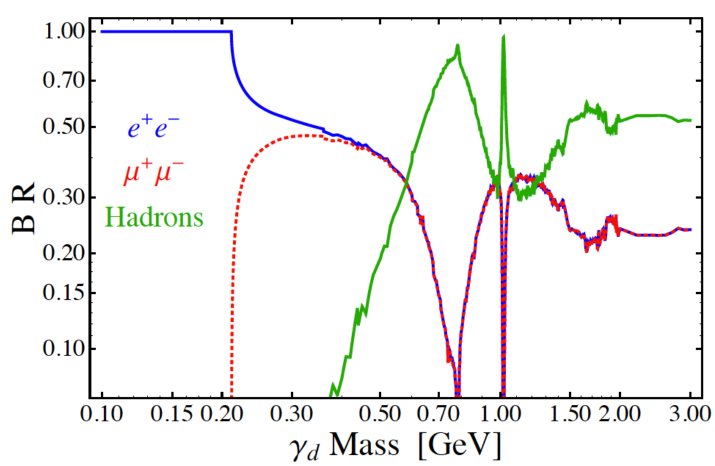

Figure 4.2. Branching fraction of dark bosons to leptons and hadrons.

Table 4.1. The decay modes of γ_d and corresponding branching fractions [31, 65] as implemented in the SUSY signal MC generations.

$m_{\gamma_d} = 0.1, 0.2$ GeV		$m_{\gamma_d} = 0.3$ GeV	
decay modes	BF	decay modes	BF
$\gamma_d \to e^+e^-$	1.0	$\gamma_d \to e^+e^-$	0.53
		$\gamma_d \to \mu^+\mu^-$	0.47
$m_{\gamma_d} = 0.4$ GeV			
$\gamma_d \to e^+e^-$	0.45		
$\gamma_d \to \mu^+\mu^-$	0.45		
$\gamma_d \to \pi^+\pi^-$	0.10		
$m_{\gamma_d} = 0.5$ GeV		$m_{\gamma_d} = 0.7$ GeV	
$\gamma_d \to e^+e^-$	0.4	$\gamma_d \to e^+e^-$	0.15
$\gamma_d \to \mu^+\mu^-$	0.4	$\gamma_d \to \mu^+\mu^-$	0.15
$\gamma_d \to \pi^+\pi^-$	0.2	$\gamma_d \to \pi^+\pi^-$	0.70
$m_{\gamma_d} = 0.9$ GeV		$m_{\gamma_d} = 1.2$ GeV	
$\gamma_d \to e^+e^-$	0.27	$\gamma_d \to e^+e^-$	0.34
$\gamma_d \to \mu^+\mu^-$	0.27	$\gamma_d \to \mu^+\mu^-$	0.33
$\gamma_d \to \pi^+\pi^-$	0.42	$\gamma_d \to \pi^+\pi^-$	0.064
$\gamma_d \to \pi^+\pi^-\pi^o\pi^o$	0.036	$\gamma_d \to \omega\pi^o$	0.079
$\gamma_d \to \pi^+\pi^-\pi^+\pi^-$	0.007	$\gamma_d \to K^+K^-$	0.045
		$\gamma_d \to K^o\bar{K}^o$	0.005
		$\gamma_d \to \pi^+\pi^-\pi^o\pi^o$	0.075
		$\gamma_d \to \pi^+\pi^-\pi^+\pi^-$	0.041
		$\gamma_d \to \pi^+\pi^-\pi^o$	0.024
$m_{\gamma_d} = 1.5$ GeV		$m_{\gamma_d} = 2.0$ GeV	
$\gamma_d \to e^+e^-$	0.24	$\gamma_d \to e^+e^-$	0.24
$\gamma_d \to \mu^+\mu^-$	0.24	$\gamma_d \to \mu^+\mu^-$	0.24
$\gamma_d \to \pi^+\pi^-\pi^o\pi^o$	0.23	$\gamma_d \to \pi^+\pi^-\pi^o\pi^o$	0.150
$\gamma_d \to \pi^+\pi^-\pi^+\pi^-$	0.23	$\gamma_d \to \pi^+\pi^-\pi^+\pi^-$	0.093
$\gamma_d \to \pi^+\pi^-\pi^o$	0.035	$\gamma_d \to \pi^+\pi^-\pi^o$	0.010
$\gamma_d \to \pi^+\pi^-\pi^+\pi^-\pi^o$	0.009	$\gamma_d \to \pi^+\pi^-\pi^+\pi^-\pi^o$	0.031
$\gamma_d \to K^+K^-\pi^o$	0.0101	$\gamma_d \to K^+K^-\pi^+\pi^-$	0.062
$\gamma_d \to \pi^+\pi^-\pi^+\pi^-\pi^+\pi^-$	0.0027	$\gamma_d \to K^+K^-\pi^o$	0.026
$\gamma_d \to \pi^+\pi^-\pi^+\pi^-\pi^o\pi^o$	0.0016	$\gamma_d \to K^+K^-\pi^+\pi^-\pi^o$	0.007
$\gamma_d \to \pi^+\pi^-$	0.0014	$\gamma_d \to \pi^+\pi^-\pi^+\pi^-\pi^+\pi^-$	0.023
		$\gamma_d \to \pi^+\pi^-\pi^+\pi^-\pi^o\pi^o$	0.093
		$\gamma_d \to p\bar{p}$	0.014
		$\gamma_d \to \pi^+\pi^-$	0.007

4.1.2 The SUSY portal

Supersymmetry mediated models, as described in [37], consider the dark sector particles produced from SUSY final states. In the proton-proton collisions in the LHC, squark ($\tilde{q}_i$) pairs are produced. Squarks are super symmetric partners to quarks of the Standard Model. The squarks ($\tilde{q}_i$) decay to the lightest super symmetry particle, the neutralino ($\tilde{\chi}_1^0$), where the neutralino decays into the dark sector producing a dark photon (γ_d) or a dark scalar (s_d). Squarks are set to decay with 100% branching fraction (BR) into a quark and a neutralino ($\tilde{\chi}_1^0$) as shown in Figure 4.3. The neutralinos decay into the hidden sector particles with either of the two decay modes, $\tilde{\chi}_1^0 \to \gamma_d \tilde{\chi}_d$ or $\tilde{\chi}_1^0 \to s_d \tilde{\chi}_d$, where $s_d \to \gamma_d \gamma_d$. Dark photon showering in the dark sector is set to zero.

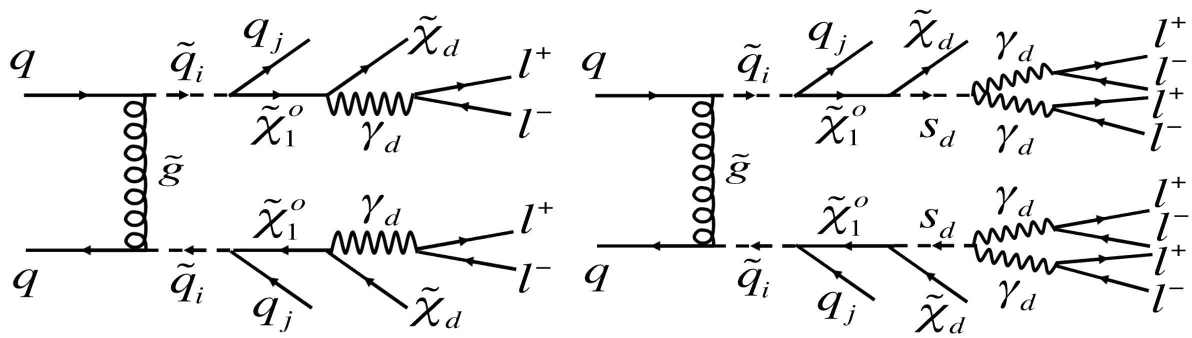

Figure 4.3. Feynman diagram illustrating the dark photon production in the final state. (left) 2 γ_d final state, (right) 4 γ_d final state.

The generated mass of a squark is 700 GeV with a production cross section of 64 fb (femtobarn). A 700 GeV squark mass is not excluded by previous searches [2]. The $\tilde{\chi}_1^0$ mass is set to 8 GeV. A set of γ_d masses is chosen ranging from 0.1 GeV to 2 GeV. The dark scalar s_d mass is set to 2 GeV for samples with γ_d masses below 0.9 GeV, 4 GeV for samples with γ_d mass in the range of 0.9 to 1.5 GeV, and 4.5 GeV for sample with γ_d mass of 2 GeV. This ensures the mass spectrum is not squeezed and all particles in the decay chain remain on-shell. Masses of γ_d above 2 GeV are not favored due to the nonobservance of anti-protons excess over protons in the cosmic-ray data [13, 30].

4.1.3 The Higgs portal

The Higgs portal refers to possible decays of the SM Higgs boson to a pair of dark fermions f_{d2} [11, 48] as shown in the Figure 4.4. The dark fermion f_{d2} then decays to a dark photon

(γ_d) and a lighter dark fermion (f_{d1}) otherwise known as the Hidden Lightest Stable Particle (HLSP) (Figure 4.4a). In another possibility, the dark fermion f_{d2} decays to a lighter dark fermion f_{d1} (or HLSP) and a dark scalar s_{d1}, where the dark scalar then decays to a pair of dark photons (Figure 4.4b). Dark photon showering in the dark sector is set to zero.

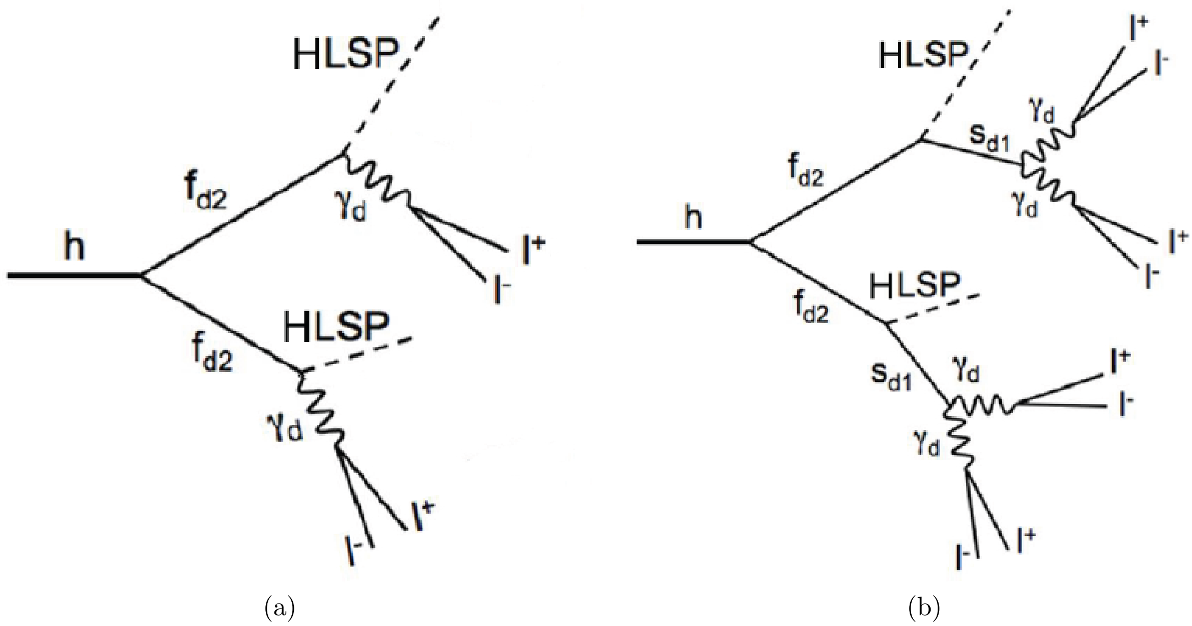

Figure 4.4. The Higgs boson decays to a pair of dark fermions f_{d2}, which then subsequently decays to a Hidden Lightest Stable Particle (HLSP) and a dark photon (left) or to a HLSP and a dark scalar s_{d1} (right), which in turn decays to pair of dark photons γ_d

The Higgs boson ($m_H = 125\ GeV$) is produced through the gluon-gluon fusion production mechanism with an estimated production cross-section of $\sigma_{SM} = 19.2$ pb in the pp collisions at $\sqrt{s} = 8$ TeV. The mass of f_{d2} is 5 GeV, the mass of f_{d1} and s_{d1} are both set to 2 GeV, and the γ_d, mass is 0.4 GeV. The masses of the dark fermions f_{d1} and f_{d2} are light relative to the Higgs mass. The branching fraction of the dark photon at 0.4 GeV is expected to be 45% e^+e^-, 45% $\mu^+\mu^-$ and 10% $\pi^+\pi^-$. There are four branching fractions of the Higgs boson to the dark particle are considered: 5%, 10%, 20%, and 40%

4.2 LeptonJets

A dark photon that kinetically mixes with a SM photon decays to a pair of collimated, energetic lepton-antilepton or quark-antiquark pair, depending on the mass of the dark photon, γ_d. An energetic, collimated lepton pair is called a lepton-jet (LJ). Lepton-jets are therefore signature for discovering dark photons in the ATLAS detector.

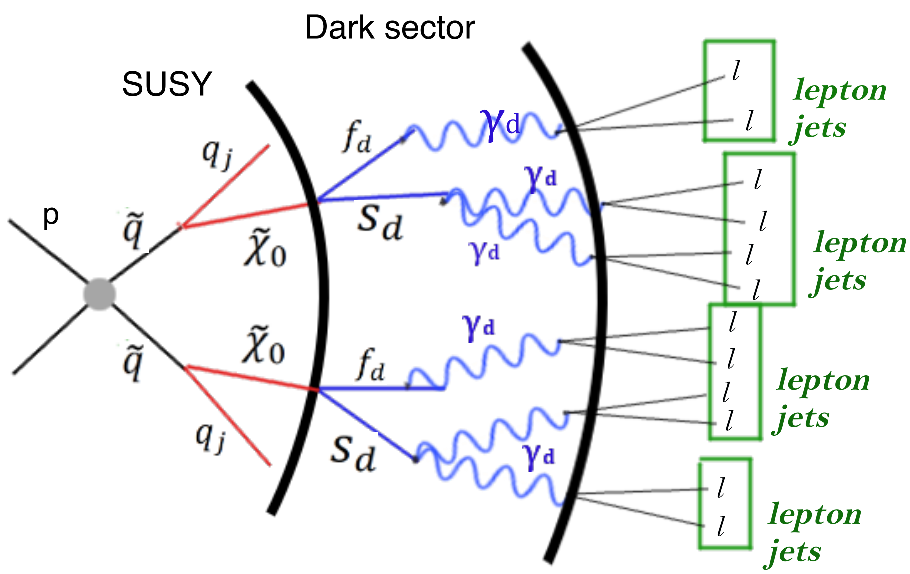

Figure 4.5. Feynman diagram showing lepton jets production through super symmetry (SUSY) mechanism.

Figure 4.5 shows a toy Feynman diagram of lepton-jets production through SUSY portal. Starting with a proton-proton (pp) collision, squark pairs are produced that then decay to the lightest SUSY particle, the neutralino ($\tilde{\chi}_0$). Neutralino decay into the dark sector, producing dark scalars (s_d). Dark scalars decay to two dark photon γ_d, which lead to lepton-jets.

CHAPTER 5

DATA AND MONTE CARLO SAMPLES

The data collected with the ATLAS detector in 2012 is grouped into three streams: The Egamma stream, the Muon stream, and the JetTauEtMiss stream. In this document, from this point onward the Egamma stream and the Muon stream will be referred to as search streams, and the JetTauEtMiss stream will be referred to as the background stream. In this work, the entire 20.3 fb^{-1} of good quality data (blue shade in Figure 3.2) collected with the ATLAS detector during the data-taking period of 2012 is used. The good quality data ensures that all the relevant detector systems operated properly and that events are not erroneously retained due to instrumental noise.

The Monte Carlo software package in ATLAS provides tools to generate signal and background events, and simulate the events in the ATLAS detector. Monte Carlo events are vital in understanding the behavior of the signal events, backgrounds, and detector performance.

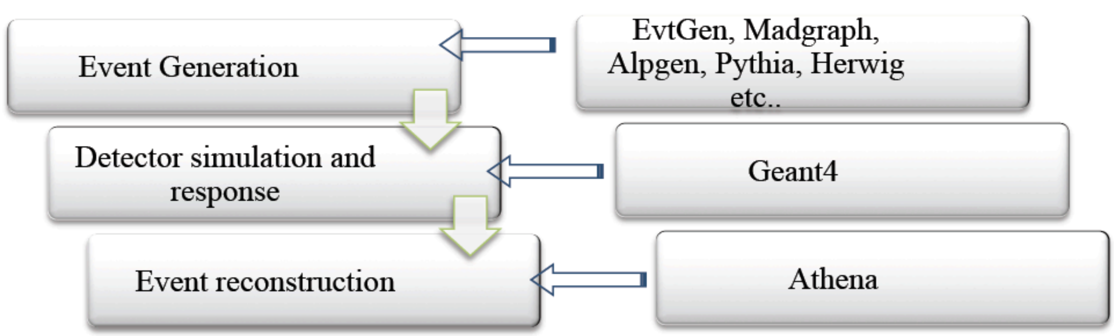

Figure 5.1. Monte Carlo production steps (left) and the tools used in each stage (right).

Figure 5.1 shows the steps involved in the Monte Carlo simulation, and the tools that are used at each stage. The ATLAS Monte Carlo full-chain process is Event generation — Simulation — Digitizing — Reconstruction. In this work, Madgraph[16] is used to generate dark photons and decay them into Standard Model leptons. Pythia, Powheg, Sherpa, Alpgen, and Jimmy are used to generate Standard Model background events. In the ATLAS collaboration, Monte Carlo production is a centralized process that conforms to the collaboration standards. Only ATLAS approved Monte Carlo samples can be used for analysis and publications. In ATLAS, Monte Carlo generated particles are known as "truth particles" or just "truth".

To study the signal characteristics, three sets of signal MC samples are used. They are, lepton-jet gun samples (Appendix A), SUSY mediated samples (Section 4.1.2), and Higgs mediated samples (Section 4.1.3).

Background Monte Carlo samples listed in Table 5.1 are used to study the contribution and characteristics of the background processes. Such Monte Carlo samples are helpful in optimizing the analysis to reject background events, while retaining signal events (lepton-jet events).

Table 5.1. List of background Monte Carlo samples used to study the characteristics and contribution of background processes. This table shows various Standard Model processes, the MC generator used to produce those processes.

Samples	MC generator	Int. luminosity (fb^{-1})
QCD (0 GeV $\leq p_T \leq$ 20 GeV)	Pythia8	0.82 $\times 10^{-7}$
QCD (20 GeV $< p_T \leq$ 80 GeV)	Pythia8	0.82 $\times 10^{-7}$
QCD (80 GeV $< p_T \leq$ 200 GeV)	Pythia8	0.23 $\times 10^{-3}$
QCD (200 GeV $< p_T \leq$ 500 GeV)	Pythia8	0.011
QCD (500 GeV $< p_T \leq$ 1000 GeV)	Pythia8	0.93
QCD (1000 GeV $< p_T \leq$ 1500 GeV)	Pythia8	75.4
QCD (1500 GeV $< p_T \leq$ 2000 GeV)	Pythia8	7194.6
QCD ($p_T >$ 2000 GeV)	Pythia8	73628.2
γ+jets (20 GeV $\leq p_T \leq$ 40 GeV)	Pythia8	1.2 $\times 10^{-3}$
γ+jets (40 GeV $< p_T \leq$ 80 GeV)	Pythia8	1.0 $\times 10^{-2}$
γ+jets (80 GeV $< p_T \leq$ 150 GeV)	Pythia8	0.1
γ+jets (150 GeV $< p_T \leq$ 300 GeV)	Pythia8	3.2
γ+jets ($p_T >$ 300 GeV)	Pythia8	166.4
$W(\to e\nu)$ + jets	Powheg + Pythia8	3.3, 3.6
$W(\to \mu\nu)$ + jets	Powheg + Pythia8	3.3, 3.6
$W(\to \tau\nu)$ + jets	Powheg + Pythia8	0.58, 0.63
$Z/\gamma^*(\to ee)$ + jets	Powheg + Pythia8	9.0
$Z/\gamma^*(\to \mu\mu)$ + jets	Powheg + Pythia8	9.0
$Z/\gamma^*(\to \tau\tau)$ + jets	Powheg + Pythia8	4.5
$t\bar{t} \to$ lepton + jets	MCAtNLO + Jimmy	72.0
$t\bar{t} \to$ all jets	MCAtNLO + Jimmy	5.8
$t\bar{t} \to$ di-leptons	MCAtNLO + Jimmy	48.1
$\gamma\gamma$	Sherpa	20.6
$W + W \to l\nu l\nu$	Sherpa	491.0
$W + Z/\gamma^* \to l\nu l\nu$	Sherpa	276.9
$Z/\gamma^* + Z/\gamma^* \to llll$	Sherpa	434.8
$Z/\gamma^* + Z/\gamma^* \to ll\nu\nu$	Sherpa	1814.5
10 - 60 GeV DY ($\gamma^* \to ee$ + jets)	Alpgen+Jimmy	0.29 – 14.5
10-60 GeV DY ($\gamma^* \to \mu\mu$ + jets)	Alpgen+Jimmy	0.29 – 14.5
10-60 GeV DY ($\gamma^* \to \tau\tau$ + jets)	Alpgen+Jimmy	0.29 – 14.5
2-8 GeV DY ($\gamma^* \to ee$ + jets)	Sherpa	59.7
2-8 GeV DY ($\gamma^* \to \mu\mu$ + jets)	Sherpa	59.7

CHAPTER 6

SELECTION OF EVENTS WITH LEPTON-JETS

Events are required to have a primary collision vertex containing at least three ID tracks in order to remove cosmic rays. All events should satisfy the trigger requirements. There must be at least two lepton-jets present in an event.

6.1 Track, electron cluster, and muon selection

A lepton-jet is reconstructed using ID tracks, electromagnetic clusters, and muons. Tracks are selected with transverse[1] momentum p_{T} >5 GeV, pseudo-rapidity $|\eta\ |$[2] $<$ 2.5, and the closest approach of a track to the primary vertex in the transverse plane $|d0| < 1mm$. Additional requirements are placed on the number hits along the track in the Pixel and the SCT detectors. Electromagnetic clusters are selected with transverse energy $E_T >$ 10 GeV, $|\eta| < 2.47$. Muon candidates are selected with p_{T} >5 GeV, $|\eta| < 2.5$. Muon candidates must be reconstructed both in the ID and the muon spectrometer, and additional requirements are made on the number of hits on the muon candidate track in the ID.

6.2 Lepton-jet definition

A lepton-jet (LJ) is a collection of boosted leptons within an angular separation, $\Delta R = \sqrt{\Delta\eta^2 + \Delta\phi^2}$[3]. Figure 6.1 shows the dependence of the average angular separation between truth (Monte Carlo generated particle) leptons in an event as a function of the transverse momentum of the γ_d (s_d) for various mass γ_d values. The average ΔR between the leptons decreases with increasing p_T of the dark photon.

---

[1] Transverse to the direction of the beam.

[2] $\eta = -log(tan\frac{\theta}{2})$, θ is the angle measured anticlockwise from the beam axis when viewed from outside the ring.

[3] ΔR in ATLAS is equivalent to solid angle in geometry. $\Delta R = \sqrt{\Delta\eta^2 + \Delta\phi^2}$, where $\eta = -log(tan\frac{\theta}{2}))$ and ϕ is the azimuthal angle.

Figure 6.2 shows the distribution of the maximum ΔR among the truth-matched, reconstructed ID tracks in the LJ gun sample for various for various γ_d and s_d mass values. The truth particle is matched to the ID tracks by requiring the closest ΔR between a truth lepton and the ID tracks to be smaller than 0.05. The search criteria $\Delta R \leq 0.5$ is sufficient for clustering the nearby ID tracks belonging to an O(1) GeV γ_d or $s_d \to \gamma_d\gamma_d$ (see Section 6.3).

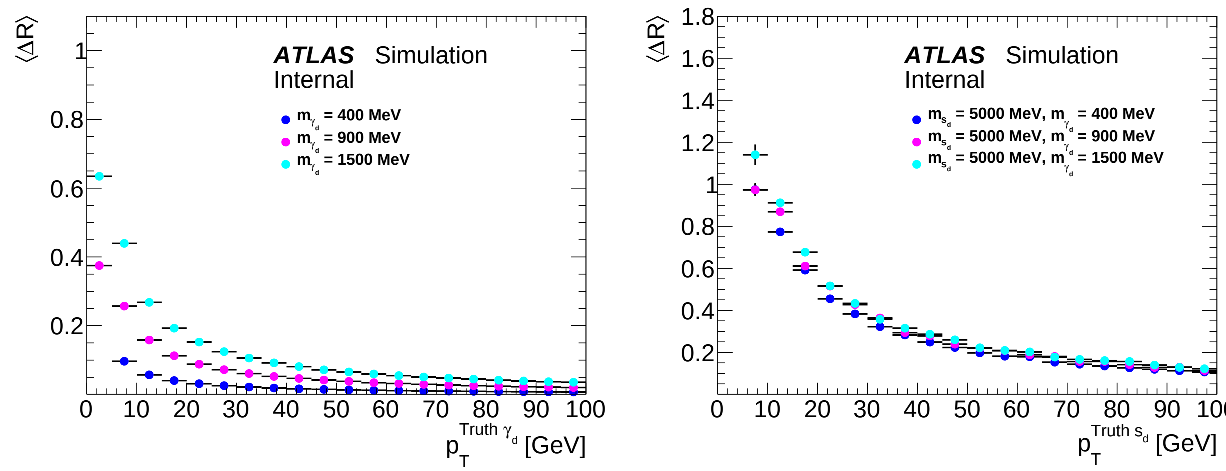

Figure 6.1. Angular separation between two truth muons with respect to the p_T of γ_d (left), with respect to the p_T of scalar dark particle s_d with a mass of 5 GeV (right).

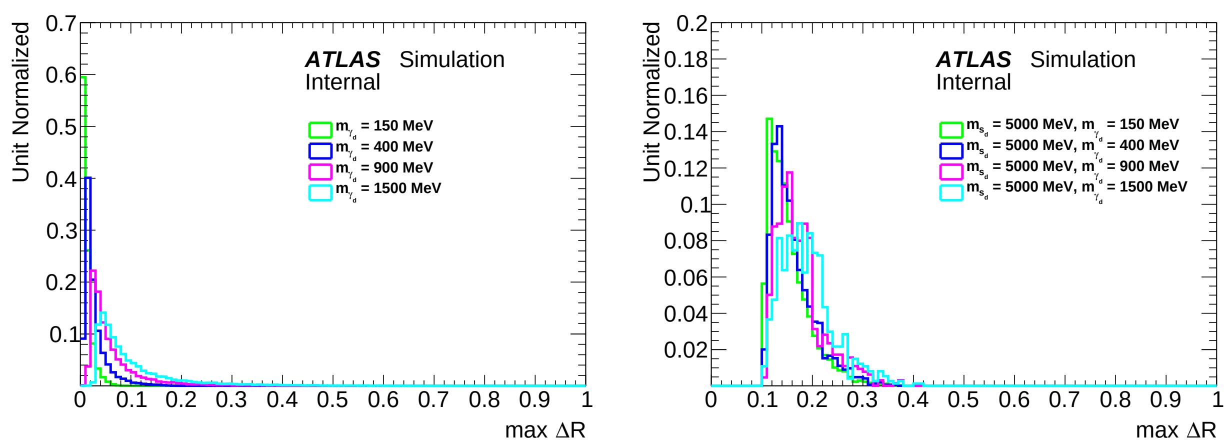

Figure 6.2. Maximum ΔR between truth-matched reconstructed ID tracks in the LJ gun samples for various masses of γ_d. Single γ_d samples are shown on the left. Dark scalar $s_d \to \gamma_d\gamma_d$, $m_{s_d} = 5$ GeV, samples are shown at the right. γ_d have been decayed to e^+e^-.

6.3 Lepton-jet pre-selection

Candidate lepton-jets are formed from ID tracks. Lepton-jet building is based in an iterative algorithm within $\Delta R = 0.5$ cone. All selected ID tracks from an event's primary vertex are p_{T} ordered. Starting from the first seed track in the list, the next track within $\Delta R = 0.5$ with respect to the momentum of the seed track is found. The 4-momenta of the two tracks are summed to give the 4-momentum of the lepton-jet candidate. Subsequent track within 0.5 cone around the lepton-jet candidate are added iteratively, recomputing the momentum sum at each step. The procedure is repeated until the track list is exhausted. Tracks that have been added to the lepton-jet candidates are removed from consideration for subsequent LJ candidates. Additional lepton-jet candidates are built from the remaining tracks in the list following the same procedure. Each lepton-jet candidate must contain at least two tracks. These lepton-jet candidates are categorized as follows:

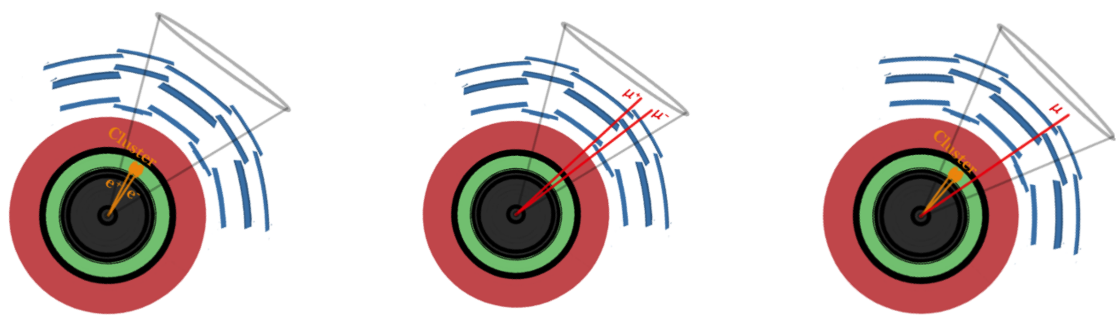

(a) (b) (c)

Figure 6.3. Cartoon showing (a) eLJ, (b) muLJ, and (c) emuLJ in a cut-away wedge section of the ATLAS detector.

- **Electron-jet (eLJ):** If at least one electromagnetic (EM) cluster with cluster transverse energy, $E_T \geq 10$ GeV is found within a $\Delta R \leq 0.5$ cone around the lepton-jet candidate direction and there are no muon candidates within the cone. The lepton-jet candidate is called an electron-jet (eLJ). Due to the limited spatial resolution of the EM calorimeter, the two electrons from an O(1) GeV γ_d offen merge to form a single cluster.

- **Muon-jet (muLJ):** If at least two muon candidates satisfying all selection criteria described in Section 6.1 are found within within a $\Delta R \leq 0.5$ cone around the lepton-jet candidate's direction, then the lepton-jet candidate is called a muon-jet (muLJ). There must no electromagnetic cluster within the cone.

- **Mixed-jet (emuLJ):** If at least one EM cluster and one muon candidates satisfying all cuts as described in Section 6.1 are found within the cone around the lepton-jet candidate direction, then the lepton-jet candidate is called a mixed-jet (emuLJ). Mixed-jets would derive from $s_d \to \gamma_d\ \gamma_d$, where one γ_d decays to e^+e^- and other to $\mu^+\mu^-$.

A lepton-jet candidate failing the eLJ, muLJ, and emuLJ criteria is rejected from further consideration. Note that there are six possible combinations of two lepton-jets selection per event:

Electron channel	eLJ - eLJ
Muon channel	muLJ - muLJ
Mixed channels	eLJ - muLJ eLJ - emuLJ muLJ - emuLJ emuLJ - emuLJ

The characteristics and the efficiency of the reconstructed lepton-jets are studied using LJ gun samples (Section A). The eLJ reconstruction efficiency (Figures 6.4-6.5) is defined as the fraction of events having at least one truth $\gamma_d \to e^+e^-$ that contains a reconstructed eLJ matched to the direction of the dark particle (γ_d or s_d). Reconstructed eLJs and the truth γ_d's (s_d's) are matched by requiring the angle, ΔR, between the momentum direction of the eLJ and the truth γ_d (s_d) to be less than 0.5. In case of efficiency evaluation as a function of the p_{T} of the s_d, both γ_d are required to decay into electron pairs.
The muLJ reconstruction efficiency (Figures 6.6-6.7) is defined as the fraction of events having at least one truth $\gamma_d \to \mu^+\mu^-$ that contains a reconstructed muLJ matched to the direction of the dark particle (γ_d or s_d). Reconstructed muLJ and the truth γ_d (s_d) are matched by requiring the angle, ΔR, between the momentum direction of muLJ and the truth γ_d (s_d) to be less than 0.5. In case of efficiency evaluation as a function of p_{T} of the s_d, both γ_d are required to decay into muon pairs.

The emuLJ reconstruction efficiency (Figure 6.8) is defined as the fraction of events with two truth γ_d from a dark scalar (s_d) that contains a reconstructed emuLJ matched to the

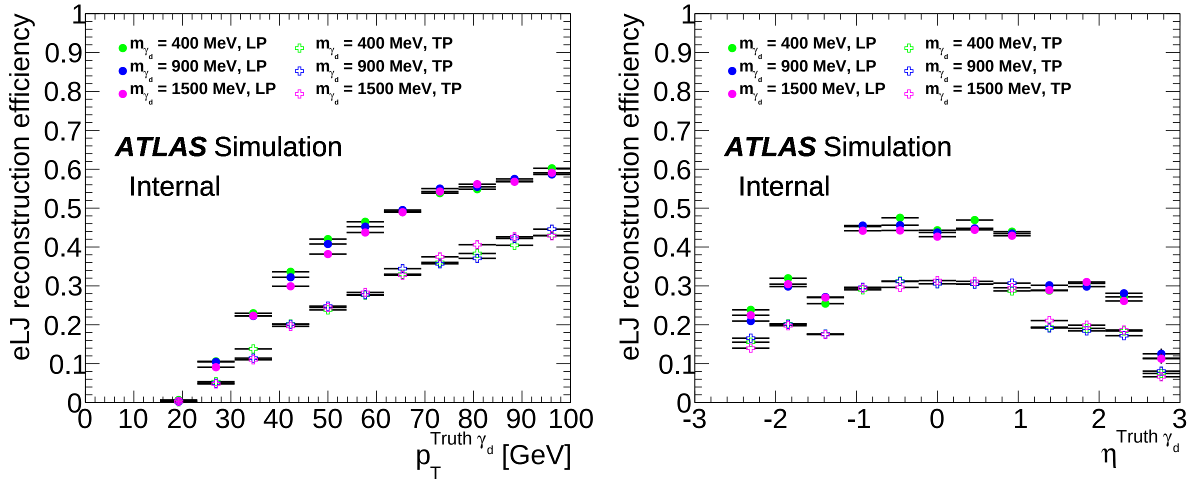

Figure 6.4. Efficiency of eLJ reconstruction as a function of p_T (left) and η (right) of longitudinally (LP) or transversely (TP) polarized γ_d for a $\gamma_d \rightarrow e^+e^-$.

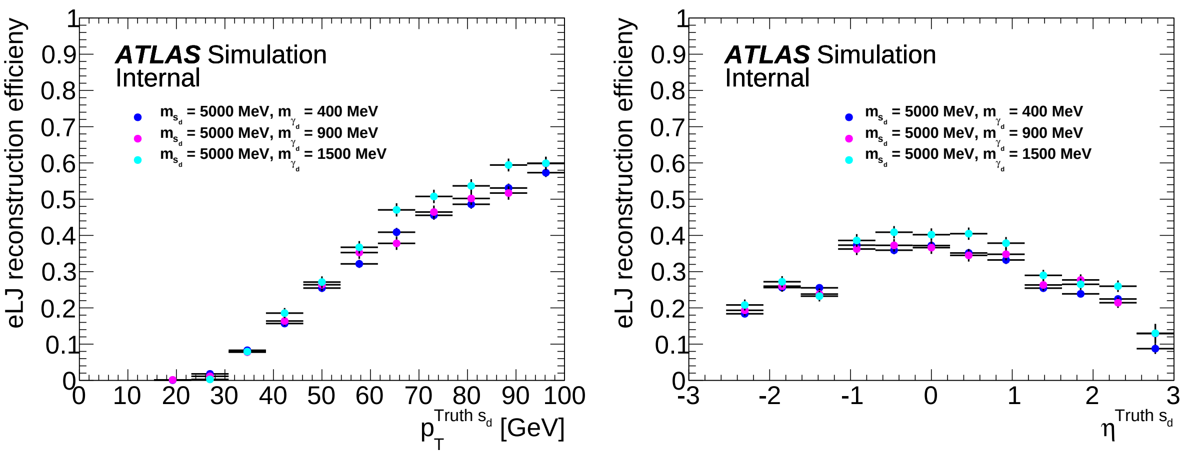

Figure 6.5. Efficiency of eLJ reconstruction as a function of p_T (left) and η (right) of s_d for $s_d \rightarrow \gamma_d\gamma_d$, with s_d mass of 5 GeV, for events where both γ_d decay to e^+e^-.

direction of s_d, where one $\gamma_d \rightarrow e^+e^-$ and another $\gamma_d \rightarrow \mu^+\mu^-$. Reconstructed emuLJ and the truth (s_d) are matched by requiring the ΔR between the momentum direction of emuLJ and the truth s_d to be less than 0.5.

The efficiency turn on in Figures 6.4 - 6.8 for γ_d is due to the requirement of at least two tracks with $p_T \geq 10$ GeV associated to at least one cluster with $E_T \geq 10$ GeV. In Figures 6.4 and 6.6 longitudinally polarized (LP) dark photons have a higher efficiency than the transversely polarized (TP) dark photon due to the lower probability of imbalanced momenta of decayed

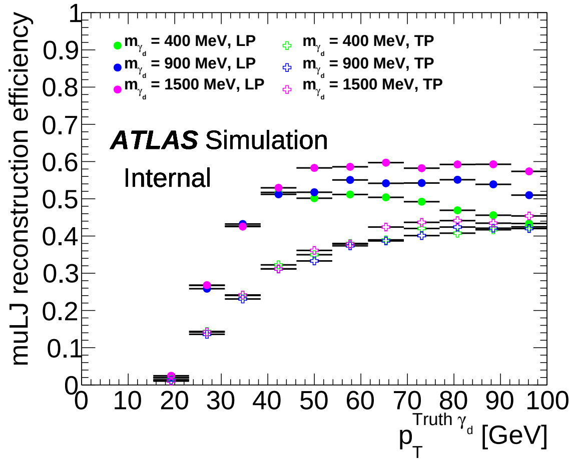

Figure 6.6. Efficiency of muLJ reconstruction as a function of p_T (left) and η (right) for longitudinally (LP) or transversely (TP) polarized γ_d with $\gamma_d \to \mu^+\mu^-$.

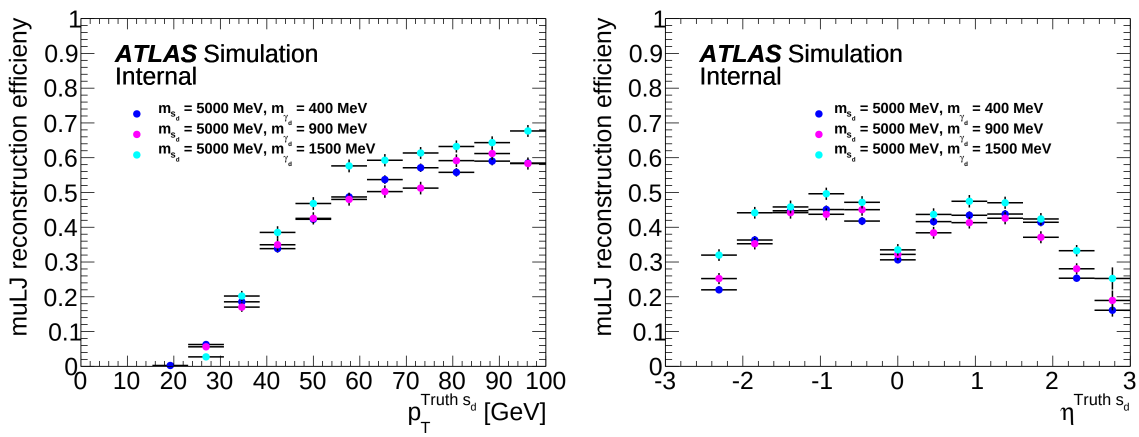

Figure 6.7. Efficiency of muLJ reconstruction as a function of p_T (left) and η (right) of s_d for $s_d \to \gamma_d\gamma_d$, with s_d mass of 5 GeV, for events where both γ_d decay to $\mu^+\mu^-$.

electrons in the case of LP dark photons. The sub-leading lepton from TP dark photons tend to fail the p_{T} >10 GeV cut.

At higher p_{T} the reconstruction efficiency of muLJ from single γ_d sample drops due to the collimation of muons. As the p_{T} of the γ_d increases, muons tend to be collimated and become too close to be reconstructed as two individual muons in the muon spectrometer. This effect is more pronounced for the LP γ_d, because of higher probability of its decay products to carry equivalent p_T and with higher collimations. Further, the drop in efficiency is steeper for a low mass γ_d, as the opening angle directly depends on the γ_d mass.

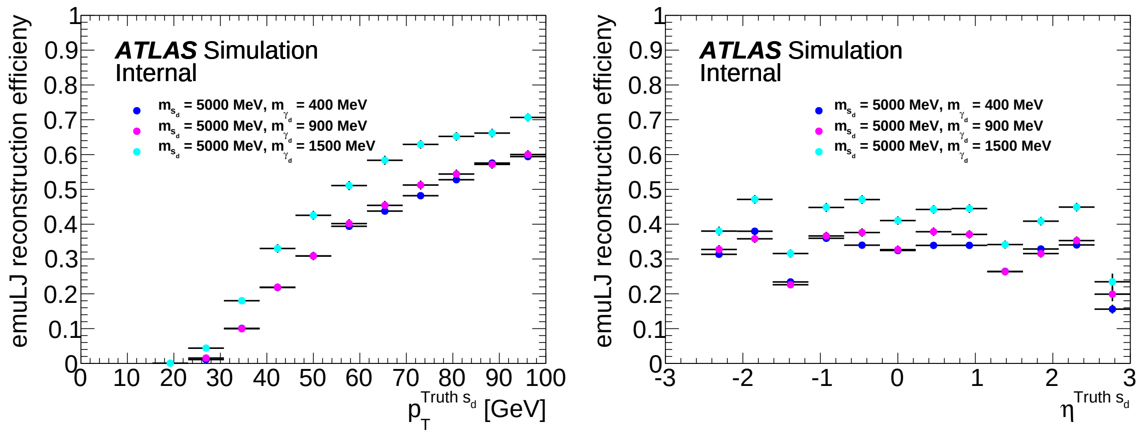

Figure 6.8. Efficiency of emuLJ reconstruction as a function of dark scalar p_T (left) and η (right) for $s_d \to \gamma_d \gamma_d$, with s_d mass of 5 GeV, where one γ_d decays to e^+e^- and the other to $\mu^+\mu^-$. The efficiency for high mass γ_d is higher due to relatively wider opening angle of its final state leptons, making it relatively efficient to find at least two reconstructed tracks.

6.4 Lepton jet discriminating variables

The set of variables listed in Section 6.4.1 play a key role in characterizing the lepton-jets and discriminating the signal against the background. By effectively choosing cut values for these variables, signal events are preferentially selected and background events are preferentially rejected. The choice of these variables depends on the type of a lepton-jet. Sections 6.4.1 to 6.4.3 list all the variables that are considered for eLJs, muLJs, and emuLJs. Figures 6.9 - 6.11 show the shape of the eLJ, muLJ, and emuLJ variables for signal MC samples and for the dominant backgrounds.

6.4.1 eLJ variables

- **Track isolation:** Track isolation is defined as the ratio between the p_T sum of the ID tracks within $\Delta R \leq 0.5$, "electron-tracks" excluded, and the p_T of the eLJ. Each ID track used for the isolation calculation passes the requirements described in Section 6.1.

- **Fraction of high threshold hits in TRT, f_{HT}:** Electrons deposit higher energy in the TRT than the pions due to transition radiation. The ratio of the number of high threshold TRT hits to the total number of TRT hits, f_{HT} is used.

- **Energy of strip with maximal energy deposit, E_{s1}^{max}:** The first sampling of the EM calorimeter has a finer granularity in η. This granularity can distinguish between electron and π^0 showers. An electron tends to deposit its energy in a single strip, while the $\pi^0 \to \gamma\gamma$ decays tend to share energy between two strips, providing a discriminant for π^0 rejection.

- **Fraction of energy deposited in third sampling of EM calorimeter, f_{s3}:** Electron deposit most of their energy in the second sampling of the EM calorimeter, leaving only small amount leaking into the third sampling. Therefore, the fraction of energy found in the third sampling should be small to identify the electrons. A hadron on the other hand deposit relatively higher fraction of their total EM calorimeter energy in the third sampling.

- **Electromagnetic energy fraction, f_{EM}:** This is the fraction of cluster's total transverse energy found in the EM calorimeter. An eLJ is expected to have larger EM fraction compared to a QCD jet.

Figure 6.9 shows the distribution of eLJ discriminating variables for signal MC from the LJgun and for background MC samples of QCD jets, photons (which are converted and produces two tracks), and electrons from $Z \to e^+e^-$ events that is associated to an additional ID track from nearby QCD jet.

6.4.2 muLJ variables

- **Track isolation:** Track isolation is defined as the ratio between the p_{T} sum of the ID tracks within $\Delta R \leq 0.5$, "muon-tracks" excluded, and the p_{T} of the muLJ. Each ID track used for the isolation calculation must pass the requirements described in Section 6.1.

- **Calorimeter isolation:** The ratio of the total transverse energy in the EM calorimeter within a 0.2 cone around the leading muon of muLJ to the p_{T} of that muon. Muons are minimum ionizing particles, whereas electrons and hadrons produce showers.

6.4.3 emuLJ variables

- **Track isolation:** The ratio between the p_T sum of the ID tracks within $\Delta R \leq 0.5$, electron-tracks and muon-tracks excluded, and the emuLJ p_T. Each ID track used for the isolation calculation must pass the precision hit requirements as described in Section 6.1.

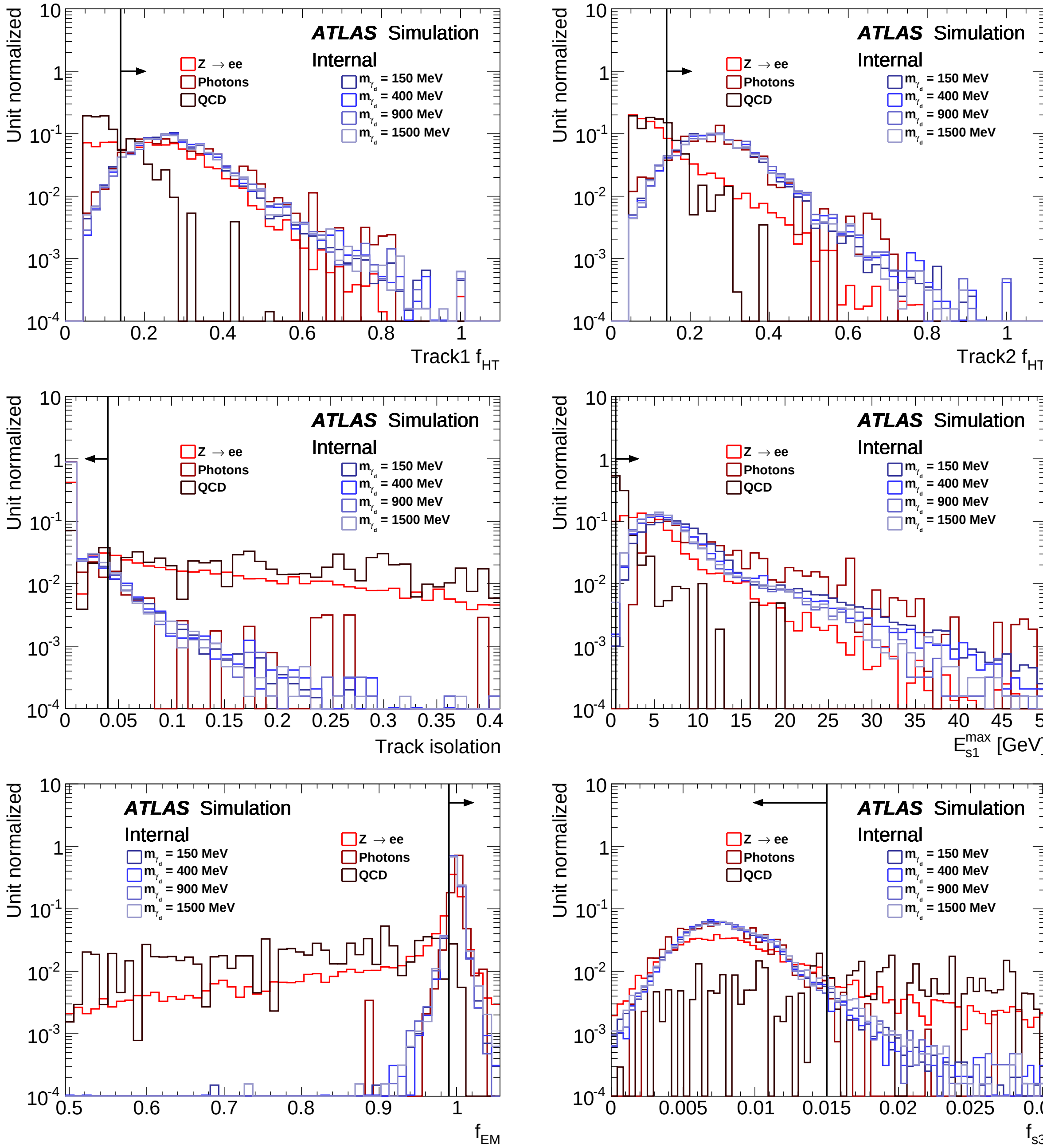

Figure 6.9. The shape of eLJ discriminating variables for events containing exactly one eLJ. The black vertical line shows the cut value on the variable and the arrow points towards the selected region. Top left and right: Fraction of high threshold hits in TRT deposited by leading and subleading tracks, respectively, middle left: Track isolation, middle right: Energy of strip with maximal energy deposit, E_{s1}^{max}, bottom left: Electromagnetic energy fraction, f_{EM}, bottom right: Fraction of energy deposited in third sampling of EM calorimeter, f_{s3}.

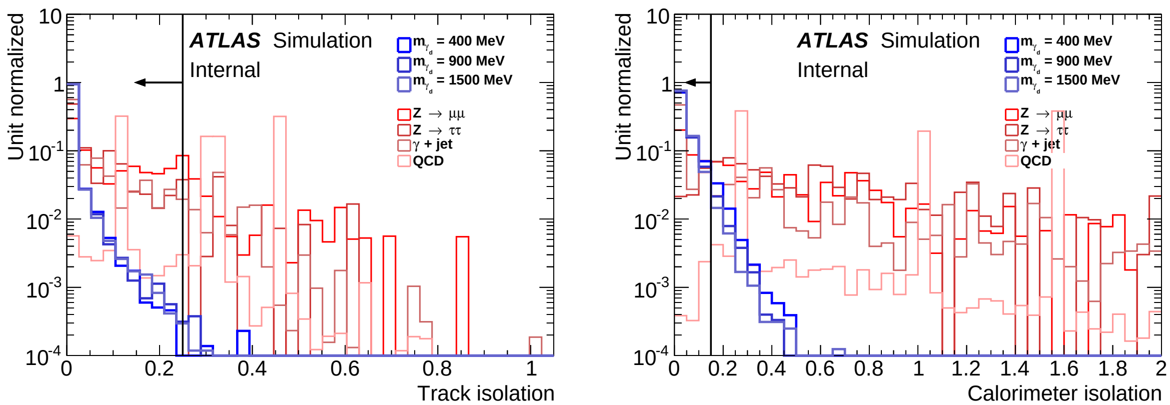

(a) (b)

Figure 6.10. The shape of the muLJ discriminating variables in the MC samples of the LJ gun and the dominant backgrounds - QCD, γ + jet, Z $\rightarrow \mu\mu$ and Z $\rightarrow \tau\tau$. The black vertical line shows the cut value on the variable and the arrow points the selection region. (a) Track isolation, (b) Calorimeter isolation.

- **Energy of strip with maximal energy deposit, E_{s1}^{max}:** Same as described in Section 6.4.1.
- **Fraction of energy deposited in third sampling of EM calorimeter, f_{s3}:** Same as described in Section 6.4.1.
- **Hadronic leakage, E_T^{had}:** The transverse energy of the electron deposited in the first sampling of hadronic calorimeter. The emuLJ is expected only to have a small hadronic contribution due to the presence of muon within the cone. Hadronic backgrounds typically show energy deposit from hadronic showering.

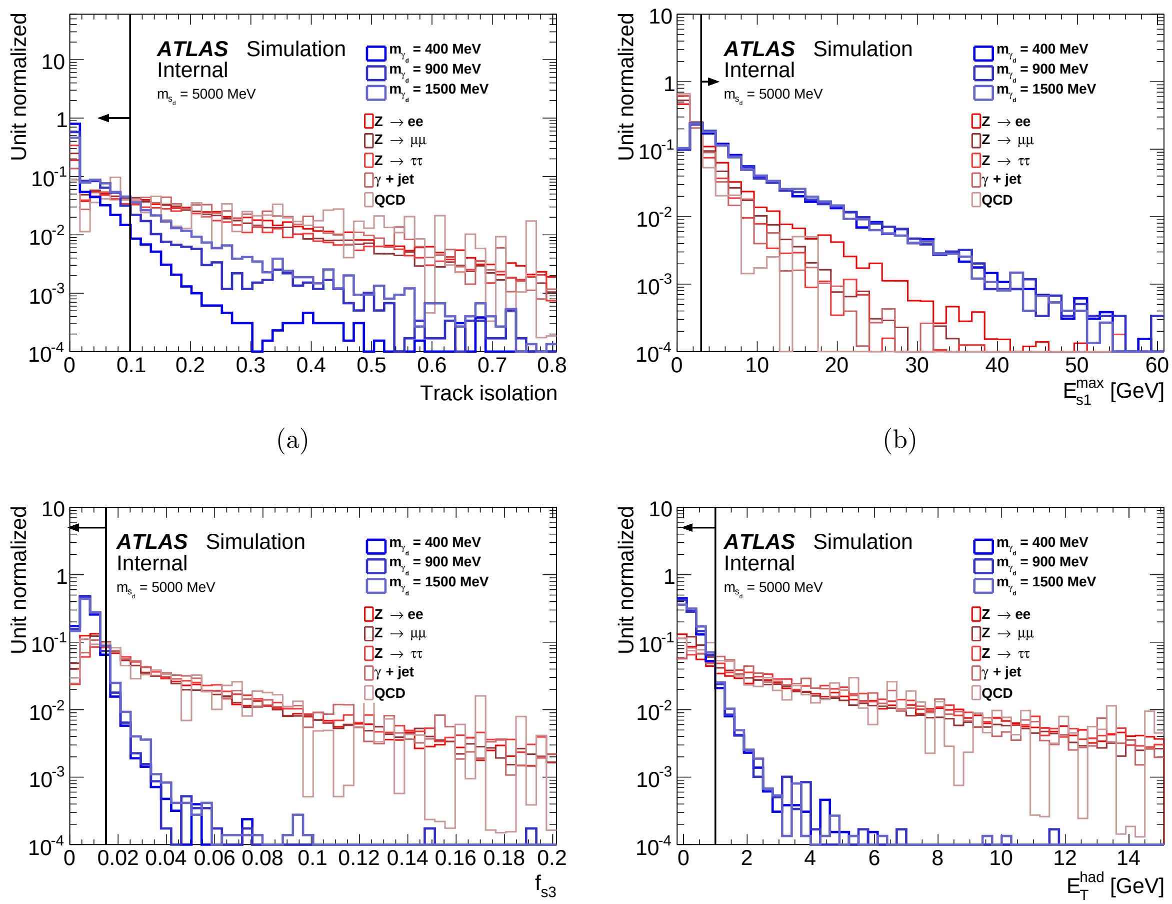

(a) (b) (c) (d)

Figure 6.11. The shape of the emuLJ discriminating variables in the MC samples of the LJ gun and dominant backgrounds - QCD, γ + jet, Z $\to ee$, Z $\to \mu\mu$, and Z $\to \tau\tau$. The black vertical line shows the cut value on the variable and the arrow points the selection region. (a) Track isolation, (b) Energy of strip with maximal energy deposit, (c) Fraction of energy deposited in third sampling of EM calorimeter, f_{s3}, (d) E_T^{had}.

6.5 Lepton-jet variables optimization

Cuts on the lepton-jet discriminating variables are used to reject background events and select signal. The cuts are optimized to maximize the signal to background ratio as expressed in Eqn. 6.1.

$$\text{Significance} = \frac{\epsilon_s \times \sigma \times \mathcal{L}}{1 + \sqrt{n_B}} \tag{6.1}$$

where ϵ_s represents the signal efficiency. The signal efficiency is the product of the LJ reconstruction efficiency (Section 6.3), the discriminating variable cut efficiency and the trigger efficiency (Section 6.6). The signal cross-section σ is arbitrarily set to 1 fb. A part of the background stream data is used to evaluate hadronic backgrounds. The integrated luminosity $\mathcal{L}$ is set to 5 fb^{-1}, corresponding to the size of the background data sample used. The symbol n_B denotes the number of background events passing the cuts. The signal efficiency is obtained from an LJgun sample.

All the variables of a given LJ are simultaneously optimized to arrive at the global significance maximum (Eqn. 6.1). In the multi-dimensional variable space, the cuts that produce the maximum significance is located. This point is specified by n coordinates in an n-dimensional variable space, where each coordinate corresponds to the cut value for that variable. For example, in eLJ the cut values for the five discriminating variables are simultaneously optimized by building a 5-dimensional variable space and locating the point with maximum significance. The optimized cuts for all LJ variables are given in Table 6.1. The total efficiency of selected cuts on the discriminating variables is shown in Figure 6.13.

For visualization of the significance in the variable space, the cut values of all the variables are set to their optimal values except for the two variables shown in the Figure 6.12. Figure 6.12a shows the significance of the eLJ discriminating variables cut in the track isolation and f_{EM} space, while cut on the E_{s1}^{max}, f_{s3}, and f_{HT} are fixed to the values listed in Table 6.1. Figure 6.12b shows the significance of the muLJ discriminating variables cut in the track isolation and calorimeter isolation space. Figure 6.12c shows the significance of the emuLJ discriminating variables cut in the track isolation and f_{s3} space, while cut on the E_{s1}^{max} and E_T^{had} are fixed as listed in Table 6.1. Figure 6.12 demonstrates the choice of cut values for a given LJ.

The eLJ cut efficiency is defined as the fraction of reconstructed eLJs matched to a truth γ_d decaying to e^+e^- that would further pass the cuts on the discriminating variables. The muLJ cut efficiency is defined as the fraction of reconstructed muLJ matched to a truth γ_d decaying to $\mu^+\mu^-$ that would further pass the cuts on muLJ variables. The emuLJ cut efficiency is defined as the fraction of emuLJs matched to two truth γ_d, where one $\gamma_d \rightarrow e^+e^-$ and another $\gamma_d \rightarrow \mu^+\mu^-$, that would further pass the emuLJ discriminating variables cuts. The efficiencies for the cuts on the individual variables are shown in Appendix C.1.

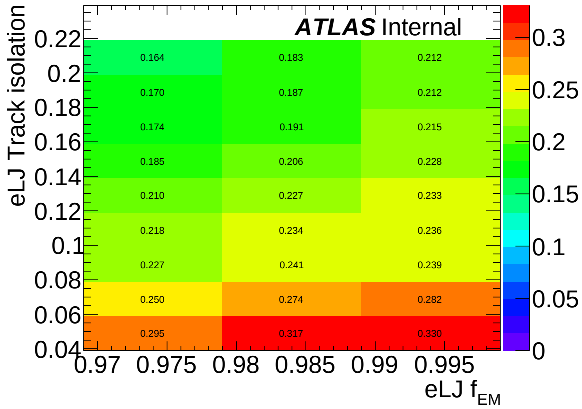

(a)

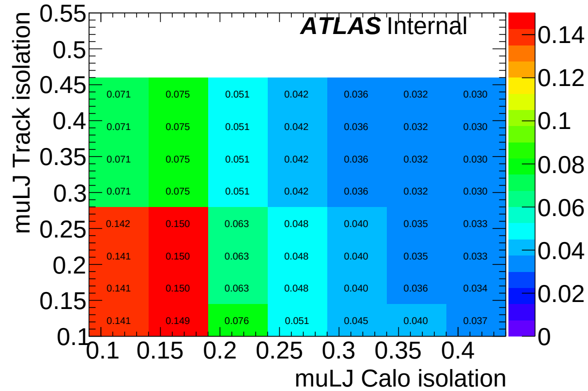

(b)

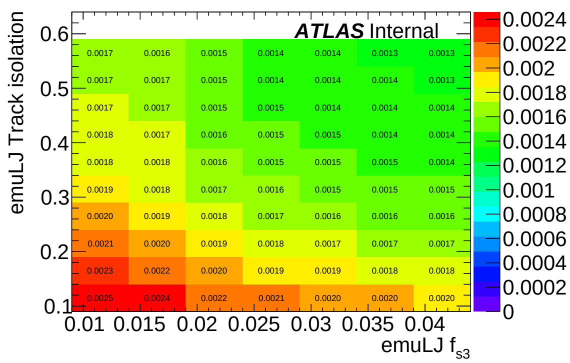

(c)

Figure 6.12. Two-dimensional 'significance' plots for various cut values for a given LJ. For visualization, cuts on the discriminating variables not shown are fixed to the optimal value. (Top left) eLJ variables. (Top right) muLJ variables. (Bottom) emuLJ variables.

Table 6.1. The final set of cut values for discriminating eLJs, muLJs and emuLJs.

eLJ	muLJ	emuLJ
$E_{s1}^{max} >$ 0.5 GeV track isolation $<$ 0.04 $f_{HT} >$ 0.14 $f_{EM} >$ 0.99 $f_{s3} <$ 0.015	track isolation $<$ 0.25 calo isolation $<$ 0.15	$E_{s1}^{max} >$ 3 GeV track isolation $<$ 0.1 $E_T^{had} <$ 1 GeV $f_{s3} <$ 0.015

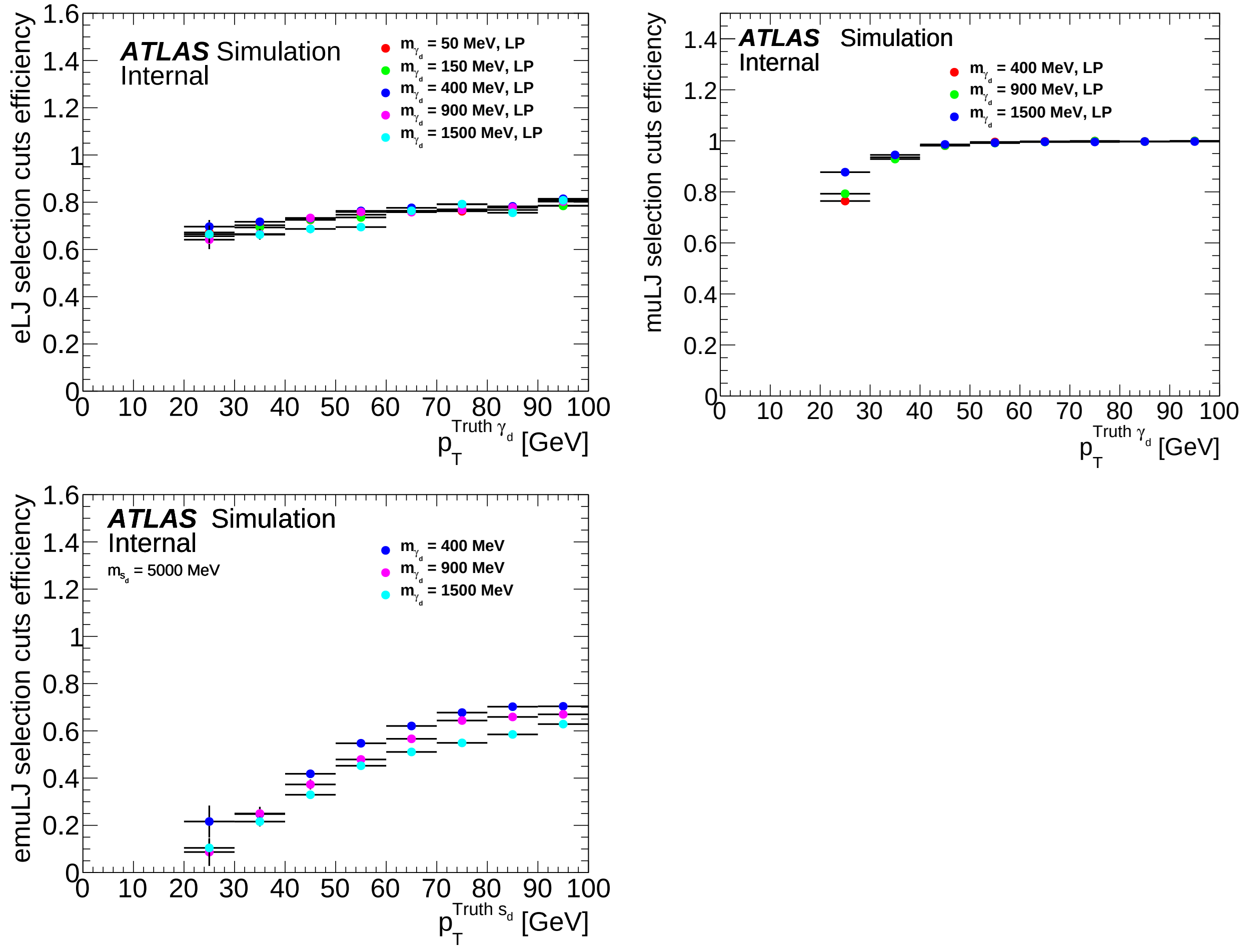

Figure 6.13. Efficiency of the selected cuts on the discriminating variables of eLJ (top left), muLJ (top right) and emuLJ (bottom) as a function of dark particle p_{T}. Figures C.2, C.1, and C.3 show further detail on the impact of each cut on efficiencies. The emuLJ suffers from larger loss in cut efficiency at low p_T due to tighter cut on E_{s1}^{max}.

The branching fraction for lepton jet final state

Given that represents The probability for a γ_d to decay into an electron pair, a muon pair, or to a hadron pair is given by p_e, p_μ or p_h, such that $p_e+p_\mu+p_h = 1$. The values for p_e, p_μ or p_h are determined from e^+e^- data [31, 65] as shown in Figure 4.2. The branching fractions for two lepton-jets final states can be computed based on the following formulas for samples with $2\gamma_d$ or with $2(s_d \to \gamma_d\gamma_d)$ from the SUSY mediated samples. The branching fraction for eLJ–eLJ, muLJ–muLJ, eLJ–muLJ, eLJ–emuLJ, muLJ–emuLJ and emuLJ–emuLJ production in $2\gamma_d$ and $2(s_d \to \gamma_d\gamma_d)$ final states are given by the following equations expressed in terms of p_e and p_μ:

$$\begin{aligned}
B^{\text{eLJ–eLJ}}_{2\gamma_d} &= p_e^2 \\
B^{\text{muLJ–muLJ}}_{2\gamma_d} &= p_\mu^2 \\
B^{\text{eLJ–muLJ}}_{2\gamma_d} &= 2p_e p_\mu \\
B^{\text{eLJ–emuLJ}}_{2\gamma_d} &= 0 \\
B^{\text{muLJ–emuLJ}}_{2\gamma_d} &= 0 \\
B^{\text{emuLJ–emuLJ}}_{2\gamma_d} &= 0
\end{aligned}$$

$$\begin{aligned}
B^{\text{eLJ–eLJ}}_{2(s_d\to\gamma_d\gamma_d)} &= Prob.(s_d \to \gamma_d + \gamma_d \to ee + ee) \times Prob.(s_d \to \gamma_d + \gamma_d \to ee + ee) \\
&+ Prob.(s_d \to \gamma_d + \gamma_d \to ee + ee) \times Prob.(s_d \to \gamma_d + \gamma_d \to ee + hh) \\
&+ Prob.(s_d \to \gamma_d + \gamma_d \to ee + hh) \times Prob.(s_d \to \gamma_d + \gamma_d \to ee + hh) \\
&= p_e^4 + 4p_e^3 p_h + 4p_e^2 p_h^2 \\
&= p_e^4 + 4p_e^3(p_\mu - 1) + 4p_e^2(p_\mu - 1)^2
\end{aligned}$$

$$\begin{aligned}
B^{\text{muLJ–muLJ}}_{2(s_d\to\gamma_d\gamma_d)} &= Prob.(s_d \to \gamma_d + \gamma_d \to \mu\mu + \mu\mu) \times Prob.(s_d \to \gamma_d + \gamma_d \to \mu\mu + \mu\mu) \\
&+ Prob.(s_d \to \gamma_d + \gamma_d \to \mu\mu + \mu\mu) \times Prob.(s_d \to \gamma_d + \gamma_d \to \mu\mu + hh) \\
&+ Prob.(s_d \to \gamma_d + \gamma_d \to \mu\mu + hh) \times Prob.(s_d \to \gamma_d + \gamma_d \to \mu\mu + hh) \\
&= p_\mu^4 + 4p_\mu^3 p_h + 4p_\mu^2 p_h^2 \\
&= p_\mu^4 + 4p_\mu^3(p_e - 1) + 4p_\mu^2(p_e - 1)^2
\end{aligned}$$

$$
\begin{aligned}
B_{2(s_d\to\gamma_d\gamma_d)}^{\text{eLJ–muLJ}} &= Prob.(s_d \to \gamma_d + \gamma_d \to ee + ee) \times Prob.(s_d \to \gamma_d + \gamma_d \to \mu\mu + \mu\mu) \\
&+ Prob.(s_d \to \gamma_d + \gamma_d \to ee + hh) \times Prob.(s_d \to \gamma_d + \gamma_d \to \mu\mu + \mu\mu) \\
&+ Prob.(s_d \to \gamma_d + \gamma_d \to ee + ee) \times Prob.(s_d \to \gamma_d + \gamma_d \to \mu\mu + hh) \\
&+ Prob.(s_d \to \gamma_d + \gamma_d \to ee + hh) \times Prob.(s_d \to \gamma_d + \gamma_d \to \mu\mu + hh) \\
&= 2p_e^2p_\mu^2 + 4p_ep_\mu^2p_h + 4p_e^2p_\mu p_h + 8p_ep_\mu p_h^2 \\
&= 10p_e^2p_\mu^2 + 4p_e^3p_\mu + 4p_ep_\mu^3 - 12p_e^2p_\mu - 12p_ep_\mu^2 + 8p_ep_\mu
\end{aligned}
$$

$$
\begin{aligned}
B_{2(s_d\to\gamma_d\gamma_d)}^{\text{eLJ–emuLJ}} &= Prob.(s_d \to \gamma_d + \gamma_d \to ee + ee) \times Prob.(s_d \to \gamma_d + \gamma_d \to ee + \mu\mu) \\
&+ Prob.(s_d \to \gamma_d + \gamma_d \to ee + hh) \times Prob.(s_d \to \gamma_d + \gamma_d \to ee + \mu\mu) \\
&= 4p_e^3p_\mu + 8p_e^2p_\mu p_h \\
&= 8p_e^2p_\mu - 4p_e^3p_\mu - 8p_e^2p_\mu^2
\end{aligned}
$$

$$
\begin{aligned}
B_{2(s_d\to\gamma_d\gamma_d)}^{\text{muLJ–emuLJ}} &= Prob.(s_d \to \gamma_d + \gamma_d \to ee + \mu\mu) \times Prob.(s_d \to \gamma_d + \gamma_d \to \mu\mu + \mu\mu) \\
&+ Prob.(s_d \to \gamma_d + \gamma_d \to \mu\mu + hh) \times Prob.(s_d \to \gamma_d + \gamma_d \to ee + \mu\mu) \\
&= 4p_ep_\mu^3 + 8p_ep_\mu^2p_h \\
&= 8p_ep_\mu^2 - 4p_ep_\mu^3 - 8p_e^2p_\mu^2
\end{aligned}
$$

$$
\begin{aligned}
B_{2(s_d\to\gamma_d\gamma_d)}^{\text{emuLJ–emuLJ}} &= Prob.(s_d \to \gamma_d + \gamma_d \to ee + \mu\mu) \times Prob.(s_d \to \gamma_d + \gamma_d \to ee + \mu\mu) \\
&= 4p_e^2p_\mu^2
\end{aligned}
$$

Table 6.2 shows the computed values of the branching fractions for various two lepton-jet pair channels in $2\gamma_d$ and $2(s_d \to \gamma_d\gamma_d)$ final states based on the above formulas and using the decay probability values given in Table 4.1.

Table 6.2. The branching fractions for two lepton-jets final state in various channels. The eLJ–eLJ is the only sensitive channel for γ_d masses below $\mu\mu$ threshold.

γ_d mass	eLJ–eLJ		muLJ–muLJ		eLJ–muLJ		eLJ–emuLJ	muLJ–emuLJ	emuLJ–emuLJ
	2 γ_d	4 γ_d	2 γ_d	4 γ_d	2 γ_d	4 γ_d	4 γ_d	4 γ_d	4 γ_d
$m_{\gamma_d} = 0.1$ GeV	1.0	1.0	0	0	0	0	0	0	0
$m_{\gamma_d} = 0.2$ GeV	1.0	1.0	0	0	0	0	0	0	0
$m_{\gamma_d} = 0.3$ GeV	0.28	0.08	0.22	0.05	0.50	0.12	0.28	0.22	0.25
$m_{\gamma_d} = 0.4$ GeV	0.20	0.09	0.20	0.09	0.41	0.17	0.24	0.24	0.16
$m_{\gamma_d} = 0.5$ GeV	0.16	0.10	0.16	0.10	0.32	0.20	0.21	0.20	0.10
$m_{\gamma_d} = 0.7$ GeV	0.02	0.05	0.02	0.05	0.05	0.11	0.02	0.02	0.002
$m_{\gamma_d} = 0.9$ GeV	0.07	0.10	0.07	0.10	0.15	0.21	0.09	0.09	0.02
$m_{\gamma_d} = 1.2$ GeV	0.12	0.12	0.11	0.11	0.22	0.22	0.15	0.15	0.05
$m_{\gamma_d} = 1.5$ GeV	0.06	0.09	0.06	0.09	0.12	0.19	0.07	0.07	0.01
$m_{\gamma_d} = 2.0$ GeV	0.06	0.09	0.06	0.09	0.12	0.19	0.07	0.07	0.01

6.6 Trigger selection and efficiency

The ATLAS experiment's data acquisition software uses triggers to reduce the event rate by selecting only useful events as discussed in Section 3.3. The ATLAS trigger criteria used for this study are listed in Table 6.3.

In order to select signal-like events, a logical OR of two or more triggers is used to maximize acceptance for various signal topologies. The trigger efficiency is extracted using the SUSY signal Monte Carlo samples for events where two lepton-jets are reconstructed and pass the cuts on the associated discriminating variables. The trigger efficiency is determined by counting the fraction of generated events passing the selection criteria of a lepton-jet that would also pass the trigger criteria.

In the eLJ-eLJ channel, the OR of EF_e60_medium1 and EF_g35_loose_g25_loose triggers is used. Figure 6.14 shows the trigger efficiency as a function of eLJ's cluster E_T for various γ_d masses in a set of samples produced with two γ_d (left) and two s_d (right), where $s_d \to \gamma_d\, \gamma_d$.

Table 6.3. List of triggers used to select eLJ, muLJ, and emuLJ events.

Lepton-jet	ATLAS trigger name	Description
eLJ	EF_e60_medium1	Single electron trigger that select events with one EM cluster $E_T > 60$ GeV.
	EF_g35_loose_g25_loose	Di-photon trigger that select events with two EM clusters, with cluster $E_T > 35$ and $E_T > 25$ GeV.
muLJ	EF_mu36_tight	Single muon trigger that select events with muon p_{T} >36GeV.
	EF_2mu13	Di-muon trigger that select events with two muons p_{T} >13GeV.
emuLJ	OR of eLJ and muLJ triggers	EF_e60_medium1, EF_mu36_tight, and EF_2mu13.

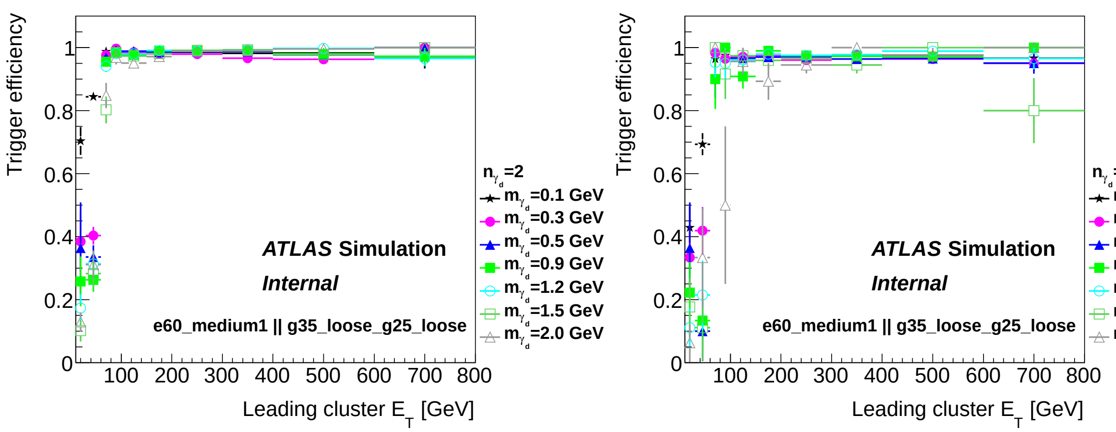

Figure 6.14. Trigger efficiency for events having at least two selected eLJs that pass the OR of EF_e60_medium1 and EF_g35_loose_g25_loose trigger requirements. The left (right) plot shows the efficiencies as a function of leading eLJ's cluster E_T for the signal MC samples with two (four) γ_d in the final state. The EF_g35_loose_g25_loose trigger is important for capturing the softer electrons of the 4 γ_d signal.

In the muLJ-muLJ channel, the OR of EF_mu36_tight, EF_2mu13, and EF_3mu6_MSonly triggers is used. The muon channel trigger efficiency as a function of the leading muon p_T of muLJ is shown in Figure 6.15.

In the mixed channel, (eLJ-muLJ, eLJ-emuLJ, muLJ-emuLJ, emuLJ-emuLJ) the OR of triggers EF_e60_medium1, EF_mu36_tight and EF_2mu13 triggers is used . The mixed channel trigger efficiency as a function of the leading muon p_T of muLJ is shown in Figure 6.16.

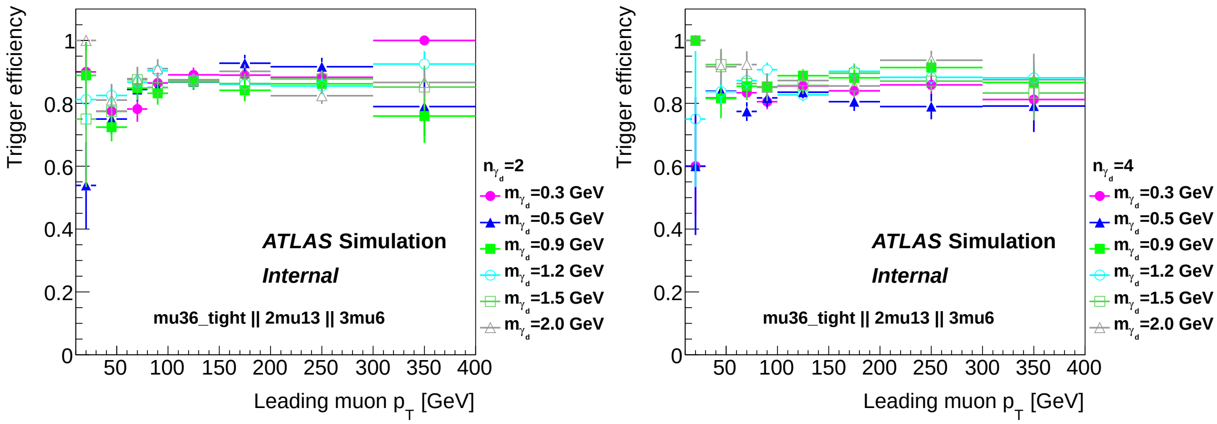

Figure 6.15. Trigger efficiency for events having at least two selected muLJs that pass the OR of EF_mu36_tight, EF_2mu13, and EF_3mu6_MSonly trigger requirements. The left (right) plot shows the efficiencies as a function of leading muon p_T in muLJ for the signal MC samples with two (four) γ_d in the final state.

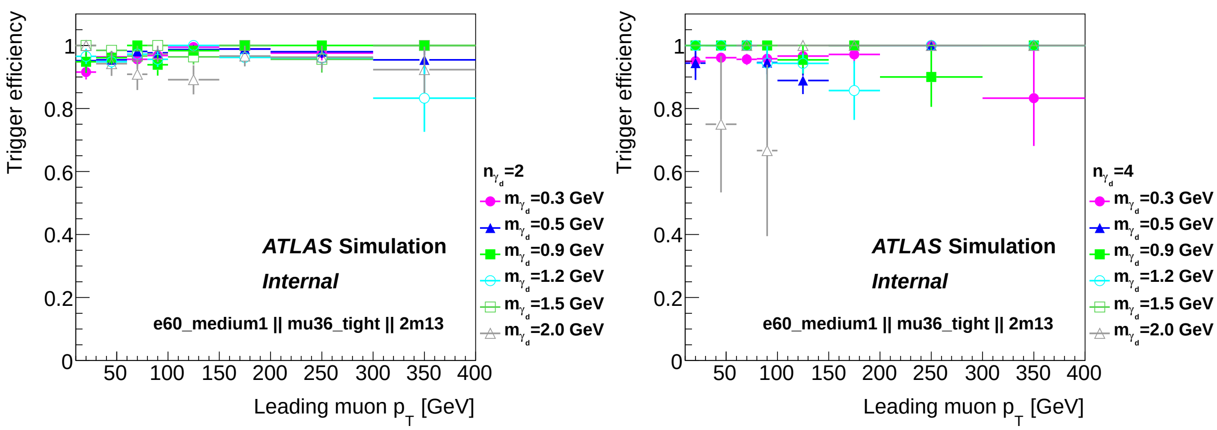

Figure 6.16. Trigger efficiency for eLJ-muLJ channel, after the offline selection of at least one eLJ and at least one muLJ per event, passing the OR of EF_e60_medium1, EF_mu36_tight, and EF_2mu13, trigger requirements. The left (right) plot shows the efficiencies as a function of leading muon p_T in muLJ for the signal MC samples with two (four) γ_d in the final state.

6.7 Signal expectation from MC

The expected number of signal events after all analysis selection is expressed as

$$N = \mathcal{L} \times \sigma \times BR \times \epsilon_{trig} \times \epsilon_{reco} \times \epsilon_{cut} \tag{6.2}$$

where $\mathcal{L}$ is the integrated luminosity, σ is the cross-section, BR is the branching fraction of the dark photon to a LJ pair, ϵ_{trig} is the trigger efficiency, ϵ_{reco} is the LJ reconstruction efficiency, and ϵ_{cuts} is the cut efficiency of the discriminating variables. Table 6.4 and 6.5

show the signal MC event yield in 20.3 fb^{-1} equivalent MC samples for all six lepton-jet pair combinations for all the dark photon masses considered.

Table 6.4. Signal MC event yield after all analysis selection cuts. Each column corresponds eLJ-eLJ, muLJ-muLJ, and eLJ-muLJ lepton jet pair channel. All numbers correspond to 20.3 fb^{-1} luminosity.

	eLJ-eLJ	muLJ-muLJ	eLJ-muLJ
SUSY MC ($n_{\gamma_d} = 2$)			
$m_{\gamma_d} = 0.1$ GeV	37.5 ± 1.0	-	-
$m_{\gamma_d} = 0.3$ GeV	15.8 ± 0.6	14.4 ± 0.6	18.4 ± 0.7
$m_{\gamma_d} = 0.5$ GeV	10.0 ± 0.5	14.3 ± 0.6	15.3 ± 0.6
$m_{\gamma_d} = 0.7$ GeV	1.3 ± 0.2	2.4 ± 0.3	2.1 ± 0.2
$m_{\gamma_d} = 0.9$ GeV	3.6 ± 0.2	9.0 ± 0.4	5.6 ± 0.3
$m_{\gamma_d} = 1.2$ GeV	6.3 ± 0.3	17.0 ± 0.5	10.2 ± 0.4
$m_{\gamma_d} = 1.5$ GeV	3.1 ± 0.2	9.3 ± 0.4	5.9 ± 0.3
$m_{\gamma_d} = 2.0$ GeV	3.6 ± 0.2	12.2 ± 0.5	6.8 ± 0.3
SUSY MC ($n_{\gamma_d} = 4$)			
$m_{\gamma_d} = 0.1$ GeV	109.1 ± 1.6	-	-
$m_{\gamma_d} = 0.3$ GeV	12.0 ± 0.5	23.2 ± 0.8	21.5 ± 0.8
$m_{\gamma_d} = 0.5$ GeV	4.5 ± 0.3	17.3 ± 0.7	11.2 ± 0.5
$m_{\gamma_d} = 0.7$ GeV	0.08 ± 0.04	1.4 ± 0.2	0.6 ± 0.1
$m_{\gamma_d} = 0.9$ GeV	0.7 ± 0.1	6.4 ± 0.3	3.0 ± 0.2
$m_{\gamma_d} = 1.2$ GeV	2.1 ± 0.2	11.2 ± 0.4	6.8 ± 0.3
$m_{\gamma_d} = 1.5$ GeV	0.8 ± 0.1	4.8 ± 0.3	3.1 ± 0.2
$m_{\gamma_d} = 2.0$ GeV	0.6 ± 0.1	4.0 ± 0.3	2.3 ± 0.2
Higgs MC ($n_{\gamma_d} = 2$)			
$m_{\gamma_d} = 0.4$ GeV	183.5 ± 12.2	1036.8 ± 31.0	322.0 ± 16.9
Higgs MC ($n_{\gamma_d} = 4$)			
$m_{\gamma_d} = 0.4$ GeV	9.1 ± 6.5	235.4 ± 33.9	40.8 ± 14.0

Table 6.5. Signal MC event yield after all analysis selection cuts. Each column corresponds eLJ-emuLJ, muLJ-emuLJ, and emuLJ-emuLJ lepton jet pair channel. All numbers correspond to 20.3 fb^{-1} luminosity.

	eLJ-emuLJ	muLJ-emuLJ	emuLJ-emuLJ
SUSY MC ($n_{\gamma_d} = 4$)			
$m_{\gamma_d} = 0.3$ GeV	18.2 ± 0.7	30.0 ± 0.9	19.6 ± 0.7
$m_{\gamma_d} = 0.5$ GeV	8.7 ± 0.5	17.3 ± 0.7	8.8 ± 0.5
$m_{\gamma_d} = 0.7$ GeV	0.09 ± 0.04	0.3 ± 0.1	0.2 ± 0.1
$m_{\gamma_d} = 0.9$ GeV	2.0 ± 0.2	4.1 ± 0.3	2.3 ± 0.2
$m_{\gamma_d} = 1.2$ GeV	4.8 ± 0.3	11.6 ± 0.4	6.4 ± 0.3
$m_{\gamma_d} = 1.5$ GeV	1.8 ± 0.2	3.3 ± 0.2	1.7 ± 0.2
$m_{\gamma_d} = 2.0$ GeV	1.7 ± 0.2	3.4 ± 0.2	1.7 ± 0.2
Higgs MC ($n_{\gamma_d} = 4$)			
$m_{\gamma_d} = 0.4$ GeV	33.4 ± 13.7	158.4 ± 27.4	40.4 ± 14.2

CHAPTER 7

BACKGROUND ESTIMATION

Hadronic jets (QCD) are a cluster of hadrons produced in the proton-proton collision. Hadronic jets can fake an eLJ if a radiated photon from the cluster deposits its energy in the EM calorimeter and two hadronic tracks point to the EM cluster. If any of its hadron punch through to the muon system, a hadronic jet can fake a muLJ. If there is an EM cluster deposit and a hadron punch through to the muon system, a hadron jet can fake an emuLJ. The γ + jets are events with a photon and a jet of particles. The photon deposits its energy in the EM calorimeter. If there happen to be two hadronic tracks pointed at the EM cluster, the signature fakes an eLJ. The W +jets, Z+jets, and γ^* +jets processes fake lepton jets when the W and Z bosons decay leptonically. Diboson processes from $W+W$, $W+Z$, $Z+Z$ fake lepton jets when the W and Z bosons decay leptonically. The $\gamma\gamma$ can decay to electron-positron or muon-antimuon, thus faking lepton jets. ATLAS generated Monte Carlo samples and QCD di-jet data samples are used to study the characteristics of backgrounds and their contribution after the analysis selection cuts are applied. The detailed list of background processes that can fake lepton-jets is shown in Table 5.1.

7.1 Background contribution

Contribution from various background processes after imposing all analysis selection cuts are listed in Tables 7.1 and 7.2. All background contributions listed in Tables 7.1 and 7.2 are based on the MC simulations. In the LHC, QCD processes dominate due to its higher production cross section, but the number of events surviving the cuts in QCD MC sample is too small to provide an useful background estimate. Therefore, background estimation from the processes involving QCD jets in the final states are based on the data-driven method discussed in Section 7.2.

'

Table 7.1. Event yields for background MC sample after all analysis selection cuts. The columns correspond to eLJ-eLJ, muLJ-muLJ, and eLJ-muLJ channels. All yield correspond to 20.3 fb^{-1} luminosity and "-" means no events are left in the MC sample after applying the selection cuts.

	eLJ-eLJ	muLJ-muLJ	eLJ-muLJ
QCD	0.7 ± 0.7	-	-
γ+jets	-	-	0.1 ± 0.1
W+jets	-	-	-
$Z/\gamma^*(\geq 60\text{GeV})$+jets	-	-	-
$t\bar{t}$	-	-	-
$W + W$	-	-	-
$W + Z/\gamma^*$	0.1 ± 0.1	-	-
$Z/\gamma^* + Z/\gamma^*$	0.3 ± 0.1	1.5 ± 0.3	0.4 ± 0.1
$\gamma\gamma$	1.3 ± 0.5	-	-
$\gamma^*([10, 60]\text{GeV})$+jet	-	-	-
$\gamma^*([2, 8]\text{GeV})$+jet	-	-	-

Table 7.2. Event yields for background MC samples after all analysis selection cuts. The columns correspond to eLJ-emuLJ, muLJ-emuLJ, and emuLJ-emuLJ channels. All yield correspond to 20.3 fb^{-1} luminosity and "-" means no events are left in the MC sample after applying the selection cuts.

	eLJ-emuLJ	muLJ-emuLJ	emuLJ-emuLJ
QCD	-	-	-
γ+jets	-	-	-
W+jets	-	-	-
$Z/\gamma^*(\geq 60\text{GeV})$+jets	-	-	-
$t\bar{t}$	-	-	0.4 ± 0.3
$W + W$	-	-	-
$W + Z/\gamma^*$	-	-	-
$Z/\gamma^* + Z/\gamma^*$	-	0.1 ± 0.1	-
$\gamma\gamma$	-	-	0.2 ± 0.2
$\gamma^*([10, 60]\text{GeV})$+jet	-	-	-
$\gamma^*([2, 8]\text{GeV})$+jet	-	-	-

7.2 Data-driven estimate of background using ABCD method

The ABCD method [49] for background estimation makes use of two uncorrelated discriminating variables that have good discriminating power against the background. Figure 7.1, shows a toy scatter plot in a 2D discriminating variable (x-y) space, which illustrates the behavior of discriminating variables for a sample with signal and background components. All analysis cuts are applied except for the two variables. The black vertical and the horizontal line are where cuts are placed for the toy discriminants x and y. The cuts define four regions in a two-dimensional space. Region A is the signal region, where signal events (blue) are concentrated. Regions B, C, and D are control/background regions where background events (red) dominate.

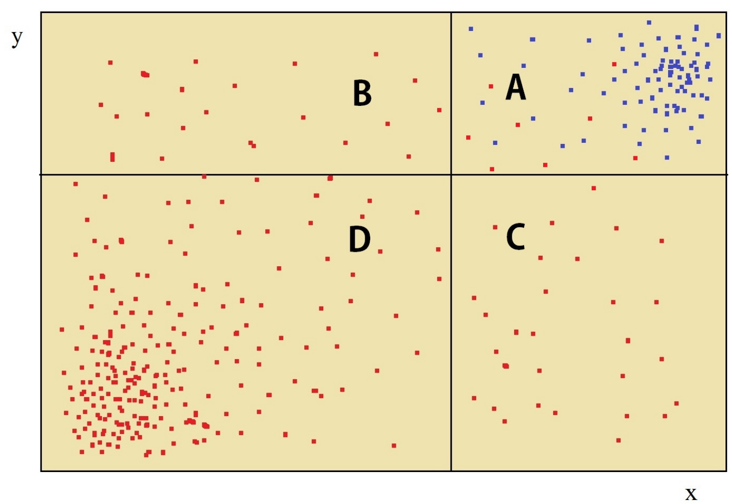

Figure 7.1. Cartoon showing A, B, C, and D regions formed by dividing the 2-dimensional variable space. Red points are background and blue points are signal.

If the two variables are uncorrelated for background processes, and if there is no signal leakage to the background dominated regions (*i.e.* no signal events in regions B, C, and D regions), then the amount of QCD di-jet background in the signal region can be estimated by the simple ABCD method,

$$\frac{N_B \times N_C}{N_D} \tag{7.1}$$

where N_B, N_C and N_D denote the number of data events counted in regions B, C, and D respectively.

The signal region A for the data stream was intentionally hidden as seleciton criteria were optimized. During cut optimization, the simple ABCD method was used to estimate the background in the signal region, A.

The list of least correlated variables-pair used in each channel for the ABCD method is:

eLJ-eLJ: subleading LJ f_{EM} and f_{HT}
muLJ-muLJ: leading LJ calorimeter isolation and subleading LJ calorimeter isolation
eLJ-muLJ: eLJ's f_{EM} and muLJ's calorimeter isolation
eLJ-emuLJ: eLJ's f_{EM} and emuLJ's E_T^{had}
muLJ-emuLJ: muLJ's calorimeter isolation and emuLJ's track isolation
emuLJ-emuLJ: subleading emuLJ's E_{s1}^{max} and track isolation

Sophisticated method is used that treats signal leakage and correlation between variables. An extension to the simple ABCD method, the ABCD likelihood method, can be used to account for signal leakage and the correlation between the variables, and systematic uncertainties. ABCD likelihood method estimates the background by fitting a likelihood function to the observed number of events in each of the four regions. The expected event rates in each region is denoted by:

- $\mu_A = \mu^U + \mu$
- $\mu_B = \mu^U \tau_B + \mu b$
- $\mu_C = \mu^U \tau_C + \mu c$
- $\mu_D = \mu^U \tau_B \tau_C + \mu d$

where μ is the signal size in region A and μ^U is the background size in region A. The factors b, c, and d scale the signal to describe the signal contamination in the control regions B, C, and D. The nuisance parameter τ_B and τ_C describe the ratio of the background in the control regions (for example, τ_B = The number of BG events in region B / The number of BG events in region A). Signal and background estimates as well as the nuisance parameters are obtained from the maximum likelihood fit to the observed number of events (n_A, n_B, n_C, and n_D) in the four regions. The likelihood function is the product of the four likelihood functions in the four regions:

$$L(n_A, n_B, n_C, n_D|\mu) = \prod_{i=A,B,C,D} \frac{e^{-\mu_i}\mu_i^{n_i}}{n_i!} \tag{7.2}$$

Figures 7.2 - 7.7 show the scatter plot of the regions for each channel for signal MC simulations and for the QCD dominated di-jet data sample from JetTauEtmiss stream in the left and right plots, respectively.

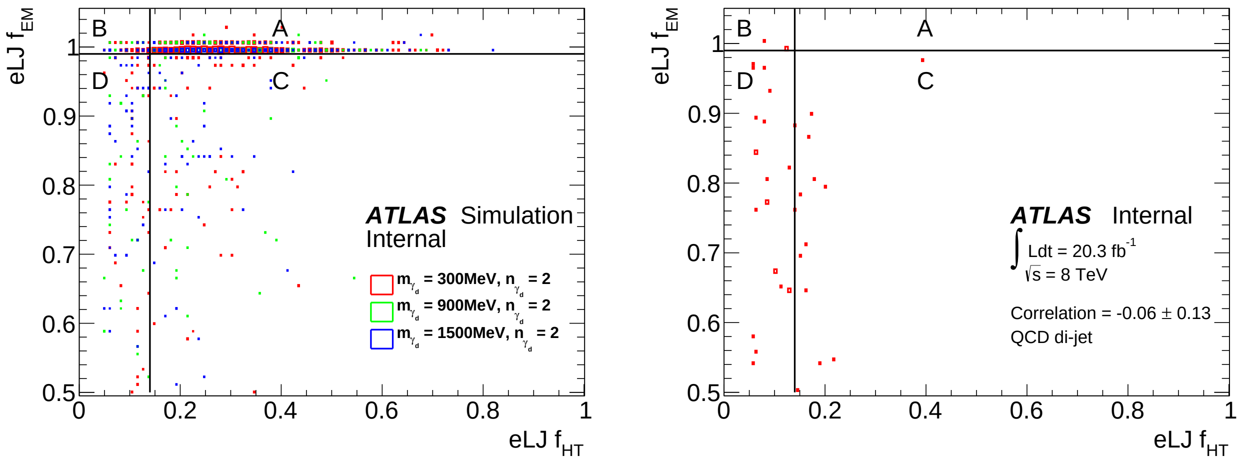

(a) (b)

Figure 7.2. Scatter plot of the variables used in the ABCD method for the eLJ-eLJ channel from signal MCs (left) and the QCD di-jet data (right). All selection requirements from Table 6.1 have been applied except for the two discriminating variables. The horizontal and the vertical black lines indicate the cut value. Nearly all signal events are found in region A, whereas the background is concentrated in regions B, C and D.

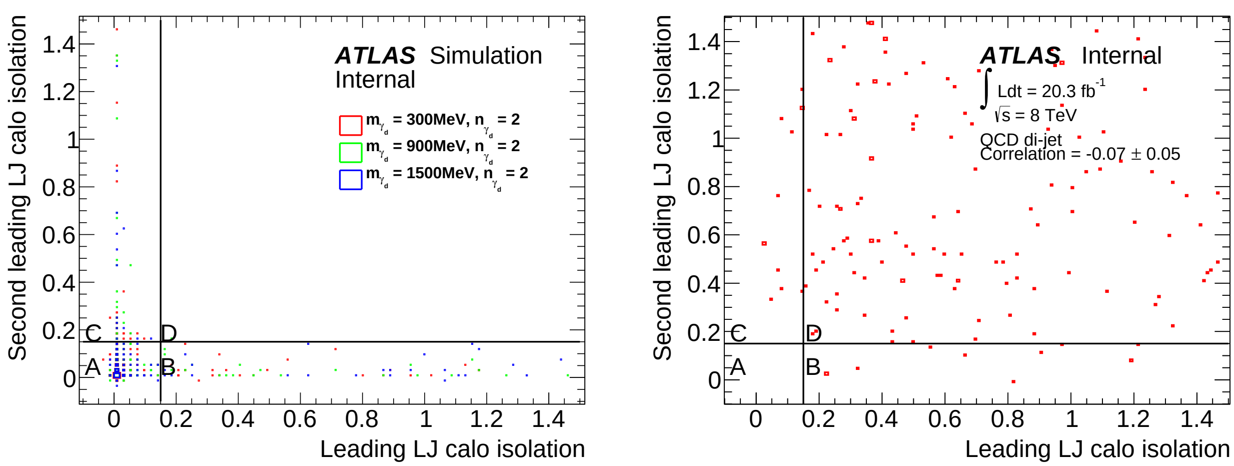

(a) (b)

Figure 7.3. Scatter plot of the variables used in the ABCD method for the muLJ-muLJ channel from signal MCs (left) and the QCD di-jet data (right). All selection requirements from Table 6.1 have been applied except for the two discriminating variables. The horizontal and the vertical black lines indicate the cut values. Nearly all signal events are found in region A, whereas the background is concentrated in regions B, C and D.

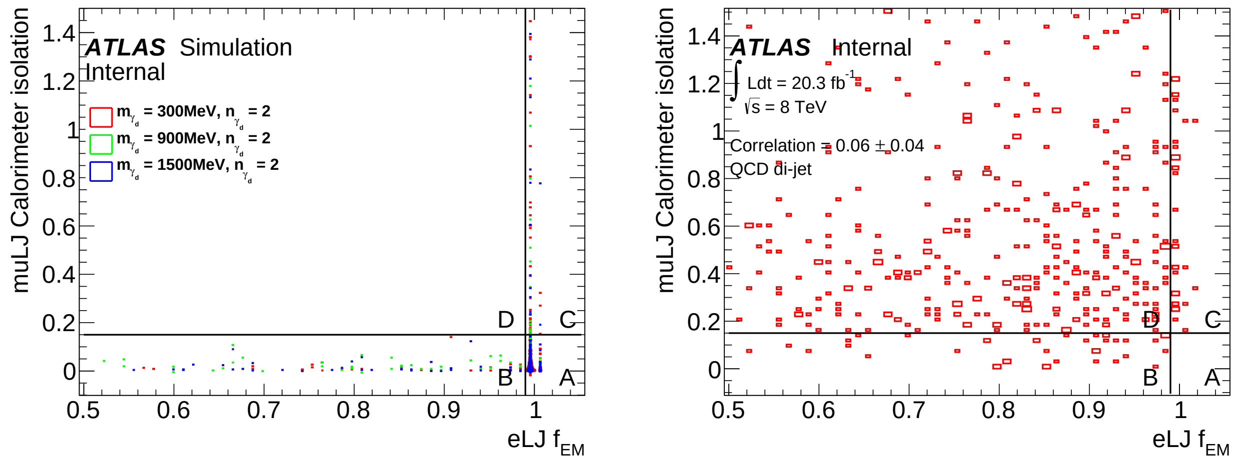

(a) (b)

Figure 7.4. Scatter plot of the variables used in the ABCD method for the eLJ-muLJ channel from signal MCs (left) and the QCD di-jet data (right). All selection requirements from Table 6.1 have been applied except for the two discriminating variables. The horizontal and the vertical black lines indicate the cut values. Nearly all signal events are found in region A, whereas the background is concentrated in regions B, C and D.

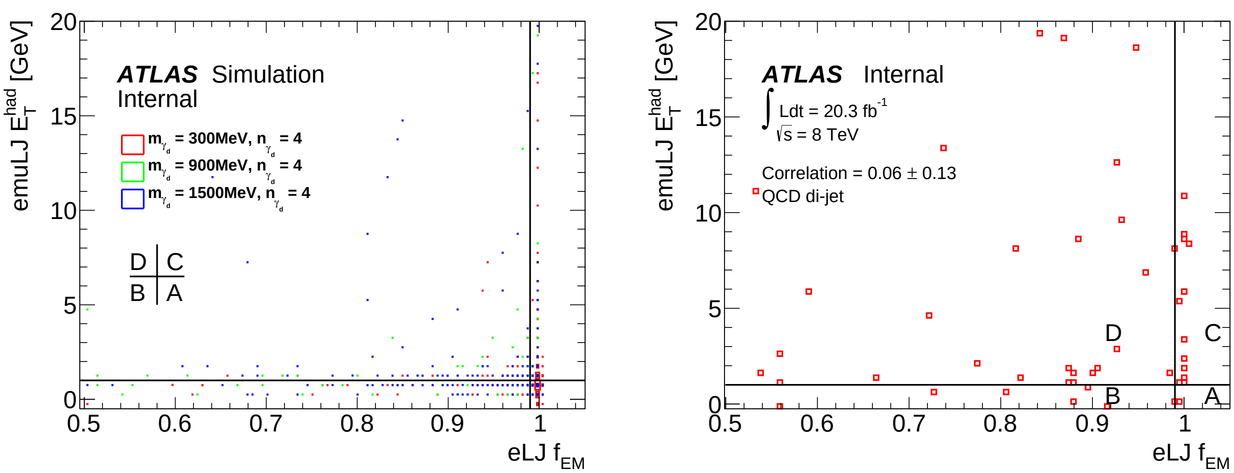

(a) (b)

Figure 7.5. Scatter plot of the variables used in the ABCD method for the eLJ-emuLJ channel from signal MCs (left) and the QCD di-jet data (right). All selection requirements from Table 6.1 have been applied except for the two discriminating variables. The horizontal and the vertical black lines indicate the cut values. Nearly all signal events are found in region A, whereas the background is concentrated in regions B, C and D.

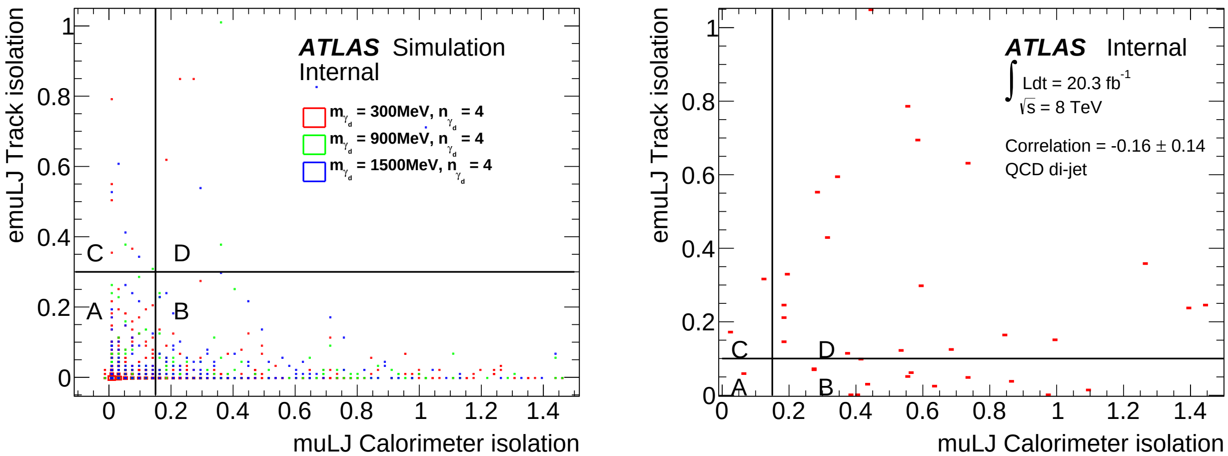

(a) (b)

Figure 7.6. Scatter plot of the variables used in the ABCD method for the muLJ-emuLJ channel from signal MCs (left) and the QCD di-jet data (right). All selection requirements from Table 6.1 have been applied except for the two discriminating variables. The horizontal and the vertical black lines indicate the cut values. Nearly all signal events are found in region A, whereas the background is concentrated in regions B, C and D.

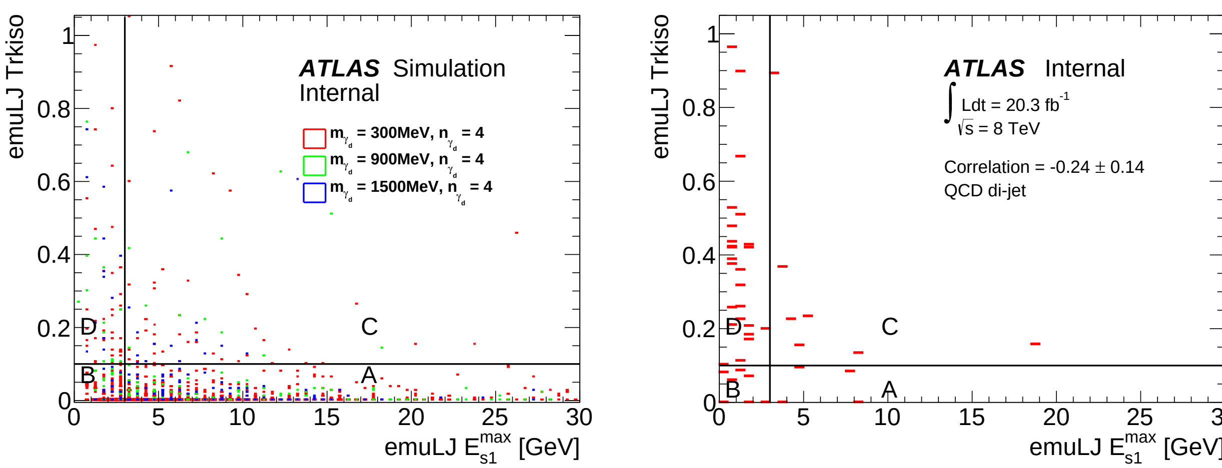

(a) (b)

Figure 7.7. Scatter plot of the variables used in the ABCD method for the emuLJ-emuLJ channel from signal MCs (left) and the QCD di-jet data (right). All selection requirements from Table 6.1 have been applied except for the two discriminating variables. The horizontal and the vertical black lines indicate the cut values. Nearly all signal events are found in region A, whereas the background is concentrated in regions B, C and D.

To validate the ABCD likelihood method, one of the control regions, region D of the QCD di-jet data from all channels is used. The region D is divided into four sub-regions: D1, D2, D3, D4. In the eLJ-eLJ channel (Figure 7.2b), region D1 is defined by $0.07 < f_{HT} < 0.14$ and $0.85 < f_{EM} < 0.99$, is treated as the signal region although it should have no signal contribution. Regions D2, D3, D4 are treated as the control regions. The observed number of events in all four regions, and the estimated amount of events in D1 using the ABCD likelihood method is in Table 7.3.

Similarly, other channels are used to validate the ABCD likelihood machinery. For the muLJ-muLJ channel (Figure 7.3b)) D1 is defined: 0.15 < leading calo isolation < 0.5 and 0.15 < sub-leading calo isolation < 0.5. For the eLJ-muLJ channel (Figure 7.4b), region D1 is defined: $0.9 < f_{EM} < 0.99$ and 0.15 < leading calo isolation < 0.4. Due to limited statistics in D region for eLJ-emuLJ, muLJ-emuLJ, and emuLJ-emuLJ channels the entire ABCD plane of the QCD di-jet data is used for the validation. Compared to the actual number of observed events the ABCD likelihood method prediction agrees.

Table 7.3. Event yields in the sub-region D1 to D4 is used to validate the ABCD likelihood method. Last column shows the estimated amount of events in D1.

Channel	Observed events				Estimated events in D1
	D2	D3	D4	D1	
eLJ-eLJ	3	47	17	20	17.7 ± 3.9
muLJ-muLJ	68	87	254	20	21.9 ± 3.3
eLJ-muLJ	35	43	89	14	15.4 ± 3.1
	B	C	D	A	Estimated events in A
eLJ-emuLJ	6	29	19	2	2.4 ± 0.3
muLJ-emuLJ	46	23	187	4	5.1 ± 1.1
emuLJ-emuLJ	6	3	9	1	1.4 ± 0.8

Figure 7.8 - 7.10 shows scatter plot of the ABCD variables from the search stream data.

Table 7.4 shows the data-driven estimate of QCD background in region A for all six channels. The middle column in Table 7.4 shows the background estimate using the simple ABCD method. The last column summarizes the QCD background estimate using the ABCD likelihood method. The simple ABCD and the ABCD likelihood method give consistent

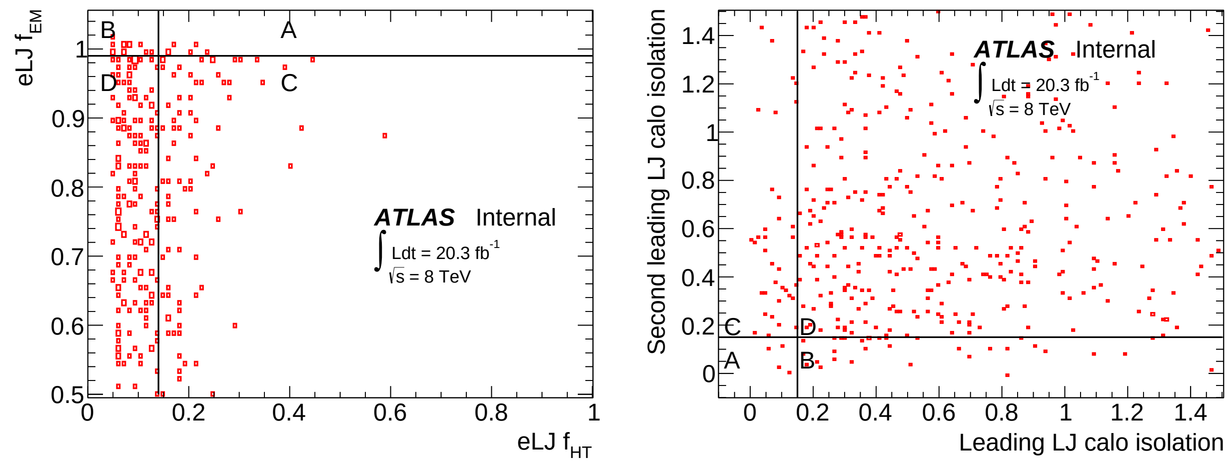

Figure 7.8. Scatter plot of the variables used for the ABCD method for (left) eLJ-eLJ, (right) muLJ-muLJ. In case of eLJ–eLJ channel, the f_{HT} cut is applied to two leading tracks in eLJ for the signal region A. The horizontal and the vertical black lines indicate the cut values on both the variables, as indicated in Table 6.1.

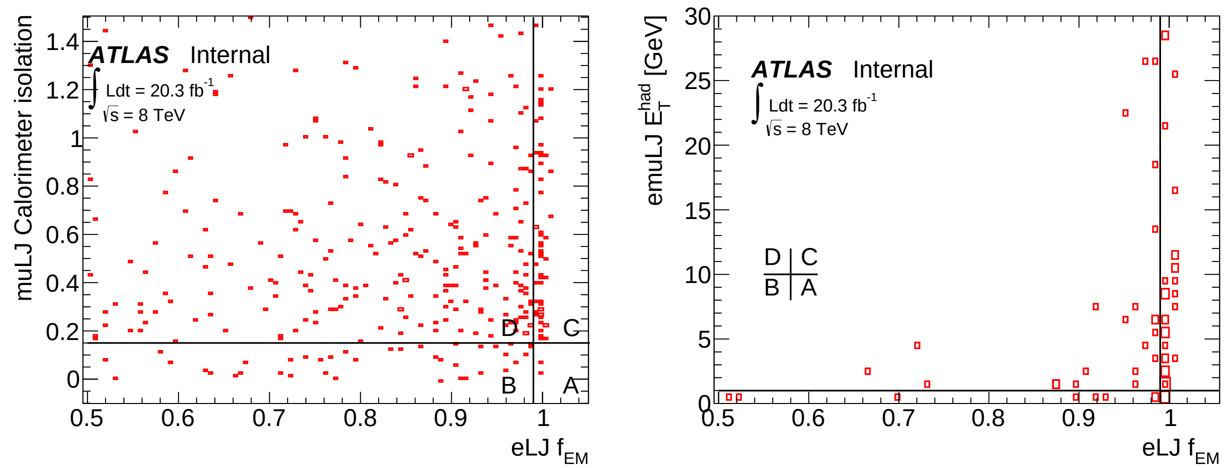

Figure 7.9. Scatter plot of the variables used for the ABCD method for (left) eLJ-muLJ, (right) eLJ-emuLJ. The horizontal and the vertical black lines indicate the cut values on both the variables, as indicated in Table 6.1.

estimates of the QCD di-jet background contributions to region A. The ABCD likelihood method is preferred as it allows for signal leakage into regions B, C, and D, and it allows for the small correlation for discriminating variables.

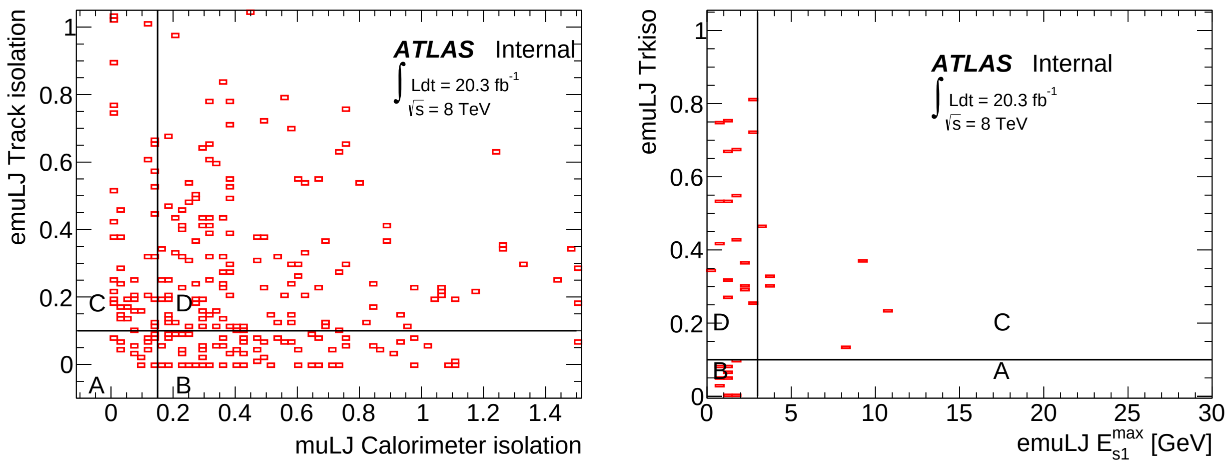

Figure 7.10. Scatter plot of the variables used for the ABCD method for (left) muLJ-emuLJ, (right) emuLJ-emuLJ. The horizontal and the vertical black lines indicate the cut values on both the variables, as indicated in Table 6.1.

Table 7.4. The amount of background in the signal region A is estimated using simple ABCD method (Eqn. 7.1) and the ABCD likelihood method. The simple ABCD method does not subtract out small background contributions estimated from the MC di-boson processes in the control regions, while the ABCD likelihood method takes them into account.

Channel	μ^U estimation using simple ABCD method	μ^U estimation using ABCD likelihood method
eLJ-eLJ	3.1 ± 0.8	2.9 ± 0.9
muLJ-muLJ	3.1 ± 0.6	2.9 ± 0.6
eLJ-muLJ	9.7 ± 1.9	6.7 ± 1.4
eLJ-emuLJ	16.7 ± 6.5	7.8 ± 2.0
muLJ-emuLJ	26.9 ± 5.4	20.2 ± 4.5
emuLJ-emuLJ	3.0 ± 1.7	1.3 ± 0.8

CHAPTER 8

RESULTS

In the previous chapter, Chapter 7, we have discussed the contribution from various background processes in the signal region. The next step is to compare the observed number of events from the search stream data in the signal region A with the estimated background. An excess of events in region A above the estimated background would be the signature of a discovery. If the observed number of data events are consistent with the background estimation, then the result would be interpreted as upper limits on the signal production cross section.

Table 8.1 shows the estimated QCD di-jet background using the data-driven ABCD likelihood background estimation method, the total estimated background (QCD di-jet estimation + MC contribution from other background processes like diboson prediction), and the observed data events in the signal region for all six lepton-jet pair channel.

Table 8.1. Total estimated background in signal region, A and the observed number of data events for each lepton-jet pair channel.

Channel	QCD di-jet background	Total background in region A	Observed events from the data
eLJ-eLJ	2.9 ± 0.8	4.4 ± 1.1	6
muLJ-muLJ	2.9 ± 0.6	4.4 ± 1.0	4
eLJ-muLJ	6.7 ± 1.4	7.1 ± 1.4	2
eLJ-emuLJ	7.8 ± 2.0	7.8 ± 2.0	5
muLJ-emuLJ	20.2 ± 4.5	20.3 ± 4.5	14
emuLJ-emuLJ	1.3 ± 0.8	1.9 ± 0.9	0

The observed number of data events in region A (last column in Table 8.1) is consistent with the estimated total background (last but one column in Table 8.1). Thus there is no discovery of dark photons decaying to lepton-jet final state for the parameters of interest.

Thus 95% Confidence Level (CL) upper limits is placed on the production cross-section times the branching fraction of the signal.

Consider $N = S + B$, where S is the poisson pdf of signal processes with a mean number of events s and B is the poisson pdf of background processes with a mean number of events b. If the observed number of data events in regions A (n_{obs}) is consistent with b, then upper limit is placed on the signal size. To get a 95% CL upper limit on the signal size, a value of s is found such that there is 5% probability to find n events as low as what is observed.

$$P(n \leq n_{obs}; s, b) = \sum_{n=0}^{n_{obs}} \frac{(s+b)^n}{n!} e^{-(s+b)} \tag{8.1}$$

Solving Eqn. 8.1 with $P = 0.05$ (95% CL) for s (in other words N_{limit}), gives the upper limit on the signal expectation. The upper limit is expressed in signal cross-section times the branching fraction, which is achieved by

$$\sigma \times BR = \frac{N_{\text{limit}} \times \sigma_{\text{Theory}} \times BR_{\text{Theory}}}{N_{\text{expected}}} \tag{8.2}$$

where N_{limit} is the upper limit on the signal, BR_{Theory} and σ_{Theory} denote the theoretical branching fraction of the dark photon (Table 6.2) and cross section from either the SUSY (64 fb) or Higgs (19.2 pb) production cross section, respectively, and N_{expected} is the signal MC expectation in region A as expressed in Eqn. 6.2. There are systematic uncertainty associated with each term in Eqn. 6.2.

8.1 Systematic uncertainties

In this section we discuss the systematic uncertainties affecting the signal and background expectations are discussed.

Luminosity:

The integrated luminosity of Eqn. 3.1 is determined as discussed in [26]. Systematic uncertainty associated with the integrated luminosity determination is 2.8% [26].

Trigger:

The systematic uncertainty of the e60_medium1 and g35_loose_g25_loose triggers derives from the requirement of a 'medium' OR 'loose' quality cluster, which impacts the signal efficiency. Modeling of these triggers is studied using background MC samples and data. The probability of an eLJ to have a 'medium' or 'loose' quality cluster is plotted as a function of the opening angle of the tracks in an eLJ. A straight line fit to this probability ratio is used to estimate the uncertainty for the 'medium or 'loose' quality requirement. The probability values are given in Table D.4. The trigger efficiency uncertainty of signal events selected with single electron trigger e60_medium1 is 8% and the events selected with g35_loose_g25_loose trigger is 17%. The total uncertainty for the signal yields after requiring the OR of those triggers ranges 8.6% to 13.5%, as described in Table D.4.

The systematic uncertainty for the multi-muon triggers (2mu13 and 3mu6_MSOnly) efficiency comes from modeling the overlaid muons that may be identified as single muon at Level 1 trigger filtering. The systematics uncertainty associated with the single muon trigger mu36_tight is small (0.6%), as described in [66]. The larger of two uncertainties for single and multi-muon triggers is considered for the systematic uncertainty associated with the multi-muon triggers as that is applied in Ref. [5]. This uncertainty is 5.8% of the signal acceptance.

The systematic uncertainty due to triggers (e60_medium1, mu36_tight, and 2mu13) used in the mixed channel selection is evaluated as the weighted average uncertainty from the uncertainties associated with each of those triggers. As listed in Table D.5, this uncertainty ranges from 3.3% to 5.4% depending on the γ_d mass for the mixed channels having eLJ-muLJ and muLJ-emuLJ combinations. For other mixed channels (eLJ-emuLJ and emuLJ-emuLJ) the uncertainty ranges from 3.1% to 4.8%.

Lepton energy/momentum scales and resolution:
The effect of the electron energy scale on the signal MC acceptance is estimated by varying the given energy of the electron cluster in an eLJ by $\pm 1\sigma$ and evaluating the final signal event yield. The difference in signal event yield from the nominal (signal event yield without varying the energy of the cluster, Tables 6.4 and 6.5) is assigned as the systematic uncertainty due to electron energy scaling. It is determined to be less than 0.1%. The systematic uncertainty associated with the muon energy scale is estimated through a similar procedure and evaluated to be in the range 1.9% to 5.2% depending on the mass point.

Track reconstruction at small opening angle:
The systematic uncertainty due to the modeling on track reconstruction at small opening angle is estimated by studying the track reconstruction efficiency difference between data and

MC samples. The efficiency is measured using the reconstructed $J/\psi \rightarrow \mu^+\mu^-$ candidates with a small ΔR between two muons in the data and MC samples. Figure D.1 shows the track reconstruction efficiency from the J/ψ sample as a function of opening angle of the muons. A 8.4% systematic uncertainty is assigned due to mis-modeling of track reconstruction at small opening angle.

Muon reconstruction at small opening angle:
The systematic uncertainty for muon reconstruction in the muon spectrometer at small opening angle is taken from Ref. [5] to be 5.4%.

LJ variables:
The systematic uncertainties for each eLJ variable (f_{HT}, E_{s1}^{max}, f_{s3}, f_{EM} and track isolation) and emuLJ variable (E_T^{had}, f_{s3}, E_{s1}^{max} and track isolation) is assigned based on the cut efficiency difference for each of those variables between the data and MC samples containing $Z \rightarrow e^+e^-$ events, as discussed in Section D.3. The systematic uncertainties for each muLJ variable (track isolation and calorimeter isolation) are obtained based on the cut efficiency difference for each of those variables between the data and MC samples using $J/\psi \rightarrow \mu\mu$ events. The systematic uncertainties for the six type of LJ pairs are found in Table 8.2.

Table 8.2. The systematic uncertainty associated with the signal acceptance due to the discriminating variables in the six type of LJ pairs. All the other variables are found to be independent of the average number of interactions per bunch crossings.

Variables	Systematics uncertainties associated with the discriminating variables in each final state					
	eLJ-eLJ	muLJ-muLJ	eLJ-muLJ	eLJ-emuLJ	muLJ-emuLJ	emuLJ-emuLJ
f_{HT}	0.4 %	-	0.2 %	0.2 %	-	-
Track isolation	9.2 %	17.0 %	13.0 %	9.2 %	13.0 %	9.2 %
E_{s1}^{max}	0.2 %	-	0.1 %	1.1 %	1.0 %	2.0 %
f_{s3}	12.9 %	-	6.0 %	9.7 %	3.3 %	6.8 %
E_T^{had}	-	-	-	0.1 %	0.1 %	0.2 %
f_{EM}	0.9 %	-	0.4 %	0.4 %	-	-
Muon calo isolation	-	6.7 %	3.3 %	-	3.3 %	-

Background systematics:
The two discriminating variables used in the ABCD data-driven background estimation show a small correlation of 6% in all LJ pair types except emuLJ-emuLJ, which has 24±14% due to limited statistics. The effect of this correlation is incorporated in the background estimation using the ABCD likelihood method. An additional 4.5% uncertainty is assigned to the background estimate due to a small pile-up dependence of the track isolation variable.

8.2 Limits

As the observed number of data events is in good agreement with the estimated mean background (Table 8.1), there is no sign of signal in the data. Hence, a 95% Confidence Level (CL) upper limit on the production cross section times branching fraction of at least two lepton-jets in the final state is placed. The limits are expressed for the theoretical models considered:

Squark + Squark $\rightarrow 2\gamma_d + \mathrm{X}$,
Squark + Squark $\rightarrow 2(s_d \rightarrow \gamma_d\gamma_d) + \mathrm{X}$,
Higgs $\rightarrow 2\gamma_d + \mathrm{X}$ and
Higgs $\rightarrow 2(s_d \rightarrow \gamma_d\gamma_d) + \mathrm{X}$

processes in the electron, muon and mixed channels.

The numbers in the Tables E.1 - E.6 show the 95% CL upper limits on signal expectation (μ), which are expressed in terms of cross section times branching fractions (BR) using Eqn. 8.2 for two lepton-jets productions and are plotted graphically for SUSY mediated topology as shown in Figures 8.1-8.5 as a function of γ_d mass.

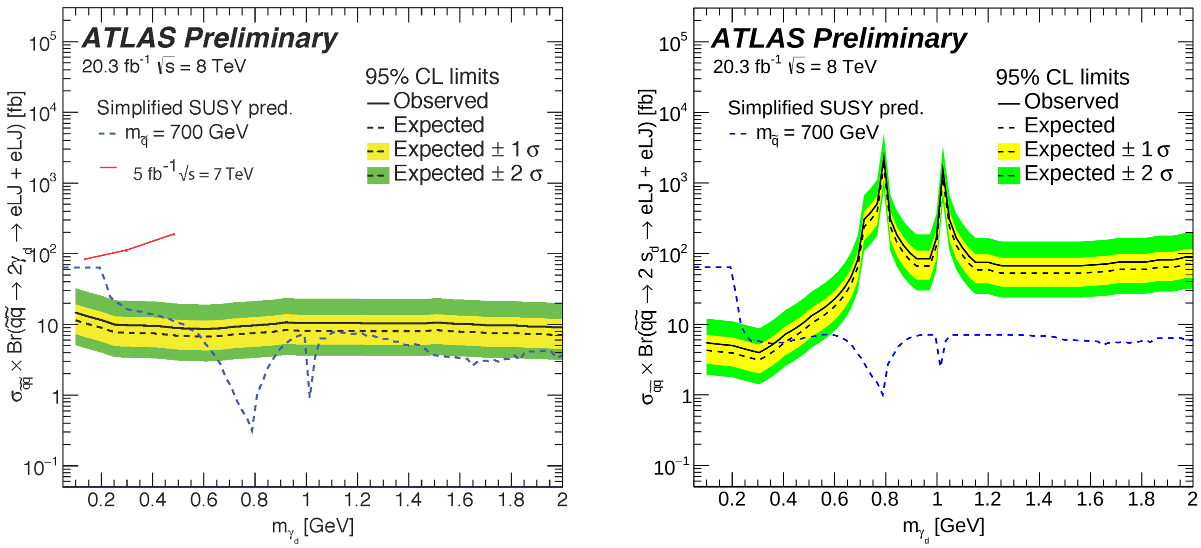

Figure 8.1. The 95% CL observed and expected upper limit on the cross section times branching fraction into two lepton-jets final states in the cases of 2 γ_d + X and 2($s_d \to \gamma_d\gamma_d$) + X productions via SUSY portal topologies in the eLJ–eLJ channel.

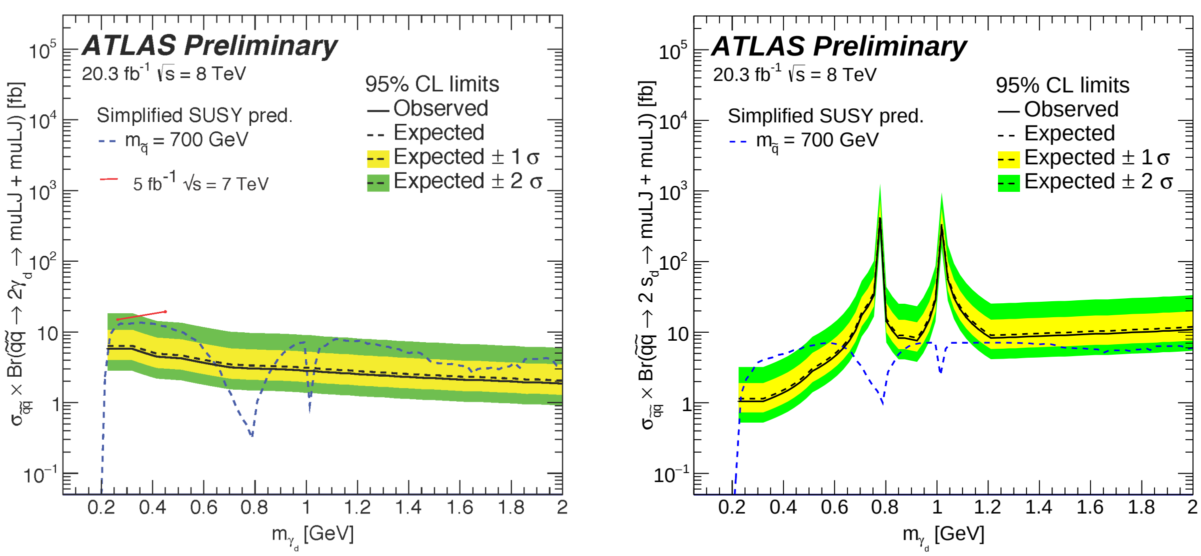

Figure 8.2. The 95% CL observed and expected upper limit on the cross section times branching fraction into two lepton-jets final states in the cases of 2 γ_d + X and 2($s_d \to \gamma_d\gamma_d$) + X productions via SUSY portal topologies in the muLJ–muLJ channel.

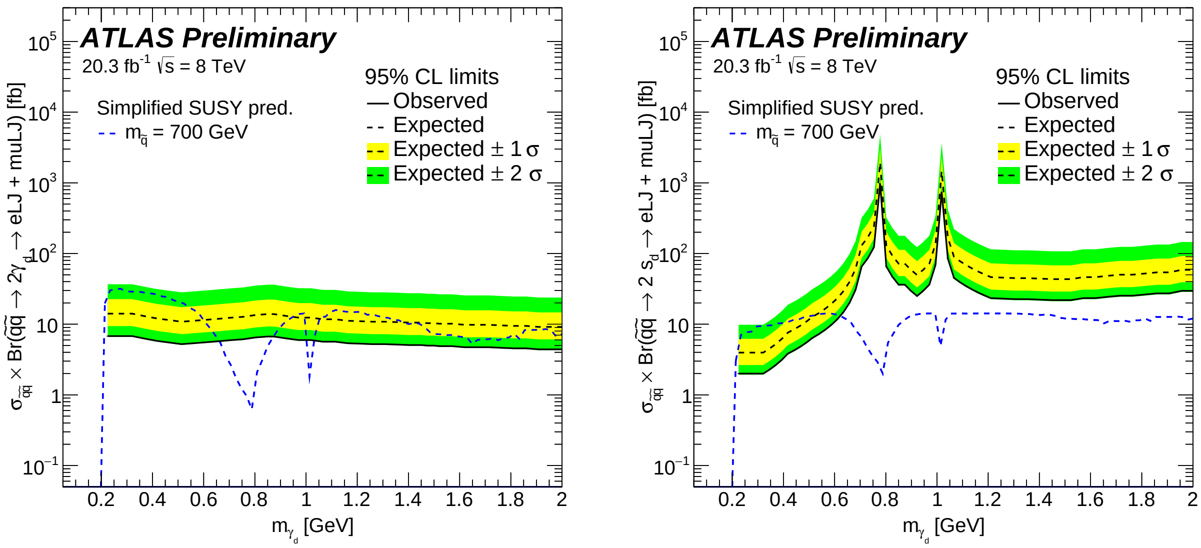

Figure 8.3. The 95% CL observed and expected upper limit on the cross section times branching fraction into two lepton-jets final states in the cases of 2 γ_d + X and $2(s_d \rightarrow \gamma_d\gamma_d)$ + X productions via SUSY portal topologies in the eLJ–muLJ channel.

The upper limit on the expected number of signal events may be interpreted as the 2-dimensional exclusion contour in the kinetic mixing parameter ϵ and γ_d mass plane for the $H \rightarrow 2\gamma_d + \text{X}$ topology. As only one mass benchmark ($\gamma_d = 0.4$ GeV) sample was generated for $H \rightarrow 2\gamma_d+\text{X}$ topology, the nominal signal efficiencies for other γ_d mass points are inferred from the SUSY MC samples.

The kinetic mixing parameter ϵ is related to mean lifetime, τ, of the dark photon. As only two samples with $c\tau = 0$ mm and $c\tau = 47$ mm were generated for $H \rightarrow 2\gamma_d + \text{X}$ model, the nominal signal efficiencies for other $c\tau$ ranges are derived using pseudo experiments with different lifetime $c\tau$ ranging from 0 to 50 mm. The p_{T} spectra of $H \rightarrow 2\gamma_d + \text{X}$ with $c\tau = 0$ mm is used to extrapolate the efficiency for different $c\tau$ ranges from 0-50mm.

To be consistent with the other lepton-jet analysis interpretation, a 90% CL exclusion limits is derived on $H \rightarrow 2\gamma_d+\text{X}$ production for various (5%, 10%, 20%, 40%) branching fractions. The final limit is obtained by combining the results from the eLJ–eLJ, muLJ–muLJ and eLJ–muLJ channels. Figure 8.6 shows the 90% CL exclusion contour interpreted in the ϵ and γ_d mass plane. The parameter space that was excluded by this study ranges from 10^{-2} to 10^{-5} in ϵ and from 0.1 to 2 GeV in m_{γ_d}. In the low mass region below $\mu^+\mu^-$ threshold,

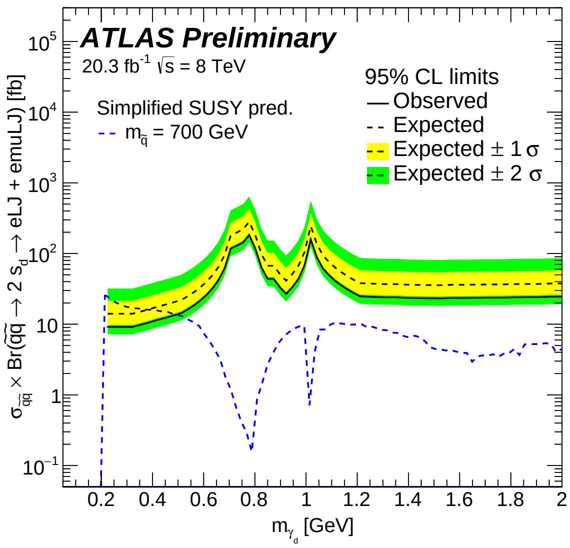

Figure 8.4. The 95% CL observed and expected upper limit on the cross section times branching fraction into eLJ–emuLJ final states for $2(s_d \to \gamma_d\gamma_d)$ + X SUSY topology. The observed upper limits are tighter than expected upper limit for all m_{γ_d}, except for 0.7 GeV mass, as the data has fewer events than the expected backgrounds in the signal region. Due to large signal leakage in 0.7 MeV benchmark with very small signal sensitivity, the observed limit gets weaker than expected limits.

only the results from eLJ–eLJ channel contributes, and therefore has smaller excluded area in ϵ range due to smaller signal efficiency. The excluded regions from the non-prompt lepton jet search at ATLAS [5] and from other experiments are also shown in Figure 8.6.

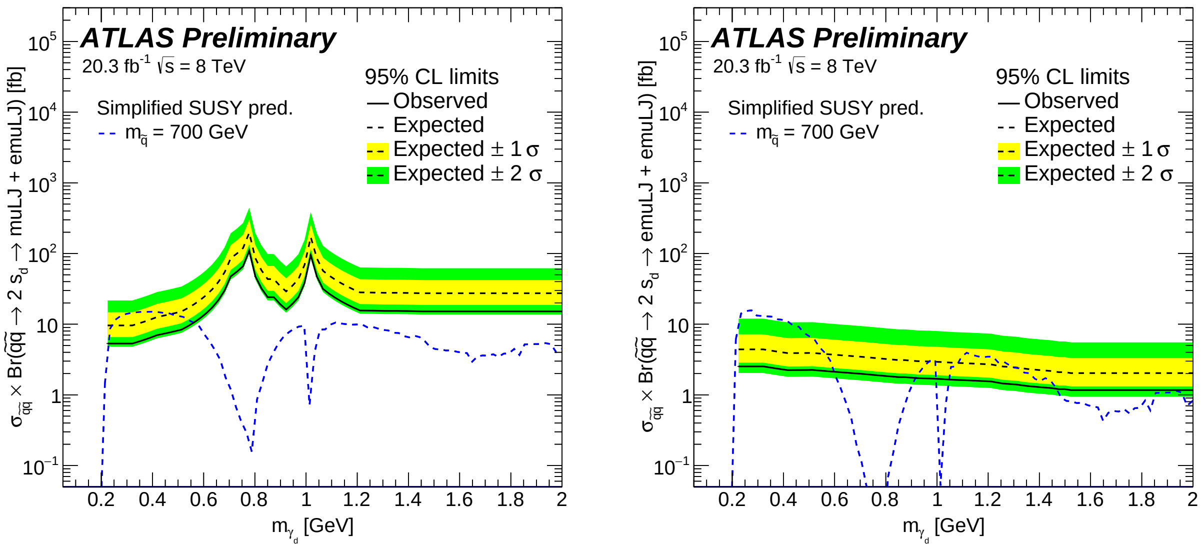

Figure 8.5. The 95% CL observed and expected upper limit on the cross section times branching fraction into muLJ–emuLJ (left) and emuLJ-emuLJ (right) final states for $2(s_d \to \gamma_d\gamma_d)$ + X SUSY topology. The observed upper limits are tighter than expected upper limit for all m_{γ_d}, as data has less events than background expectations in the signal region.

Table 8.3. This table shows efficiency for all generated signal benchmarks for the SUSY portal in $2\gamma_d$+X final state for eLJ–eLJ, muLJ–muLJ and eLJ–muLJ channels. Also, the extrapolated Higgs efficiency using the SUSY portal efficiency.

Signal benckmarks	eLJ–eLJ		muLJ–muLJ		eLJ–muLJ	
γ_d mass [GeV]	SUSY portal	Higgs portal	SUSY portal	Higgs portal	SUSY portal	Higgs portal
0.1	3.0%	0.32%	-	-	-	-
0.2	3.8%	0.37%	-	-	-	-
0.3	4.7%	0.50%	5.1%	1.8%	4.4%	0.31%
0.4	3.9%	0.33%	6.5%	1.9%	5.0%	0.34%
0.5	5.5%	0.40%	7.0%	2.2%	5.7%	0.39%
0.7	4.6%	0.20%	7.9%	1.4%	5.3%	0.44%
0.9	4.0%	0.34%	10.1%	2.6%	5.3%	0.31%
1.2	4.0%	0.21%	12.6%	2.7%	5.7%	0.26%
1.5	4.1%	0.19%	14.1%	2.7%	6.8%	0.32%
2.0	4.7%	0.20%	16.7%	3.9%	6.9%	0.27%

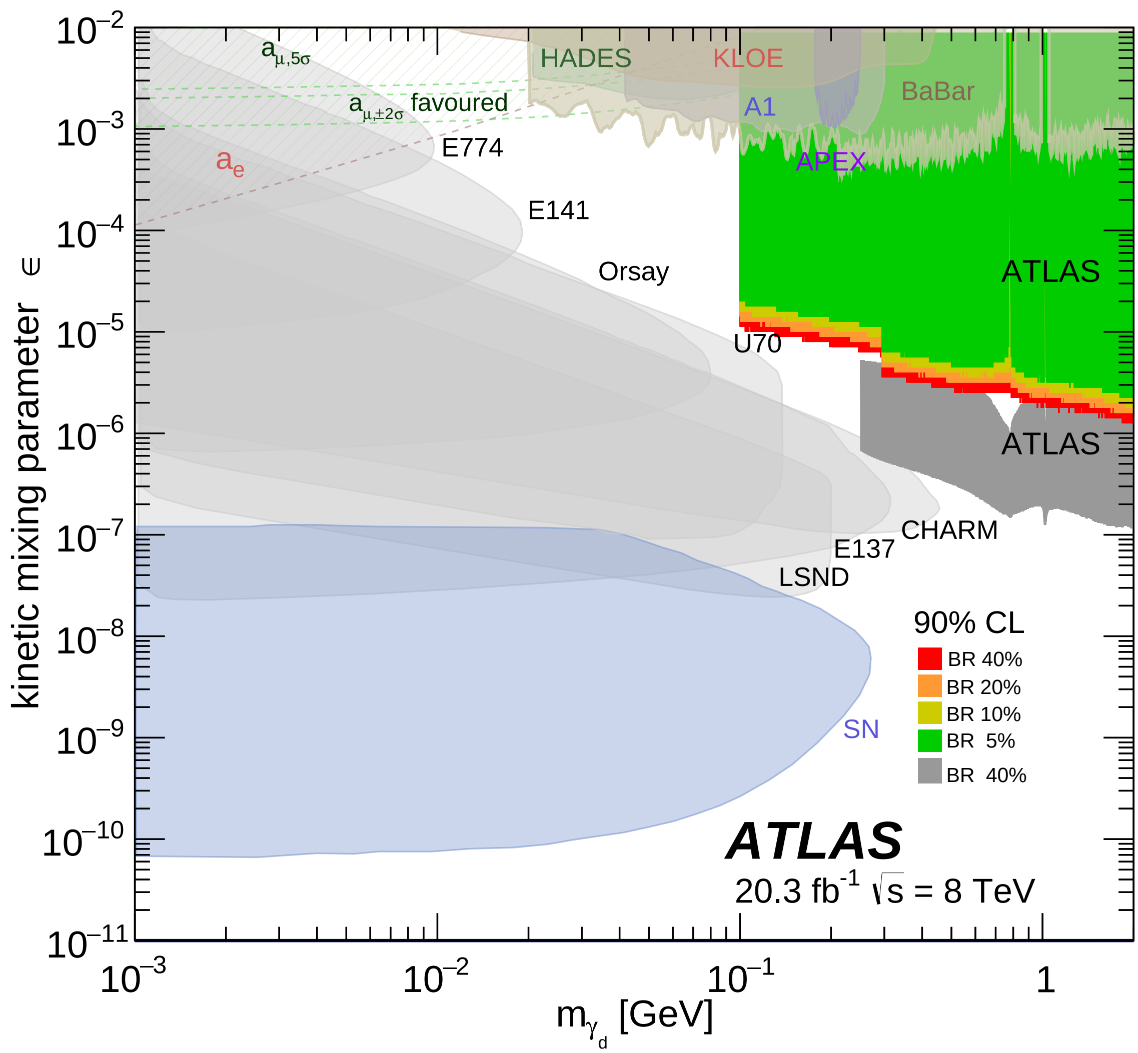

Figure 8.6. A 2-dimensional exclusion plot in m_{γ_d} and ϵ parameter space. This shows existing 90%CL exclusion regions from experiments E137, E141, and E774 [33, 35, 64], Orsay [41], U70 [34], CHARM [47], LSND [50], A1 [58], the electron and muon anomalous magnetic moment [42, 45, 62], HADES [14], KLOE [21], the test run results reported by APEX [10], an estimate using BaBar results [27, 55, 63], and constraints from astrophysical observations [43, 44]. Recent 90%CL exclusion contours from displaced lepton-jet search using 8 TeV ATLAS data are overlaid for 40% branching fractions of Higgs decaying into 2 γ_d + X [5]. The 90%CL exclusion region for prompt $H \rightarrow 2\gamma_d + X$ production with $5\%, 10\%, 20\%, 40\%$ branching fraction into 2 γ_d + X decay are extracted based on the present combined results from eLJ–eLJ, muLJ–muLJ and eLJ–muLJ channels using 8 TeV data at ATLAS, as shown in the upper green-shaded area.

CHAPTER 9

CONCLUSION

A search is performed for prompt lepton-jets containing either electrons, or muons, or a mixture using the 20.3 fb^{-1} of data collected with the ATLAS detector at the center of mass energy of 8 TeV. These lepton-jets are expected to be coming from the decay of a light-mass dark photon in the framework of dark sector models. The analysis is conducted in a model-independent way based on a general lepton-jet definition. Events were selected if they contained at least two lepton-jets satisfying selection criteria designed to discriminate them from background. The dominant QCD background in the signal region was determined using the data-driven ABCD method and small contributions from other background processes are determined from the MC simulations.

Table 9.1. Total estimated background in signal region A and the observed number of data events in region A for each lepton-jet pair channel.

Channel	Total background in region A	Observed events from the data
eLJ-eLJ	4.4 ± 1.1	6
muLJ-muLJ	4.4 ± 1.0	4
eLJ-muLJ	7.1 ± 1.4	2
eLJ-emuLJ	7.8 ± 2.0	5
muLJ-emuLJ	20.3 ± 4.5	14
emuLJ-emuLJ	1.9 ± 0.9	0

The observed number of events and the expected background are summarized in Table 9.1. The number of events found in data is compatible with the background estimate in the signal region, no sign of signal is found. Therefore, a 95% CL upper limits is placed on the production cross-section times branching fraction for two prompt lepton jets in the SUSY portal and the Higgs portal in all six channels. The results are also interpreted in terms of 90% CL exclusion region in kinetic mixing and m_{γ_d} parameter space, based on the combined results for $H \to \gamma_d\gamma_d$ + X production topology.

APPENDIX A

LEPTON-JET GUN - A PARTICLE GUN MC GENERATOR TOOL

Lepton-jet gun is a MC generator tool capable of generating a dark photon (γ_d) or a dark scalar $s_d \rightarrow \gamma_d\ \gamma_d$. The tool allows to generate samples with different s_d and γ_d masses and allows to tune the branching fraction of γ_d to ee, $\mu\mu$ or $\pi\pi$. Two different polarization of γ_d, longitudinal polarization (LP) and transverse polarization (TP) can be selected. This tool helps to understand the detector response to lepton-jets, thus helps in optimizing LJ reconstruction and selection cuts. Figure A.1 shows feynman diagram of (a) a single γ_d decays to a pair of leptons, (b) a dark scalar (s_d) decays to two γ_d s which then decay to a pair of leptons respectively.

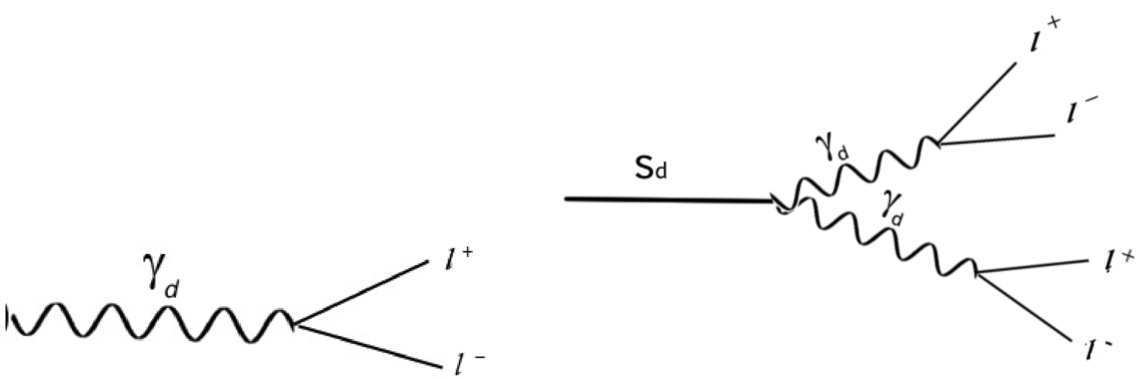

(a) (b)

Figure A.1. (a) A single dark photon decaying to a pair of leptons, (b) two dark photons from a dark scalar (s_d) decay to leptons.

Using LJ gun tool, two set of samples were generated. Single γ_d samples (Sec. A.1) and double γ_d samples (Sec. A.2).

A.1 Single γ_d sample

- 100000 events per sample

- m_{γ_d} = 0.05, 0.15, 0.4, 0.9, 1.2, 1.5, 2.0 GeV.
- γ_d parameters
  - p_{T}: 5 - 100 GeV flat
  - η: -2.5 to 2.5 flat
  - ϕ: -3.14 to 3.14 flat
  - A set of samples with transverse polarization for each mass value and the other set with longitudinal polarization.
  - Dark sector radiation $\alpha_d = 0$.

A.2 Single s_d sample, $s_d \rightarrow \gamma_d\ \gamma_d$

- 100000 events per sample.
- m_{s_d} = 1, 2, 5, 10 GeV
- s_d parameters
  - p_{T}: 5-100 GeV flat
  - η: -2.5 to 2.5 flat
  - ϕ: -3.14 to 3.14 flat
- m_{γ_d} = 0.05, 0.15, 0.4, 0.9, 1.2, 1.5, 2.0 GeV.
- γ_d parameters
  - No polarization.
  - Dark sector radiation $\alpha_d = 0$.

APPENDIX B

MODELING OF LEPTON-JETS VARIABLES IN THE QCD, Z AND PHOTOCONVERSION SAMPLES

The modeling of lepton-jets variables are checked using the background-like control samples (QCD di-jet), and signal-like samples, such as the Z and photoconversions events. The comparison of the distributions of discriminating variables is shown in Section D.3 from $Z \to e^+e^-$ events.

For the comparison of the eLJ and muLJ variables shapes in the QCD di-jet events, events containing two jets using the single jet triggers are selected, based on the average p_T of the two jets. Both jets must satisfy the standard 'medium' definition for jet quality, and are back-to-back ($\Delta\phi \geq 1.7$) with $p_T \geq 25$ GeV. In order to compare the shapes of eLJ variables, a tag jet is selected by matching it to the online trigger object within $\Delta R \leq 0.4$ and it must have electromagnetic fraction in the calorimeter less than 0.9. The other jet considered as the probe is matched to the eLJ. Figure B.2 shows the comparisons of shape of the eLJ variables in QCD di-jet events in the data and MC. In order to compare the shape of muLJ variables, a tag jet is selected by matching it to the online trigger object within $\Delta R \leq 0.4$ and it must not contain any muons. The other jet considered as the probe is matched to the muLJ. Figure B.1 shows the comparisons of shape of the eLJ variables in QCD di-jet events in the data and MC.

The eLJ variables distribution is also compared in the events containing at least two back-to-back converted photons with a minimum $E_T \geq 25$ GeV satisfying the standard "Tight" requirement. Events are selected in the data and MC, which have passed the OR of e60_medium1 and g35_loose_g25_loose triggers. Those photons are matched to the eLJ within $\Delta R < 0.5$. Figure B.4 shows the comparisons between the data and MC.

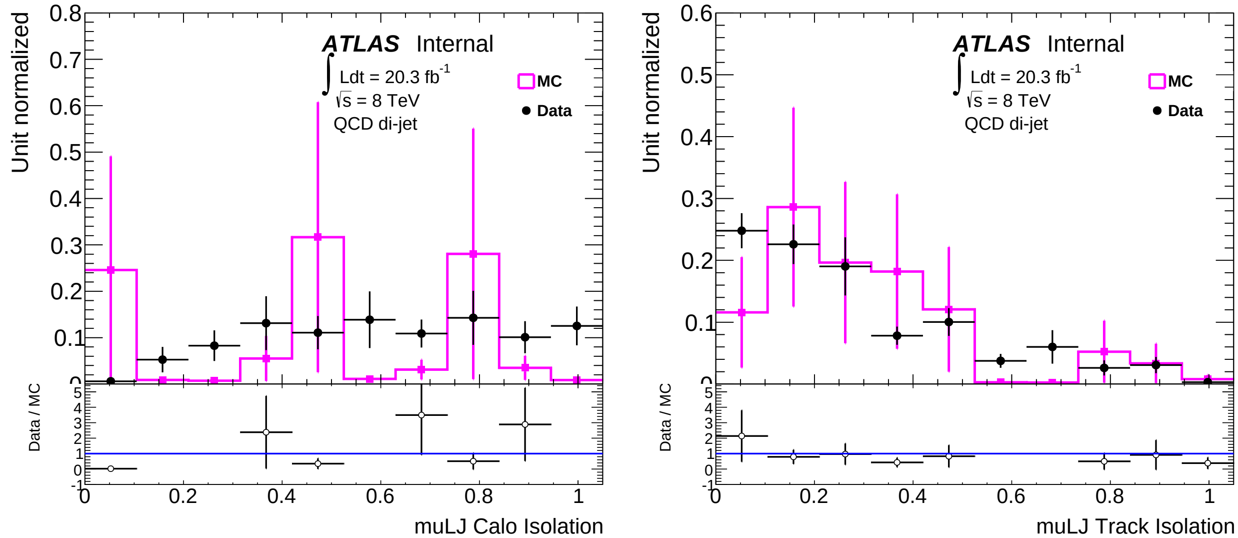

Figure B.1. Distributions of the discriminating variables from the QCD di-jet events show reasonable agreement between the data and MC samples for the muLJ matched to a QCD probe jet with $p_T \geq 25$ GeV.

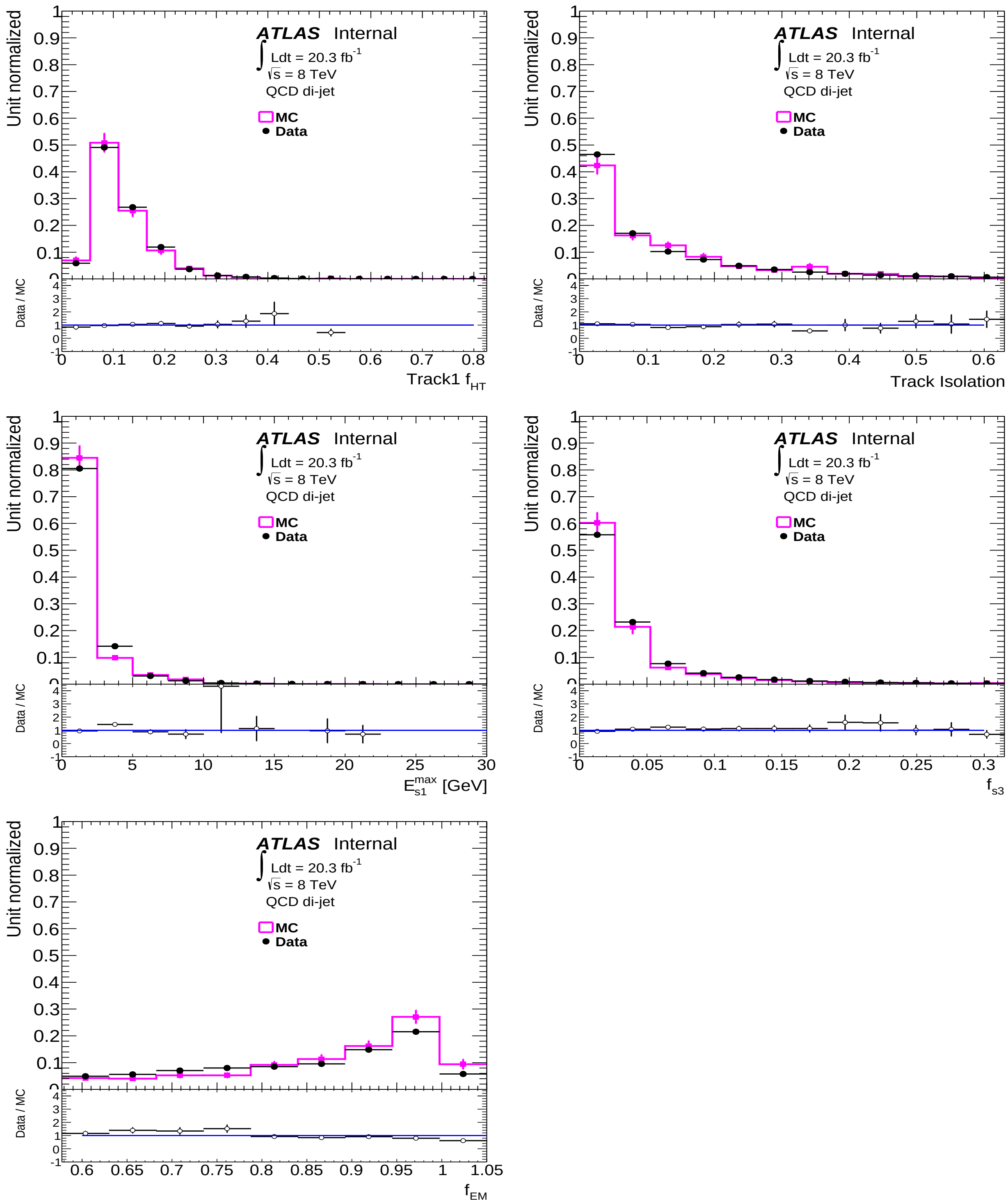

Figure B.2. Distributions of the discriminating variables from the QCD di-jet events show reasonable agreement between the data and MC samples for the eLJ matched to a QCD probe jet with $p_T \geq 25$ GeV.

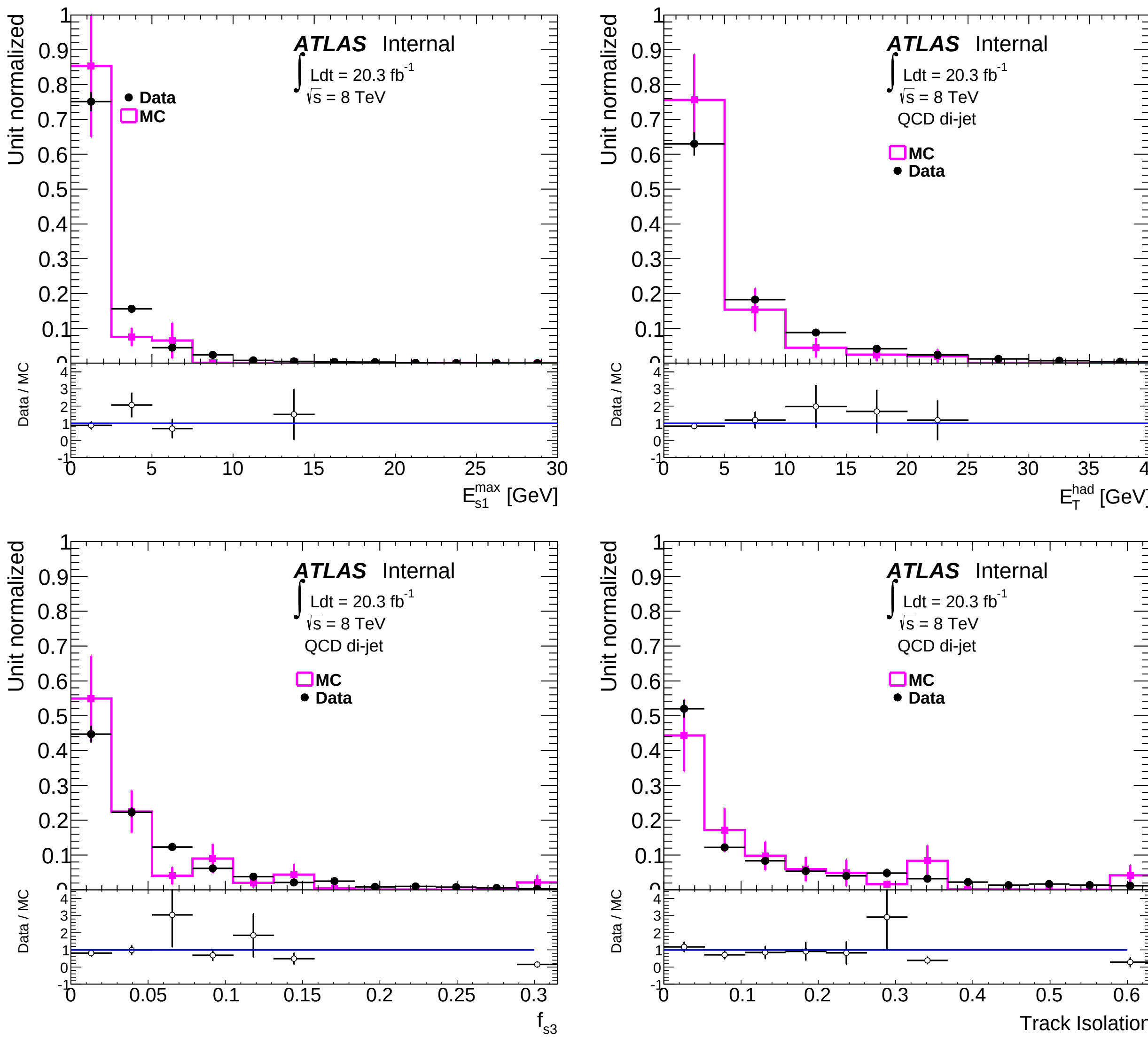

Figure B.3. Distributions of the discriminating variables from the QCD di-jet events show reasonable agreement between the data and MC samples for the emuLJ matched to a QCD probe jet with $p_T \geq 25$ GeV.

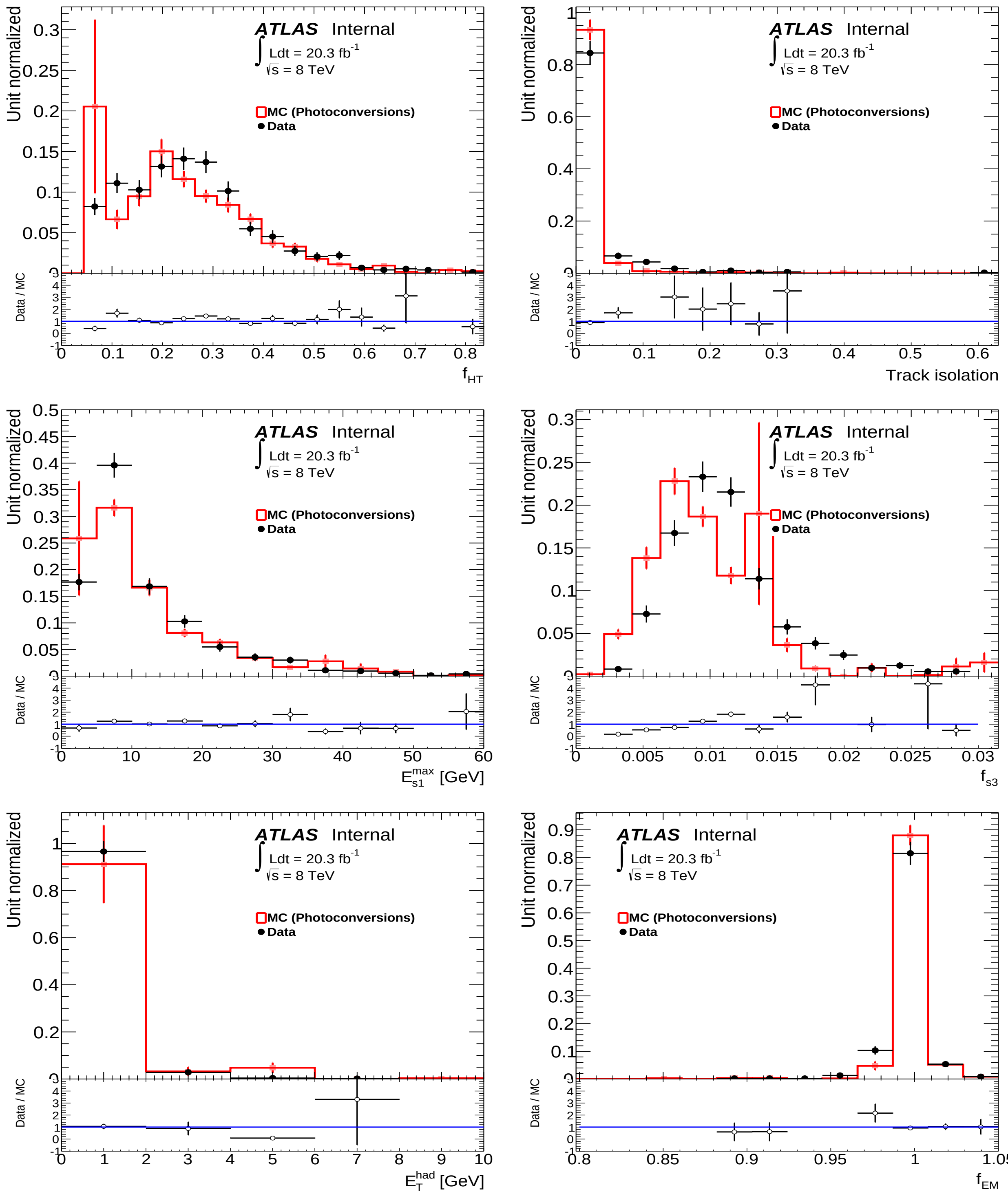

Figure B.4. Distributions of the discriminating variables from photoconversion events show reasonable agreement between the data and MC samples for the eLJ matched to the converted photons. The discrepancies visible in those distributions are due to inadequate statistics in the MC, which includes contributions dominantly from the γ+jets, $\gamma\gamma$ and QCD processes.

APPENDIX C

EFFICIENCY

C.1 Efficiencies of cuts applied to discriminating variables

In this section the cut efficiency of the individual discriminating variables for eLJ, muLJ and emuLJ are shown. Overall cut efficiency for each LJ types are shown in Figure 6.13. The cut efficiencies are shown as a function of dark particle p_{T}.

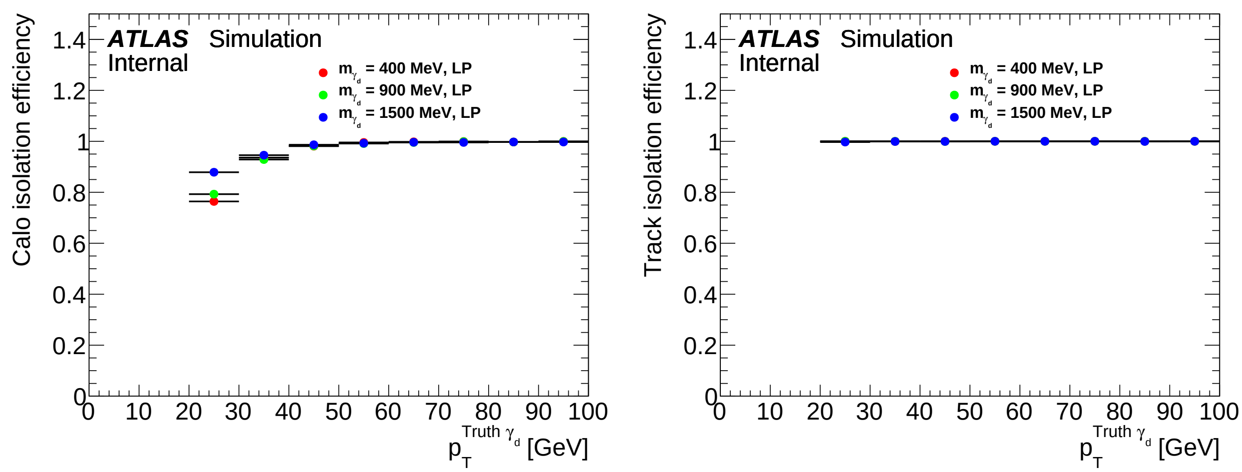

Figure C.1. Cut efficiency of the individual discriminating variables of muLJ. Cut values on the variables are discussed in Section 6.5, Table 6.1

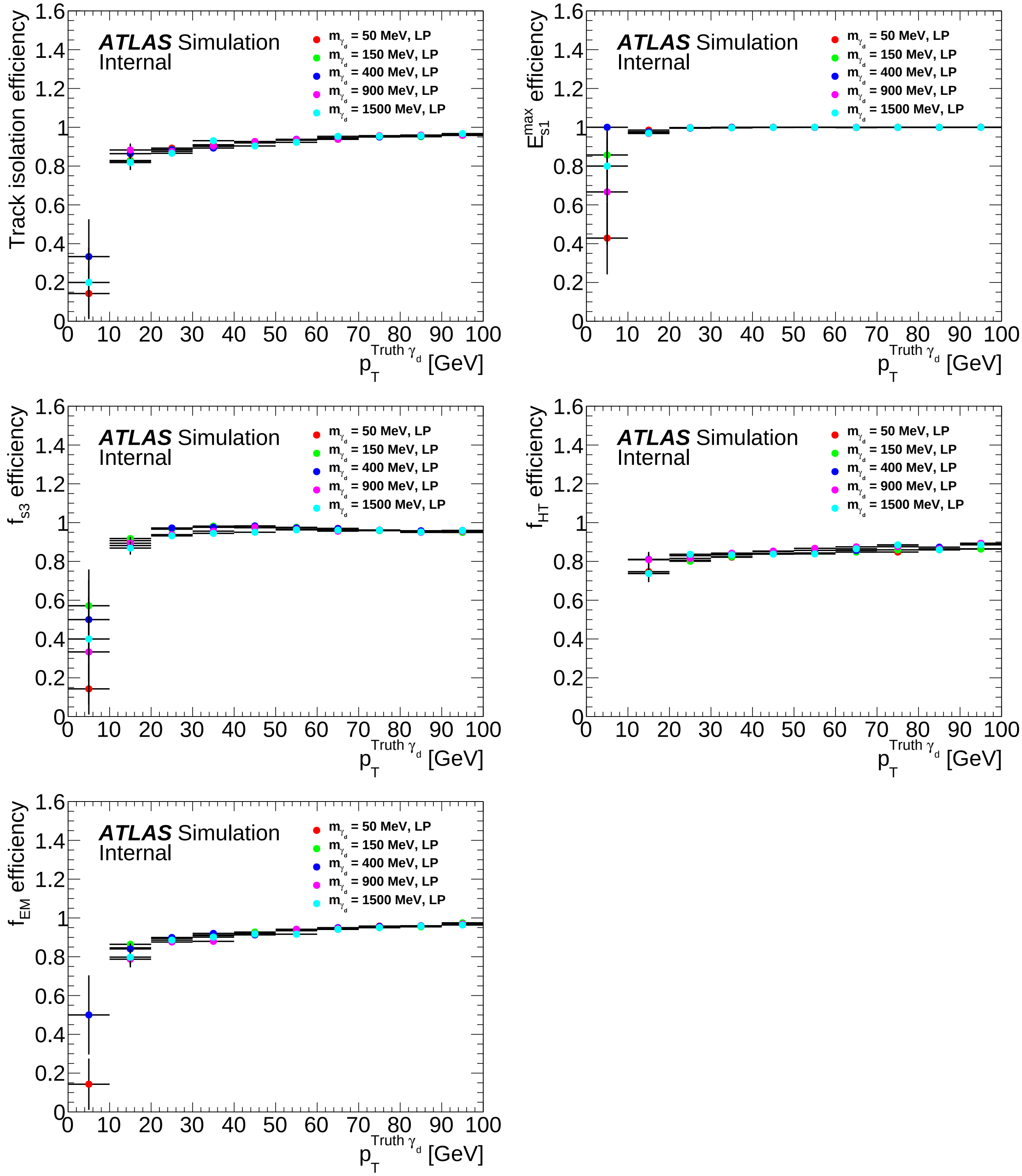

Figure C.2. Cut efficiency of the individual discriminating variables of eLJ. Cut values on the variables are discussed in Section 6.5, Table 6.1

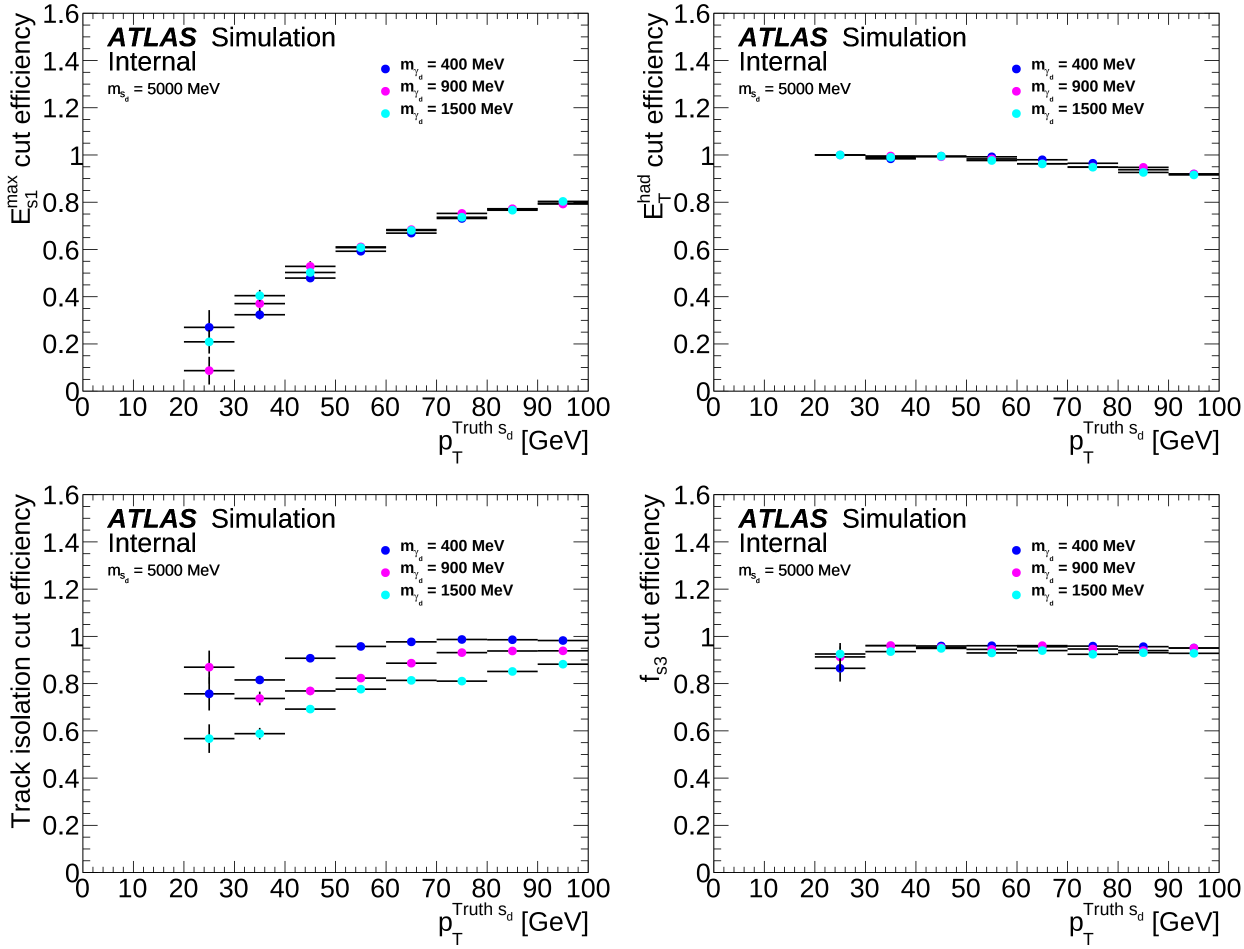

Figure C.3. Cut efficiency of the individual discriminating variables of emuLJ. Cut values on the variables are discussed in Section 6.5, Table 6.1

APPENDIX D

SYSTEMATIC UNCERTAINTIES

D.1 Track reconstruction at small opening angle

In this section, we will discuss the modeling of the ID tracks reconstruction with $p_T \geq 10$ GeV for two collimated leptons. A tag-and-probe method is employed to the $J/\psi \to \mu^+\mu^-$ sample passing EF_2mu6_Jpsimumu trigger requirement to compare the track reconstruction efficiency in the data and MC. Events must contain two muons with $p_T \geq 10$ GeV and $|\eta| \leq 2.5$ matched to the EF_2mu6_Jpsimumu trigger objects, and have invariant mass of those muons within 2 GeV - 4 GeV. One of the two muons, called the tag, must be matched to an ID track with $p_T \geq 10$ GeV passing the requirements as described in Section 6.1. No such requirement is made to the second muon. The invariant mass distribution is fitted with a double Gaussian function for the signal and a second order polynomial for the background to extract the number of J/ψ events under the J/ψ mass peak.

The track efficiency is evaluated by looking at the fraction of the probe muons matched to an ID track. Figures D.2 - D.5 show the invariant mass distributions and the number of J/ψs extracted from the fit to the data. The tracking efficiency is measured both in data and MC, as shown in Figure D.1. The difference between the two efficiency values, based on the straight line fit to the ratio of data and MC efficiencies, is taken as a systematic uncertainty. For the $\Delta R \leq 0.1$ this is found to be 8.4%, while for $\Delta R \geq 0.1$ this is evaluated to be 1.3%. Since typical opening angle between tracks in the lepton-jets from signal MC samples is below 0.1, a 8.4% uncertainty is assigned to the track reconstruction at small opening.

Two sets of invariant mass distributions are fitted using double Gaussian and a second order polynomial to extract the amount of $J/\psi \to \mu^+\mu^-$. In the first set the probe muon satisfies the above mention requirements, while in the second set the probe muon must also have an ID track associated passing the quality cuts as listed in Section 6.1. The track reconstruction efficiency is defined as the ratio of number of $J/\psi \to \mu^+\mu^-$ signal events under the peak as determined from the fit of two sets of invariant mass distributions. Figure D.1 shows the reconstruction efficiency in data and J/ψ MC.

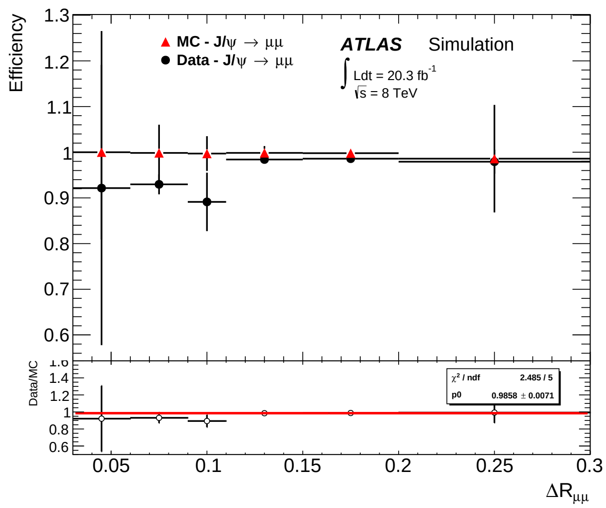

Figure D.1. The track reconstruction efficiency determined using two muons with the tag and probe method as function of ΔR between the muons from data and MC. Bottom section of the plot shows the ratio between data and MC. The systematics uncertainty associated is determined from a straight line fit to the ratio of data and MC efficiencies.

The reconstruction efficiency is computed in 6 regions of ΔR between two muons: 0.03-0.06, 0.06-0.09, 0.09-0.11, 0.11-0.15, 0.15-0.20, 0.20-0.30. Figures D.2 - D.5 show the invariant mass distribution of the tag and probe muons, with all probe muons (left) and with those matched to the ID tracks (right). The blue curve represents the fit to the data with a combination of double gaussian and a second order polynomial. The dotted red line represents the fit to the background.

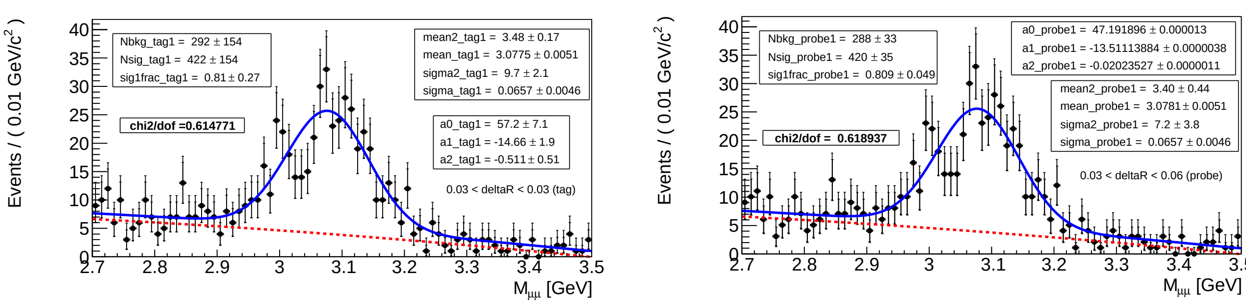

(a) (b)

Figure D.2. Invariant mass distribution of tag and probe muons with all probes (left) and matched probes (right) for the $0.03 < \Delta R < 0.06$ bin.

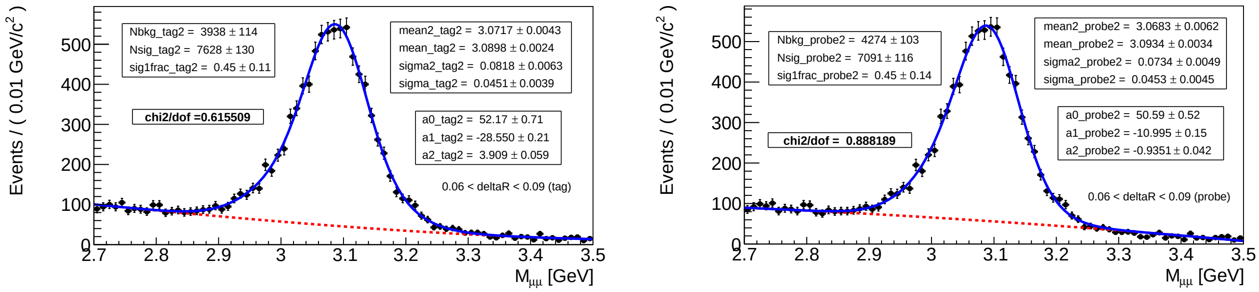

(a) (b)

Figure D.3. Invariant mass distribution of tag and probe muons with all probes (left) and matched probes (right) for the $0.06 < \Delta R < 0.09$ bin.

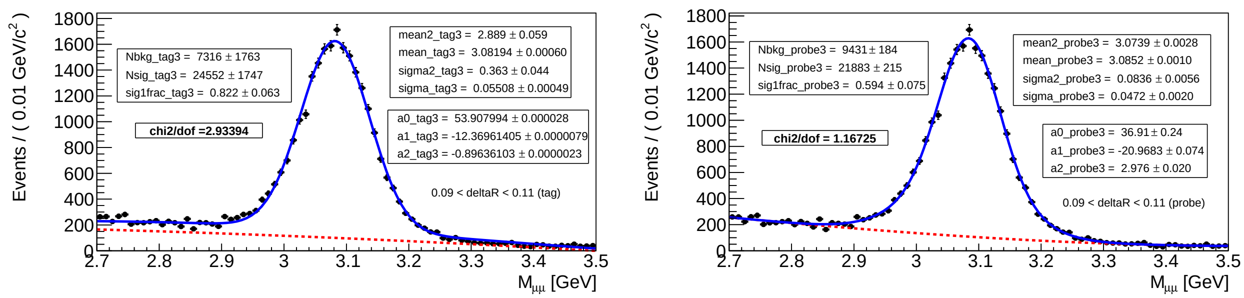

(a) (b)

Figure D.4. Invariant mass distribution of tag and probe muons with all probes (left) and matched probes (right) for the $0.09 < \Delta R < 0.11$ bin.

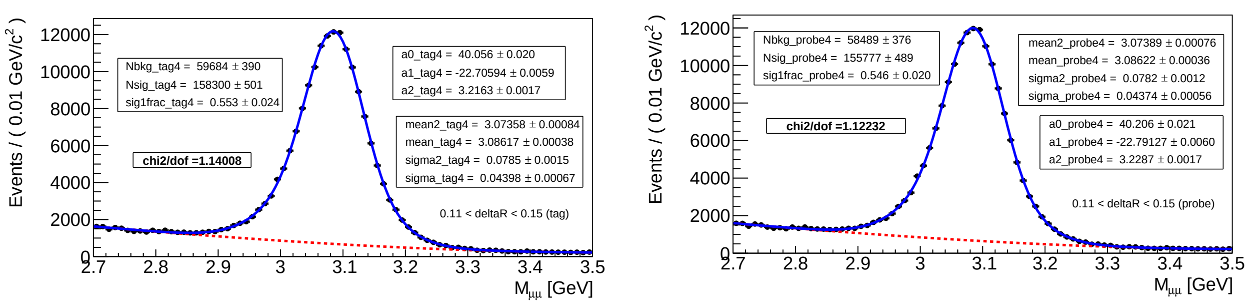

(a) (b)

Figure D.5. Invariant mass distribution of tag and probe muons with all probes (left) and matched probes (right) for the $0.11 < \Delta R < 0.15$ bin.

D.2 Trigger efficiency

Table D.1. The fraction of SUSY generated events with two truth $\gamma_d \to e^+e^-$ that would also pass electron triggers. The OR of both triggers for the event selection maintains good efficiency for a wide range of γ_d masses.

Sample	e60_medium1	g35_loose_g25_loose	e60_medium1 OR g35_loose_g25_loose
m_{γ_d} = 0.1 GeV	0.87	0.75	0.92
m_{γ_d} = 0.2 GeV	0.88	0.75	0.92
m_{γ_d} = 0.3 GeV	0.86	0.74	0.92
m_{γ_d} = 0.4 GeV	0.82	0.75	0.91
m_{γ_d} = 0.5 GeV	0.77	0.75	0.89
m_{γ_d} = 0.7 GeV	0.7	0.71	0.86
m_{γ_d} = 0.9 GeV	0.5	0.61	0.74
m_{γ_d} = 1.2 GeV	0.43	0.58	0.7
m_{γ_d} = 1.5 GeV	0.41	0.57	0.69
m_{γ_d} = 2.0 GeV	0.4	0.61	0.71

Table D.2. The fraction of SUSY generated events with one truth $\gamma_d \to e^+e^-$ and one $\gamma_d \to \mu^+\mu^-$ that would also pass the electron or muon triggers for various γ_d masses. The OR of these triggers is used for eLJ-muLJ, eLJ-emuLJ, muLJ-emuLJ, emuLJ-emuLJ channels.

Sample	e60_medium1	mu36_tight	2mu13	e60_medium1 OR mu36_tight OR 2mu13
m_{γ_d} = 0.3 GeV	0.63	0.49	0.06	0.82
m_{γ_d} = 0.4 GeV	0.58	0.48	0.06	0.79
m_{γ_d} = 0.5 GeV	0.53	0.49	0.06	0.77
m_{γ_d} = 0.7 GeV	0.41	0.50	0.05	0.71
m_{γ_d} = 0.9 GeV	0.29	0.43	0.07	0.62
m_{γ_d} = 1.2 GeV	0.25	0.47	0.08	0.62
m_{γ_d} = 1.5 GeV	0.24	0.51	0.08	0.65
m_{γ_d} = 2.0 GeV	0.22	0.55	0.1	0.67

D.3 Modeling of the eLJ and emuLJ discriminating variables

Samples of Z decays to electron or muon pairs selected from data and MC are used to study the modeling of variables used to select lepton-jets. Using the J/ψ decays to electron or muon pairs was not a feasible option. In case of $J/\psi \rightarrow e^+e^-$ reconstruction using ID tracks with minimum p_T of 10 GeV, small opening angle $\Delta R \leq 0.1$, and having a matched overlapped EM cluster from two electrons renders overwhelmingly large QCD background. The tag-and-probe method is used for this study. The $Z \rightarrow e^+e^-$ samples are selected from both the data and MC by requiring that the events must pass the e60_medium1 trigger, have at least two 'medium' quality electrons satisfying EM cluster criteria given in Section 6.1. Figure D.6 shows the comparison between the data and MC for the invariant mass distribution of two electrons. Events under the peak within the [70-110] GeV mass window are chosen to study the shapes of variables and the efficiency of cuts applied to those variables.

The electron that is matched to the online object that fired the trigger within $\Delta R < 0.2$ is the 'tag' electron, and the other electron is the 'probe'. The probe is matched to an eLJ. After comparing the shapes of all discriminating variables (f_{HT}, track isolation, E_{s1}^{max}, E_T^{had}, f_{s3}, and f_{EM}) between data and MC for the eLJ matched to the probe electron, there is a good agreement in those variables except f_{s3}. The shift in the f_{s3} distribution is found in the MC regardless of the barrel or the end-cap regions of the detector, as shown in Figure D.7. It is due to the imperfect description of crosstalk between the second and third samplings of the EM calorimeter in the MC simulation. Before evaluating the systematic uncertainty on the discriminating variables, a correction to the MC is applied using the ratio between data and MC obtained from Figure D.7 as event weight. After correction, there is a better agreement between data and MC as illustrated in Figure D.9.

The cut efficiency for each variable (f_{HT}, track isolation, E_{s1}^{max}, f_{s3}, and f_{EM}) as function of the cluster E_T and η in the data and MC from $Z \rightarrow e^+e^-$ events is used to assess the size of systematic uncertainty associated with a possible mismodeling of the optimized discriminating variables. The efficiency of cut on a variable is defined as the fraction of those eLJs matched to the probe satisfying the cuts on the variables. The cut values for all variables (f_{HT}, track isolation, E_{s1}^{max}, f_{s3}, and f_{EM}) are described in Table 6.1. The cut efficiency for each variable shown in Figures D.13 and D.14. The systematic uncertainty is assigned based on a straight line fit to the data to MC efficiency ratio. An additional 4.5% systematic uncertainty is assigned for the track isolation dependence on the pile-up, as illustrated Figure D.15. This systematic uncertainty is evaluated based on the efficiency difference at the highest average interactions per bunch crossing and at the lowest average interactions per bunch crossings.

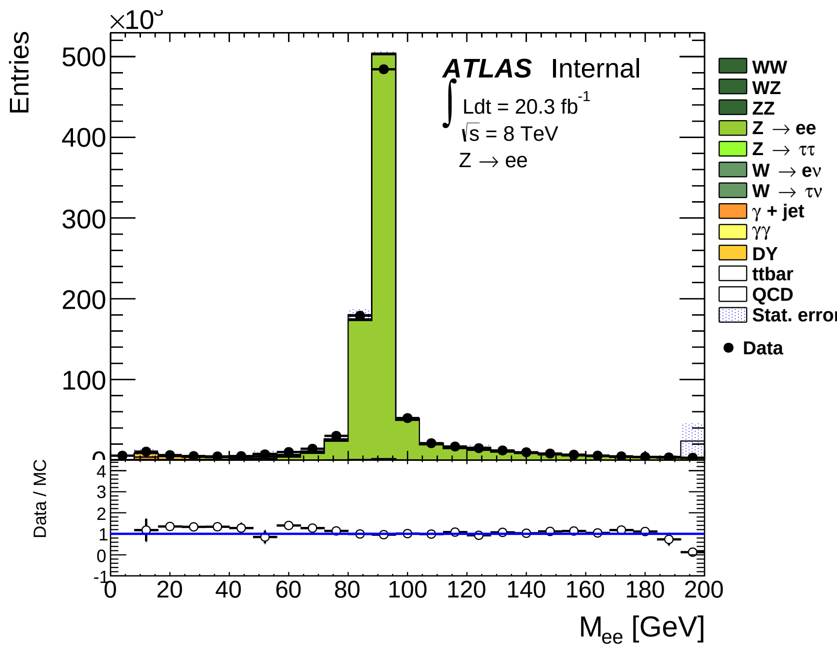

Figure D.6. Distribution of the invariant mass of two electrons showing that the data agrees reasonably well with the MC expectations under the Z peak. Events within the [70-110] GeV mass window are used to study the lepton-jets discriminating variables to compare their modeling in the MC to the data. The contributions from QCD shown in this figure have large fluctuation due to limited statistics in the MC.

Systematic uncertainty for the f_{s3} variable is derived using the scale factors obtained from ratio of the f_{s3} efficiency distribution between data and MC. After investigating the ratio of f_{s3} distributions in the data and MC for various cluster E_T regions as shown in Figure D.10, The ratios are statistically consistent for cluster $E_T < 30$ GeV and cluster $E_T \geq 30$ GeV cases. Therefore the scale factor (ratio between the f_{s3} cut efficiency in data and MC]) is derived for cluster $E_T < 30$ GeV and $E_T > 30$ GeV in different η regions (Figure D.11). Additionally a 3% systematic uncertainty is assigned to those scale factors due to small background contributions. The statistical and systematic uncertainties of the scale factors are treated as the systematic uncertainty associated with the corrected efficiencies of cuts applied to eLJ variables in the signal MC samples. The f_{s3} variable, that is found to be shifted in data, is compared between $Z \rightarrow e^+e^-$ MC and LJ gun (signal) MC samples for various cluster E_T regions to assure the applicability of those scale factors derived from $Z \rightarrow e^+e^-$ MC to the signal MC. Figure D.16 shows that, in a given cluster E_T region, the shape of distributions are consistent in the LJ gun MC events and the $Z \rightarrow e^+e^-$ events.

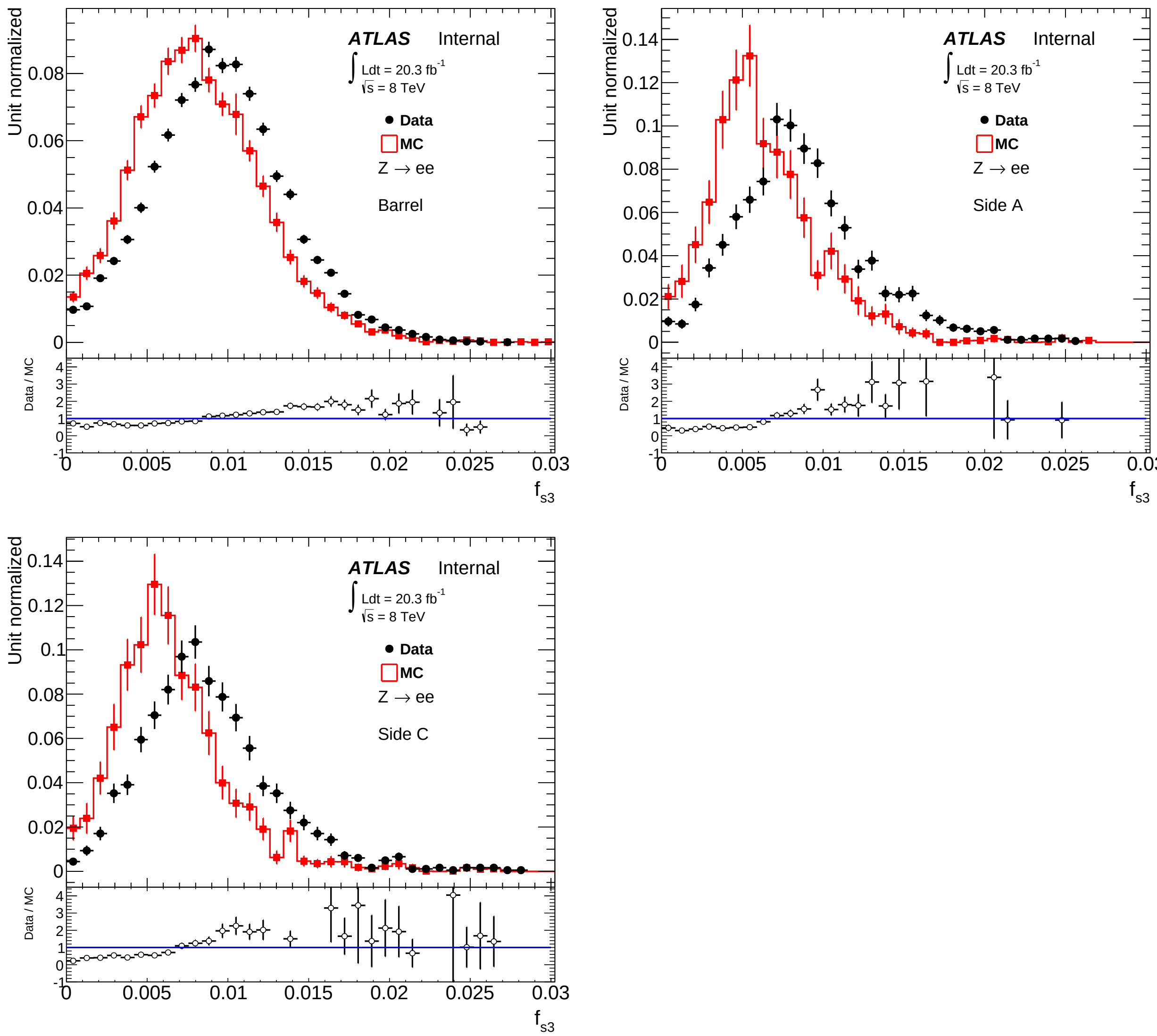

Figure D.7. The shape of f_{s3} variables from the $Z \to e^+e^-$ dominated events shows that the data has harder f_{s3} spectrum compared to the MC in the barrel, end-cap A and end-cap C regions of the detector, as shown in the left, middle and right figures respectively.

The efficiencies of each cut applied to the eLJ variables using the $Z \to e^+e^-$ events are studied as a function of cluster E_T, η and the mean number of interactions per bunch crossings, i.e $< \mu >$, as shown in Figure D.13, Figure D.14 and Figure D.15, respectively.

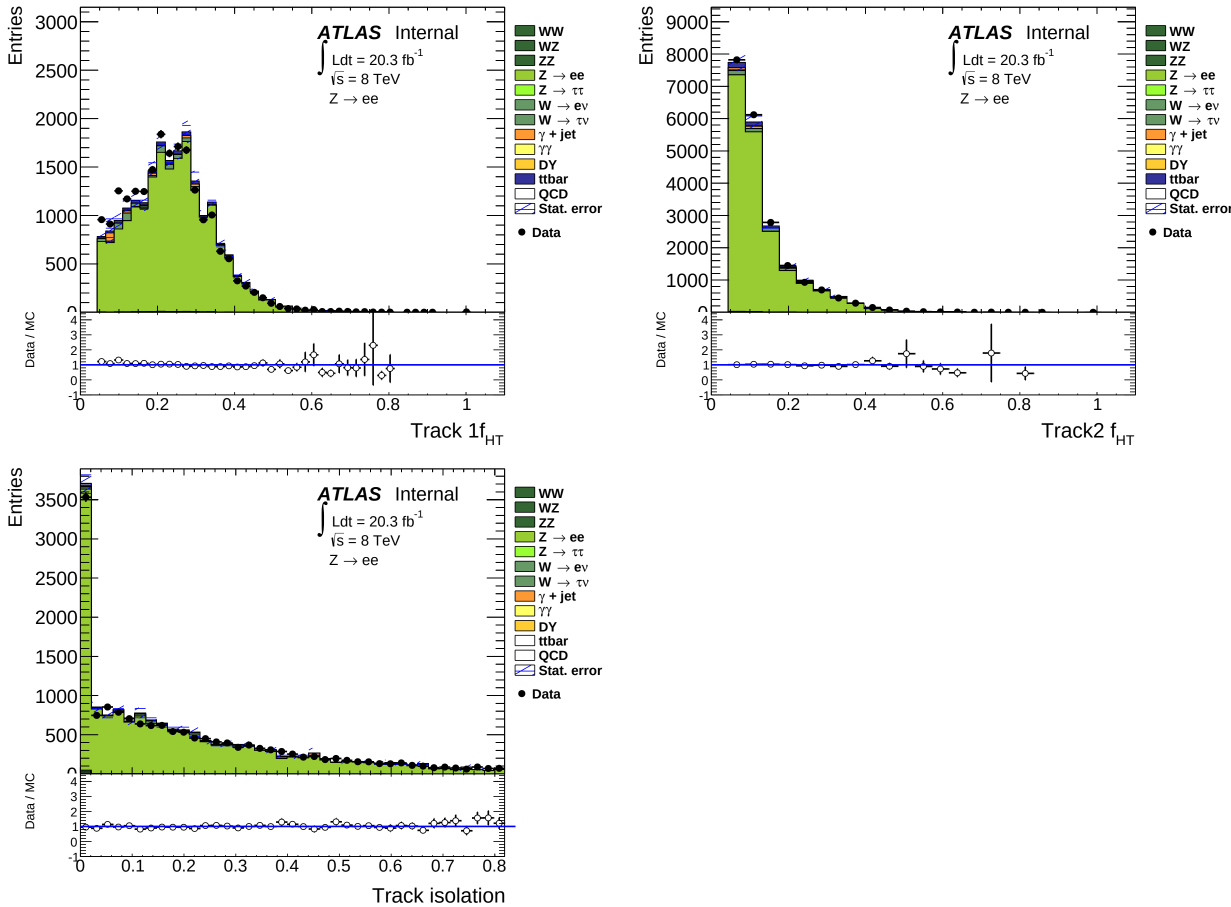

Figure D.8. Distributions of the ID track based discriminating variables from $Z \to e^+e^-$ dominated events show reasonably good agreement between data and MC samples for the eLJ matched to the probe electron.

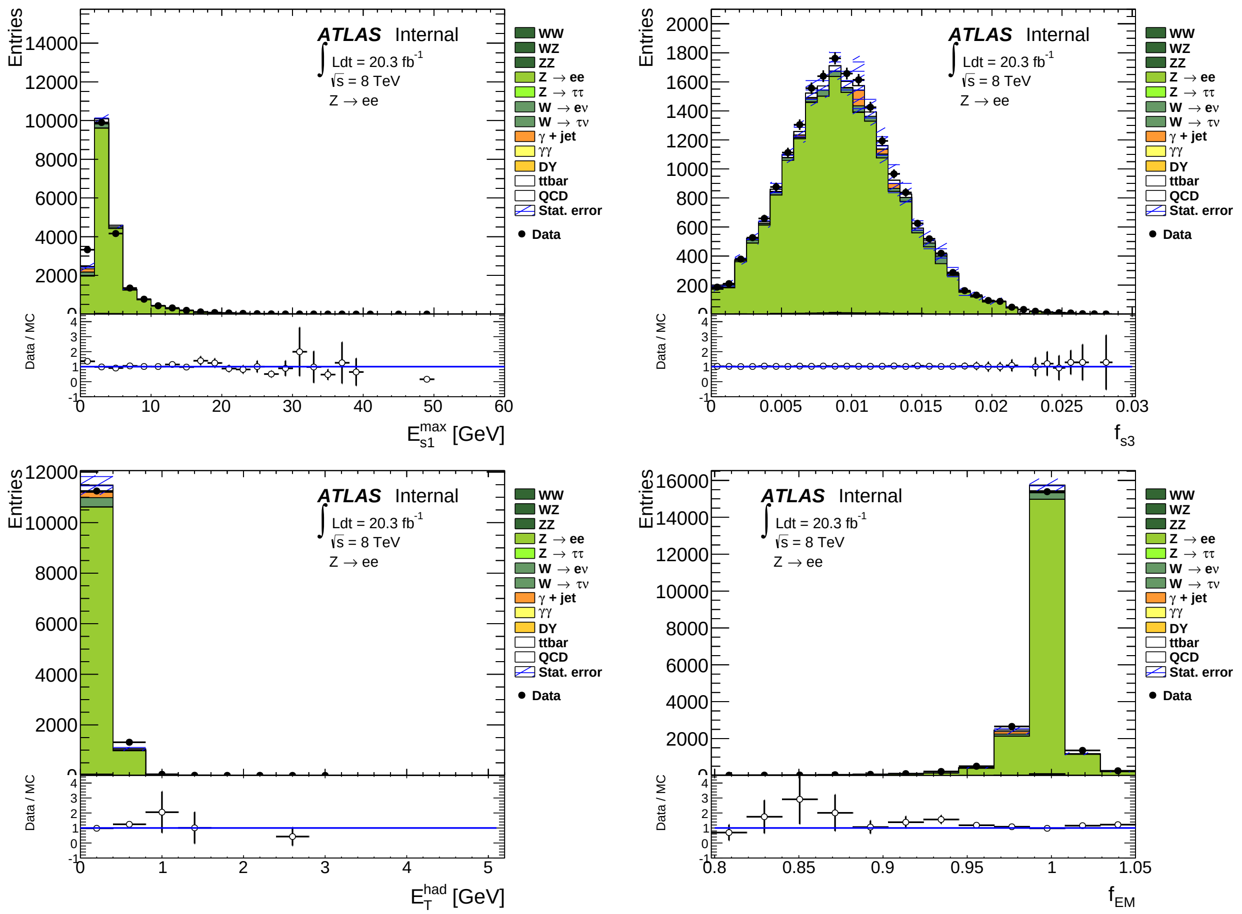

Figure D.9. Distributions of the cluster based discriminating variables from $Z \to e^+e^-$ dominated events show reasonably good agreement between the data and MC samples for the eLJ matched to the probe electron.

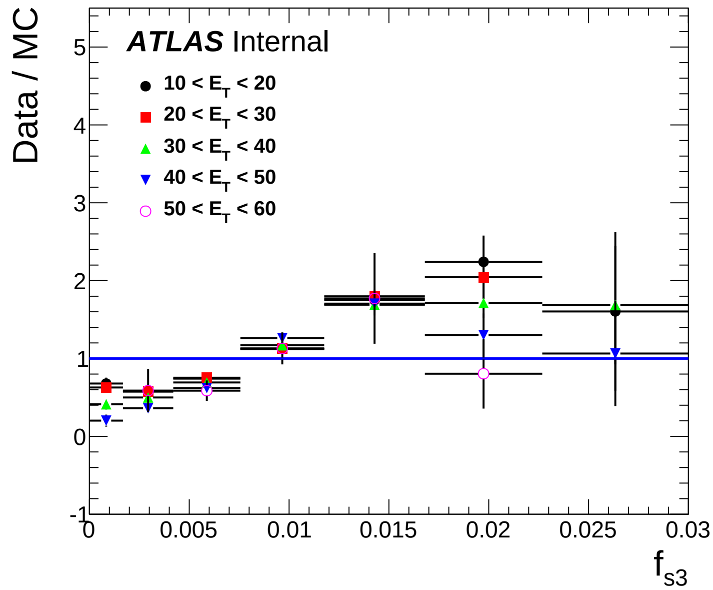

Figure D.10. Ratio of the f_{s3} distribution between Data and MC for various cluster E_T ranges.

Table D.3. The scale factors of f_{s3} cut efficiencies with respect to events already passing the cuts on the other discriminating variables. All quoted errors are statistical only. Due to small background present in the $Z \to e^+e^-$ sample, additional 3% systematic uncertainty is assigned for these scale factors.

Cluster $\|\eta\|$ regions	Data/MC scale factors for eLJ		Data/MC scale factors for emuLJ	
	Cluster $E_T < 30$ GeV	Cluster $E_T \geq 30$ GeV	Cluster $E_T < 30$ GeV	Cluster $E_T \geq 30$ GeV
$[0.0, 0.6]$	0.91 ± 0.04	0.91 ± 0.06	0.97 ± 0.01	0.97 ± 0.02
$[0.6, 1.2]$	1.01 ± 0.01	0.98 ± 0.03	0.99 ± 0.01	0.98 ± 0.01
$[1.2, 1.8]$	0.98 ± 0.03	0.90 ± 0.05	1.01 ± 0.02	0.93 ± 0.02
$[1.8, 2.4]$	1.00 ± 0.03	0.91 ± 0.05	0.94 ± 0.02	0.90 ± 0.03

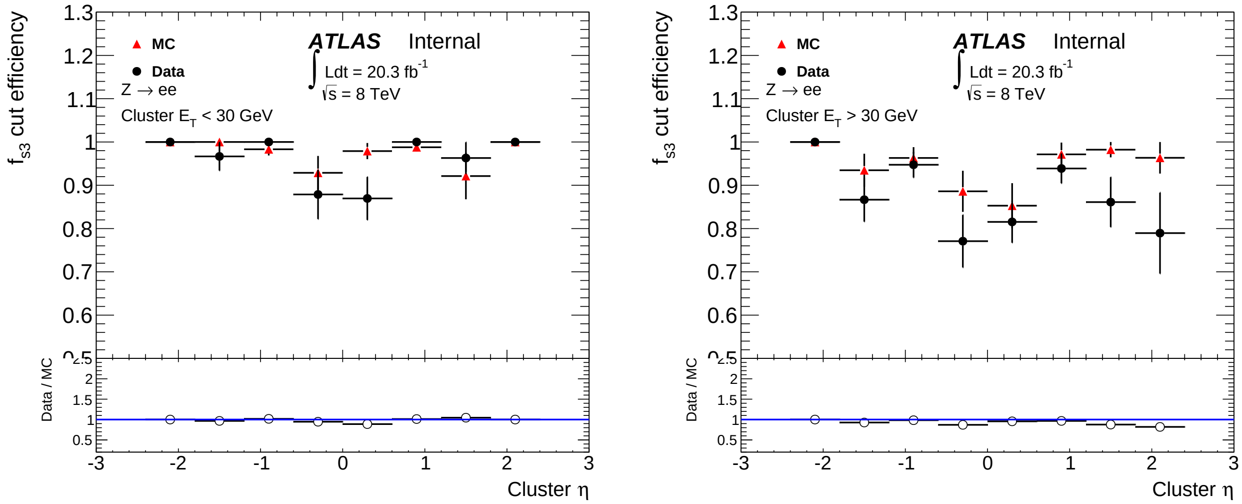

(a) (b)

Figure D.11. The efficiency of a reconstructed eLJ matched to the probe electron to pass the f_{s3} cut that has already satisfied the cuts on other discriminating variables (E_{s1}^{max}, Track isolation, f_{HT}, and f_{EM}) in data and MC samples containing $Z \to ee$ events. The efficiencies are shown as a function of cluster η. Left, cluster E_T below 30 GeV. Right, cluster E_T above 30 GeV.

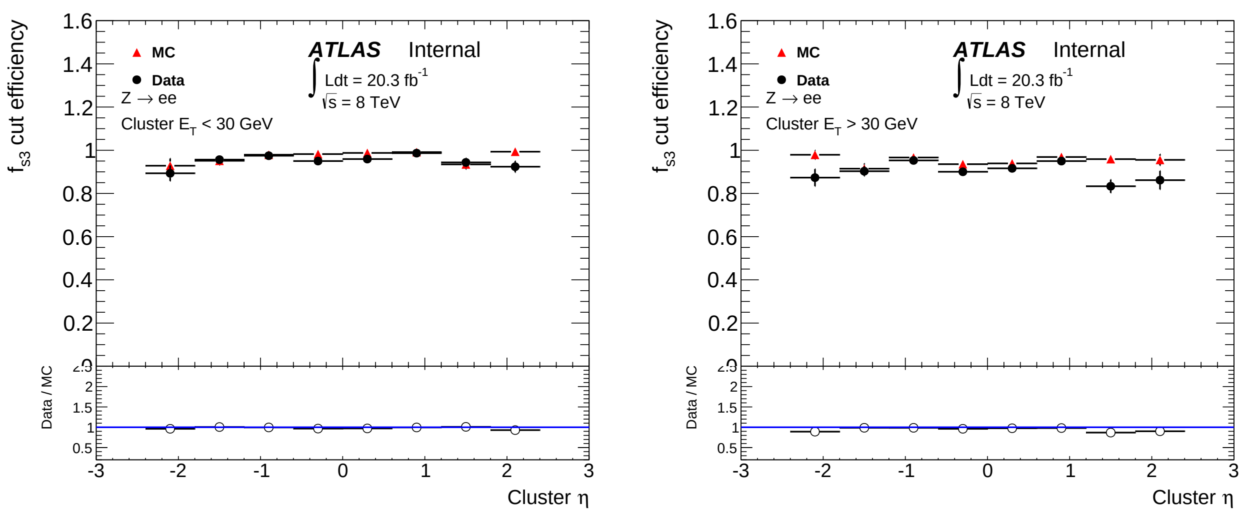

(a) (b)

Figure D.12. The efficiency of a reconstructed eLJ matched to the probe electron to pass the f_{s3} cut that has already satisfied the cuts on other discriminating variables (E_{s1}^{max}, Track isolation, and E_T^{had}) in data and MC samples containing $Z \to ee$ events. Left, for cluster E_T below 30 GeV. Right, for cluster E_T above 30 GeV.

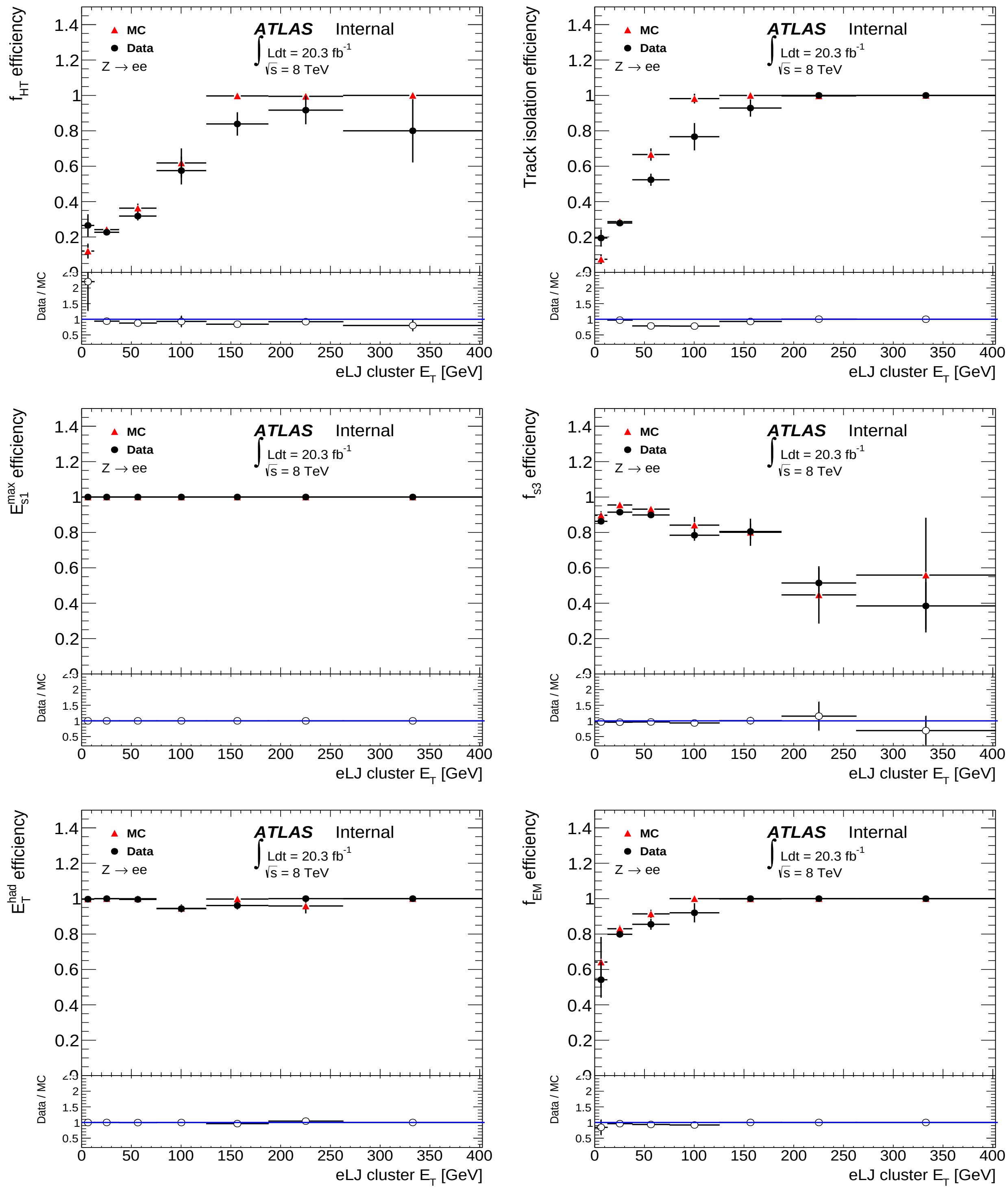

Figure D.13. Efficiencies of the cuts on the discriminating variables as a function of cluster E_T from $Z \to e^+e^-$ events show reasonable agreement between the data an d MC samples for the eLJ matched to the probe.

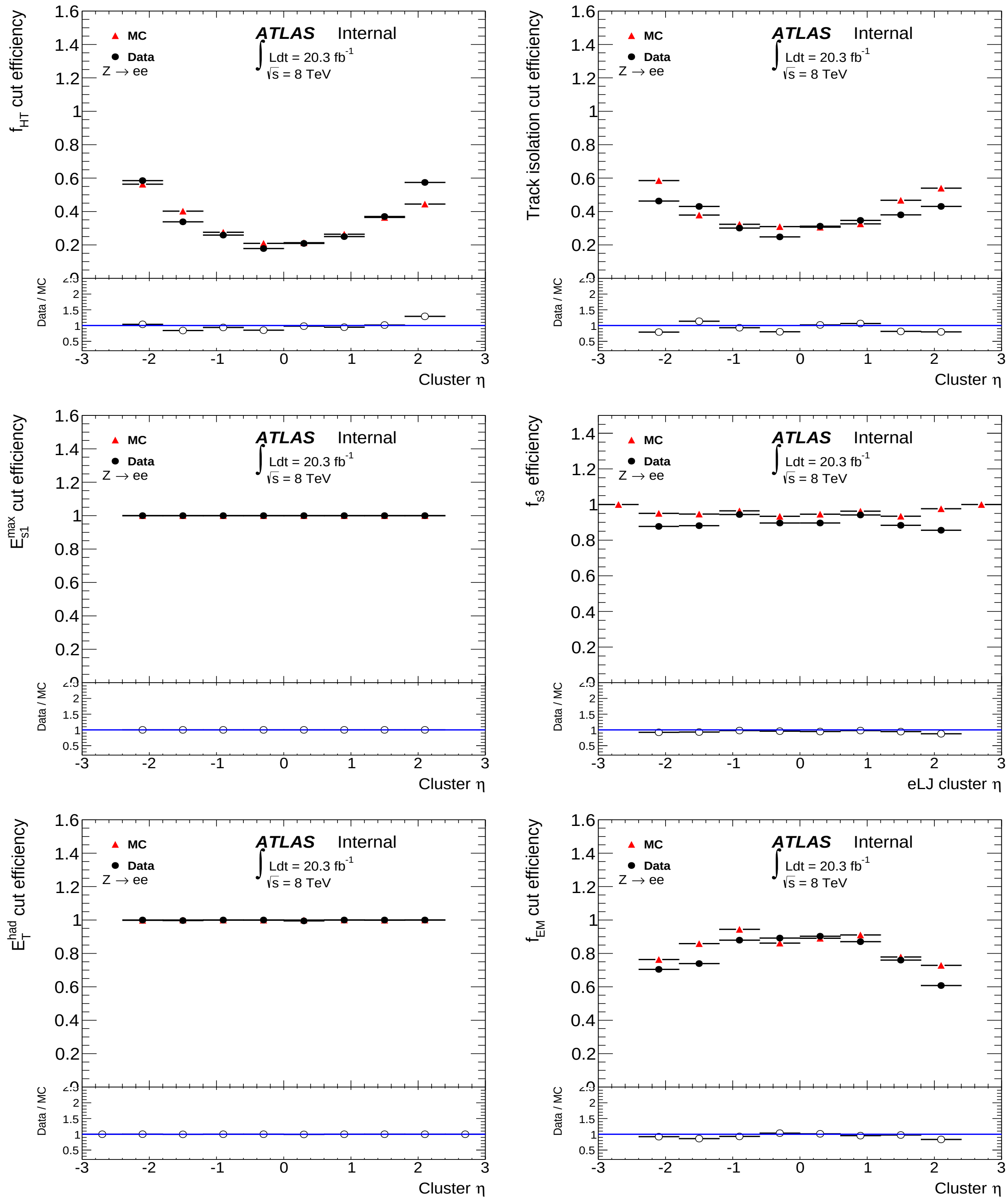

Figure D.14. Efficiencies of the cuts on the discriminating variables as a function of cluster η from $Z \to e^+e^-$ events show reasonable agreement between the data and MC samples for the eLJ matched to the probe.

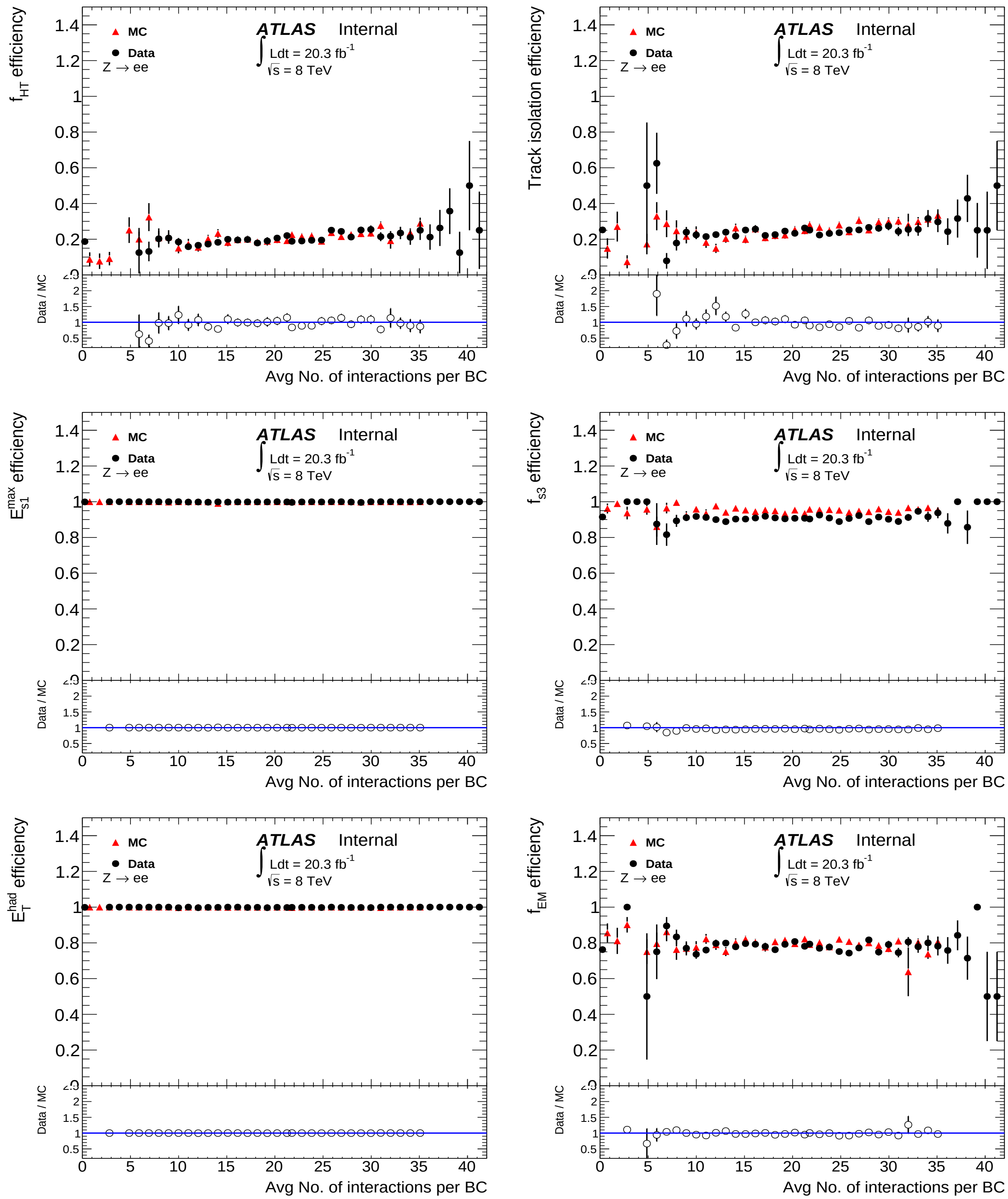

Figure D.15. Efficiencies of the cuts on the discriminating variables as a function of average number of interactions per bunch crossings from $Z \to e^+e^-$ events show reasonable agreement between the data and MC samples for the eLJ matched to the probe.

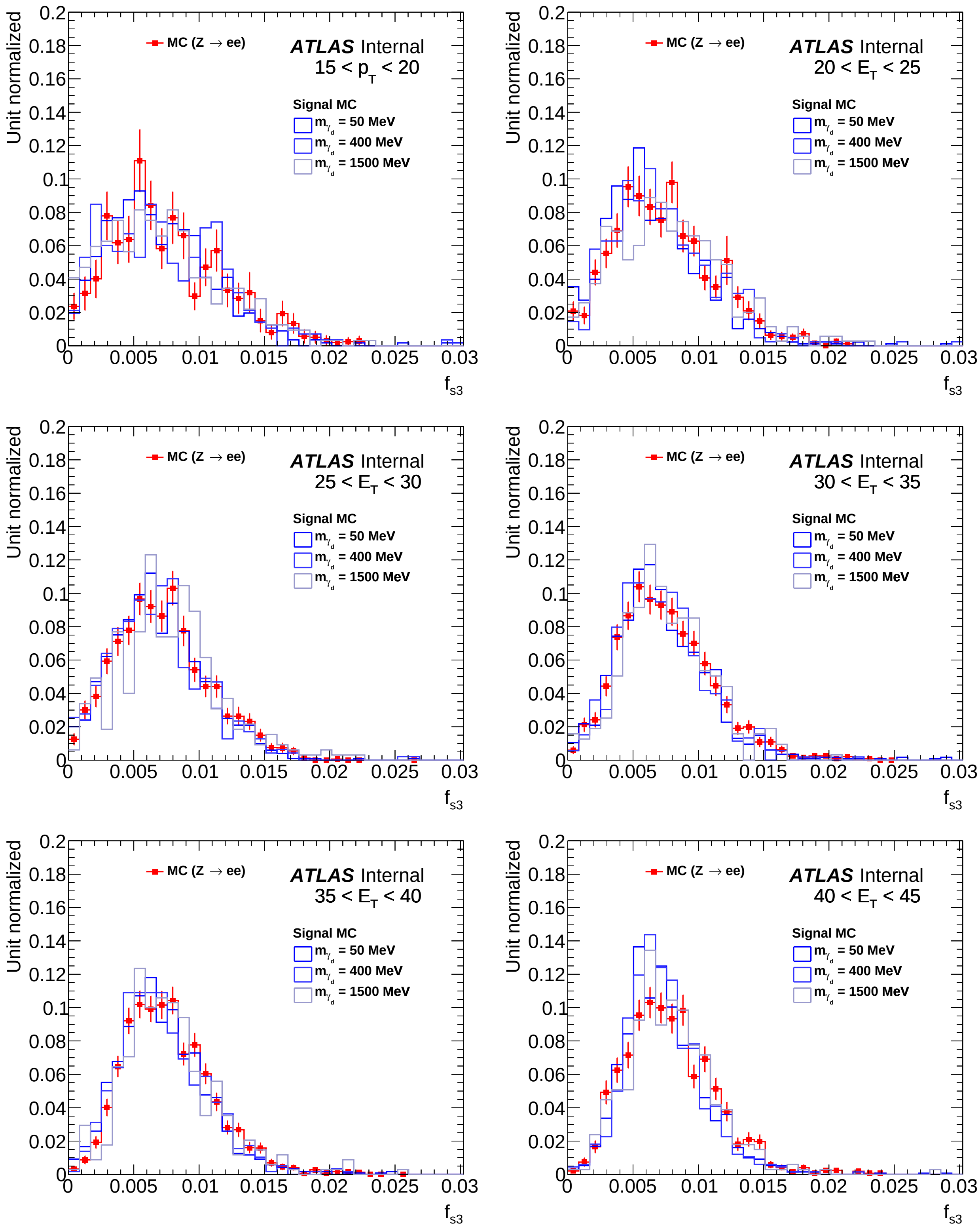

Figure D.16. f_{s3} distribution of signal MC from LJgun (blue) and background (red) MC ($Z \to ee$ control sample) in different EM cluster E_T bins.

D.4 Modeling of the muLJ discriminating variables

The systematic uncertainty associated with the muLJ discriminating variables are studied using $J/\psi \to \mu^+\mu^-$ sample. The sample selection is same as described in Appendix D.1. The probe muon is matched to the muLJ. The fraction of probe matched muLJ that pass the track isolation cut is the numerator in the efficiency plot in Figure D.17a. The fraction of probe matched muLJ that pass the calorimeter isolation cut is the numerator in the efficiency plot in Figure D.17b.

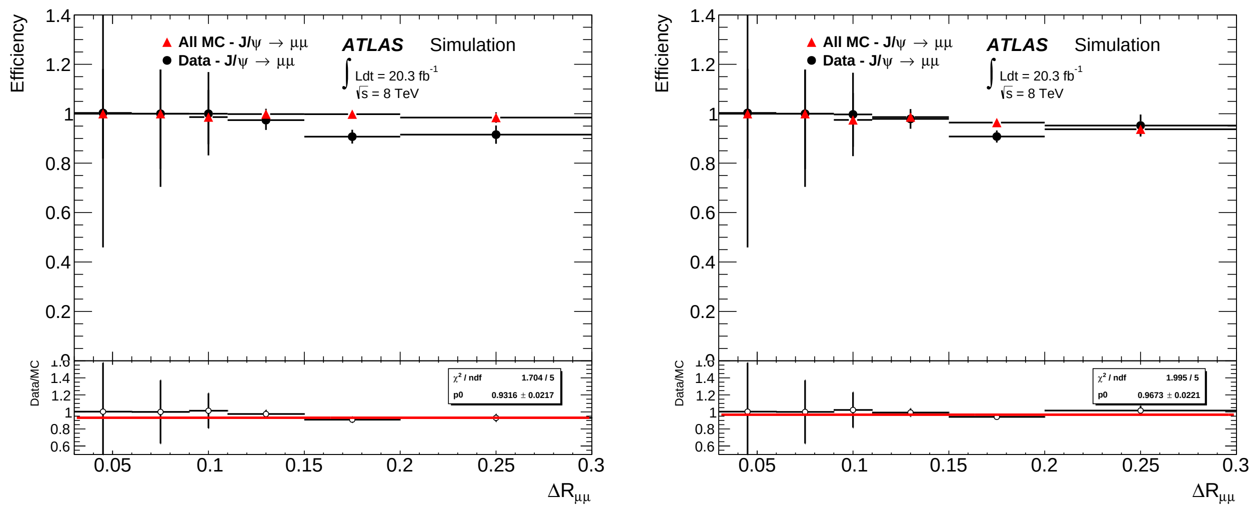

(a) (b)

Figure D.17. Cut efficiency of (a) track isolation and (b) calorimeter isolation in muLJ using $J/\psi \to \mu\mu$ sample based on tag and probe method. The straightline fit to the data and MC ratio in efficiencies is taken as systematics uncertainty for each variable.

D.5 Modeling of standard 'loose' or 'medium' electron cluster definitions

The g35_loose_g25_loose and e60_medium1 triggers apply the ATLAS standard 'loose' and 'medium' requirements which are based on a combination of discriminants depending on the cluster E_T and η regions. Those triggers are found to be well modeled for isolated electrons (from ATLAS internal note). However, it is important to check their modeling for collimated electrons. Events containing at least one eLJ in the data and background MC are used to study the efficiency of the eLJ to have a 'loose' or 'medium' quality electron cluster as a function of opening angle between two leading tracks of eLJ. Each eLJ must have both tracks with a minimum p_T of 10 GeV, and have passed $f_{HT} > 0.05$ requirement to suppress the background from pions. The number of those eLJs that would further pass the 'medium' quality electron requirement is extracted. Figure D.18 shows the fraction of these eLJs satisfying the 'medium' quality electron requirement as a function of ΔR between the two tracks, where the denominator is the number of eLJs that have both tracks with $p_T \geq 10$ GeV, and $f_{HT} > 0.05$ and the numerator is the number of those eLJs which also have 'medium' quality electron.

A straight line fit to the data over MC ratio of the efficiency is used to extract the uncertainty associated with the 'medium' or 'loose' quality efficiency as shown in Figure D.18. The difference is taken as the systematic uncertainty for the cluster quality requirements in both triggers. All bins in data agrees within 2σ of the MC. Given that p_{med} is a probability of an eLJ to have a 'medium' quality offline cluster, the total probability a_{med} of an event containing two eLJs to have either of eLJs to have a 'medium' cluster is $2p_{med}(1 - p_{med}) + p_{med} \times p_{med}$. Similarly, the total probability a_{lo} of an event containing two eLJs to have both eLJs matched to a 1loose' cluster is $p_{lo} \times p_{lo}$, where p_{lo} is the probability of an eLJ to have a 'loose' quality cluster matched.

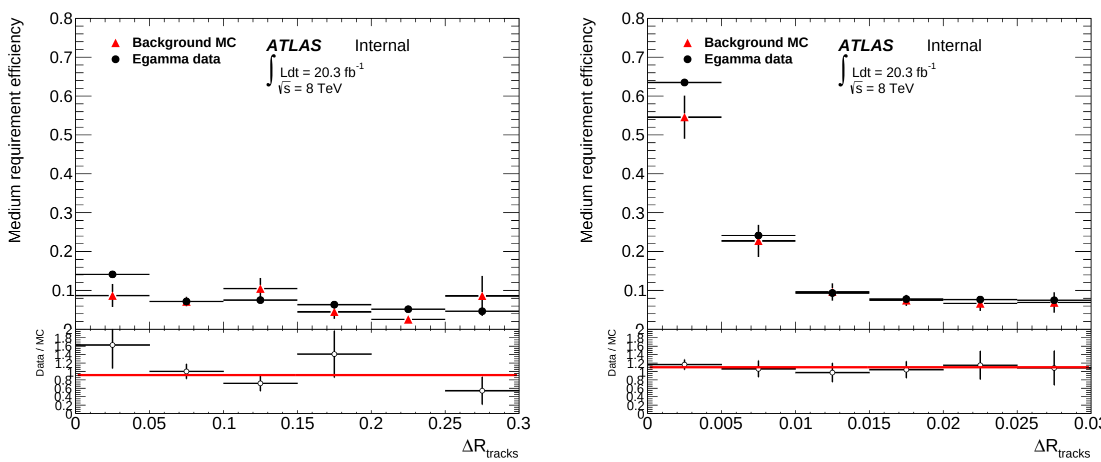

Figure D.18. The figure on the left (right) shows the fraction of eLJs having 'medium' quality electron cluster as a function of ΔR between the tracks in the ΔR range of 0.3 (0.03) in data and MC.

Table D.4. This table shows the probability of matching a 'medium' quality cluster to an eLJ (p_{med}), the probability of matching a 'loose' quality cluster to an eLJ (p_{lo}), the event acceptance with at least one eLJ matched to a 'medium' cluster (a_{med}), and the event acceptance with at least two eLJ matched to 'loose' cluster each (a_{lo}). The last column shows the weighted average systematics uncertainty associated with the OR of the triggers used in the electron channel, where weights are based on the fraction of signal MC events to pass each of triggers as listed in Table D.1.

Samples (SUSY portal)	p_{med}	p_{lo}	a_{med}	a_{lo}	weighted average uncert.
$m_{\gamma_d} = 0.1$ GeV	0.98	0.99	0.89	0.9	8.6%
$m_{\gamma_d} = 0.3$ GeV	0.84	0.85	0.76	0.77	9.6%
$m_{\gamma_d} = 0.5$ GeV	0.65	0.67	0.6	0.61	11.0%
$m_{\gamma_d} = 0.7$ GeV	0.50	0.52	0.45	0.47	11.8%
$m_{\gamma_d} = 0.9$ GeV	0.41	0.43	0.38	0.39	12.5%
$m_{\gamma_d} = 1.2$ GeV	0.29	0.3	0.27	0.28	13.1%
$m_{\gamma_d} = 1.5$ GeV	0.29	0.31	0.26	0.28	13.2%
$m_{\gamma_d} = 2.0$ GeV	0.24	0.26	0.22	0.24	13.5%

Table D.5. This table lists the systematics uncertainties associated with each of the e60_medium1, mu36_tight and 2mu13 involved in the mixed channel selection. In the mixed channels (eLJ-muLJ, muLJ-emuLJ combinations) the event probability for one lepton-jet having EM cluster to pass the trigger's medium requirement is $a_{med} = p_{med}$, and the uncertainty of a_{med} is 9%. In other mixed channels (eLJ-emuLJ, emuLJ-emuLJ combinations) the event probability for at least one lepton-jet having EM cluster to pass the trigger's medium requirement is $a_{med} = 2p_{med}(1 - p_{med}) + p_{med}p_{med}$, and the uncertainty of a_{med} is 8%. The fraction of events that pass those individual triggers is listed in Table D.2 for each γ_d mass point. The last column shows the weighted average systematics uncertainty associated with the OR of those triggers used in the mixed channel.

Samples (SUSY portal)	e60_medium1 uncertainty	mu36_tight uncertainty	2mu13 uncertainty	weighted average uncert.
$m_{\gamma_d} = 0.3$ GeV	9.0%	0.6%	5.8%	5.4%
$m_{\gamma_d} = 0.5$ GeV	9.0%	0.6%	5.8%	5.0%
$m_{\gamma_d} = 0.7$ GeV	9.0%	0.6%	5.8%	4.5%
$m_{\gamma_d} = 0.9$ GeV	9.0%	0.6%	5.8%	4.1%
$m_{\gamma_d} = 1.2$ GeV	9.0%	0.6%	5.8%	3.8%
$m_{\gamma_d} = 1.5$ GeV	9.0%	0.6%	5.8%	3.5%
$m_{\gamma_d} = 2.0$ GeV	9.0%	0.6%	5.8%	3.3%

APPENDIX E

TABLES FOR 95% CL UPPER LIMITS ON SIGNAL EXPECTATIONS

eLJ-eLJ

Table E.1. This table shows the 95% CL upper limit on the number of expected and observed events for various signal benchmarks in the eLJ–eLJ channel.

Signal benckmarks	$2\gamma_d$ + X						$2(s_d \to \gamma_d\gamma_d)$ + X					
γ_d mass [GeV]	Obs.	Exp.	-2σ	-1σ	$+1\sigma$	$+2\sigma$	Obs.	Exp.	-2σ	-1σ	$+1\sigma$	$+2\sigma$
SUSY												
0.1	8.4	6.6	3.0	4.3	10.9	18.1	8.3	6.5	2.9	4.2	10.7	17.9
0.2	8.4	6.6	3.0	4.3	10.9	18.1	8.3	6.5	2.9	4.2	10.7	17.9
0.3	8.4	6.6	3.0	4.3	10.9	18.2	8.4	6.6	3.0	4.3	10.8	18.1
0.4	8.4	6.6	3.0	4.3	10.9	18.3	9.0	7.1	3.2	4.6	11.7	19.5
0.5	8.4	6.6	3.0	4.3	11.0	18.4	9.2	7.2	3.3	4.7	12.0	20.1
0.7	8.5	6.7	3.0	4.3	11.0	18.6	9.3	7.3	3.3	4.7	12.1	20.4
0.9	8.5	6.7	3.0	4.3	11.0	18.7	9.9	7.8	3.6	5.0	13.0	21.9
1.2	8.6	6.7	3.0	4.3	11.2	18.9	9.3	7.3	3.3	4.7	12.1	20.5
1.5	8.6	6.7	3.0	4.3	11.2	18.9	9.1	7.2	3.2	4.7	12.0	20.2
2	8.5	6.7	3.0	4.3	11.1	18.8	9.1	7.2	3.2	4.7	12.0	20.3
Higgs												
0.4	8.5	6.7	3.0	4.3	10.9	18.3	8.5	6.7	3.0	4.3	11.0	18.3

muLJ-muLJ

Table E.2. This table shows the 95% CL upper limit on the number of expected and observed events for various signal benchmarks in the muLJ–muLJ channel.

Signal benckmarks	$2\gamma_d$ + X						$2(s_d \to \gamma_d\gamma_d)$ + X					
γ_d mass [GeV]	Obs.	Exp.	-2σ	-1σ	$+1\sigma$	$+2\sigma$	Obs.	Exp.	-2σ	-1σ	$+1\sigma$	$+2\sigma$
SUSY												
0.3	5.9	6.5	2.9	4.1	10.9	18.7	6.3	6.9	3	4.4	11.6	19.9
0.4	5.9	6.5	2.9	4.1	10.9	18.7	6.3	6.9	3	4.4	11.6	19.8
0.5	5.9	6.5	2.9	4.1	10.9	18.7	6.4	6.9	3	4.4	11.7	19.9
0.7	6	6.6	2.9	4.1	11	19	7	7.6	3.4	4.9	12.8	21.9
0.9	5.9	6.5	2.9	4.1	10.9	18.7	6.7	7.3	3.3	4.7	12.3	21
1.2	5.9	6.5	2.9	4.1	10.9	18.7	6.8	7.4	3.3	4.7	12.5	21.3
1.5	5.9	6.5	2.9	4.1	10.9	18.7	7.1	7.8	3.5	4.9	13	22.1
2	5.9	6.5	2.9	4.1	10.9	18.7	7.6	8.3	3.8	5.3	13.8	23.3
Higgs												
0.4	5.9	6.5	2.9	4.1	11	18.8	6.5	7	3.1	4.5	11.9	20.3

eLJ-muLJ

Table E.3. This table shows the 95% CL upper limit on the number of expected and observed events for various signal benchmarks in the eLJ–muLJ channel.

Signal benckmarks	$2\gamma_d$ + X						$2(s_d \to \gamma_d\gamma_d)$ + X					
γ_d mass [GeV]	Obs.	Exp.	-2σ	-1σ	$+1\sigma$	$+2\sigma$	Obs.	Exp.	-2σ	-1σ	$+1\sigma$	$+2\sigma$
SUSY												
0.3	3.9	8	3.8	5.3	12.9	21	4.1	8.6	4	5.7	13.8	22.3
0.4	3.9	8	3.8	5.3	12.9	20.9	4.1	8.6	4	5.7	13.8	22.4
0.5	3.9	8	3.8	5.3	12.9	20.9	4.3	8.8	4.1	5.8	14.1	22.8
0.7	3.9	8.2	3.8	5.4	13.1	21.3	5.3	10.7	5	7.1	16.9	27
0.9	3.9	8.1	3.8	5.4	13	21.1	5	10.2	4.8	6.8	16.1	25.8
1.2	3.9	8.1	3.8	5.4	13	21	4.7	9.7	4.6	6.5	15.4	24.7
1.5	3.9	8.1	3.8	5.4	13	21	5	10.1	4.8	6.8	16.1	25.7
2	3.9	8.1	3.8	5.4	13	21.1	5.6	11.1	5.4	7.4	17.4	27.5
Higgs												
0.4	3.9	8.1	3.8	5.4	13	21.1	4.5	9.2	4.4	6.1	14.7	23.8

eLJ-emuLJ

Table E.4. This table shows the 95% CL upper limit on the number of expected and observed events for various signal benchmarks in the eLJ–emuLJ channel.

Signal benckmarks	$2(s_d \to \gamma_d\gamma_d)$ + X					
γ_d mass [GeV]	Obs.	Exp.	-2σ	-1σ	$+1\sigma$	$+2\sigma$
SUSY						
0.3	6.9	11.0	5.6	7.6	17.0	26.4
0.4	7.3	11.7	5.9	8.0	17.8	27.7
0.5	7.6	11.9	6.0	8.2	18.3	28.4
0.7	6.5	4.5	2.3	3.0	7.0	10.7
0.9	9.3	14.3	7.3	9.9	21.8	32.5
1.2	10.1	14.9	7.8	10.4	22.2	32.7
1.5	12.6	17.3	9.9	13.2	23.3	32.3
2	13.7	17.4	10.7	13.5	23.1	32.0
Higgs						
0.4	5.9	9.7	4.8	6.6	15.0	23.6

muLJ-emuLJ

Table E.5. This table shows the 95% CL upper limit on the number of expected and observed events for various signal benchmarks in the muLJ–emuLJ channel.

Signal benckmarks	$2(s_d \to \gamma_d\gamma_d)$ + X					
γ_d mass [GeV]	Obs.	Exp.	-2σ	-1σ	$+1\sigma$	$+2\sigma$
SUSY						
0.3	8.8	16.5	7.9	11	26.1	41.6
0.4	8.8	16.5	7.9	11	26.2	42
0.5	9	16.8	8.1	11.3	26.6	42.2
0.7	26.1	42.4	19.8	28	54.6	74.4
0.9	10.5	19.3	9.4	12.9	30.6	46.3
1.2	9.3	17.1	8.4	11.6	26.9	42.3
1.5	11.3	20.5	10.1	13.9	31.9	46.8
2	11.2	20.2	10.1	13.8	31	45.6
Higgs						
0.4	11.5	20.8	10.2	14	32.8	47.8

emuLJ-emuLJ

Table E.6. This table shows the 95% CL upper limit on the number of expected and observed events for various signal benchmarks in the emuLJ–emuLJ channel.

Signal benckmarks	$2(s_d \to \gamma_d\gamma_d)$ + X					
γ_d mass [GeV]	Obs.	Exp.	-2σ	-1σ	$+1\sigma$	$+2\sigma$
SUSY						
0.3	2.9	5.1	2.4	3.3	8.4	14.0
0.4	2.9	5.1	2.4	3.3	8.4	14.0
0.5	3.0	5.2	2.4	3.4	8.6	14.2
0.7	3.1	5.4	2.5	3.5	8.8	14.7
0.9	2.9	5.0	2.4	3.3	8.3	13.8
1.2	2.9	5.1	2.4	3.4	8.5	14.1
1.5	2.9	5.0	2.4	3.3	8.4	13.9
2	3.0	5.3	2.5	3.5	8.7	14.4
Higgs						
0.4	3.9	6.1	2.9	4.0	9.0	13.3

REFERENCES

[1] Aad, G. et al. (2008). The ATLAS Experiment at the CERN Large Hadron Collider. *JINST 3*, S08003.

[2] Aad, G. et al. (2013a). A search for prompt lepton-jets in pp collisions at $\sqrt{s} = 7$ TeV with the ATLAS detector. *Phys. Lett. B 719*, 299–317.

[3] Aad, G. et al. (2013b). Search for displaced muonic lepton jets from light Higgs boson decay in proton–proton collisions at with the ATLAS detector. *Physics Letters B 721*, 32–50.

[4] Aad, G. et al. (2013c). Search for WH production with a light Higgs boson decaying to prompt electron-jets in proton–proton collisions at $\sqrt{s} = 7$ TeV with the ATLAS detector. *New. J. Phys 15*, 043009.

[5] Aad, G. et al. (2014). Search for long-lived neutral particles decaying into lepton jets in proton–proton collisions at $\sqrt{s} = 8$ TeV with the ATLAS detector. *JHEP 1411*, 088.

[6] Aalseth, C. et al. (2011). Results from a Search for Light-Mass Dark Matter with a P-type Point Contact Germanium Detector. *Phys. Rev. Lett. 106*, 131301.

[7] Abazov, V. M. et al. (2010a). Search for events with leptonic jets and missing transverse energy in $p\bar{p}$ collisions at $\sqrt{s} = 1.96$ TeV. *Phys. Rev. Lett. 105*, 211802.

[8] Abazov, V. M. et al. (2010b). Search for events with leptonic jets and missing transverse energy in $p\bar{p}$ collisions at $\sqrt{s} = 1.96$ TeV. *Phys. Rev. Lett. 105*, 211802.

[9] Abdo, A. A. et al. (2009). Measurement of the Cosmic Ray $e^+ + e^-$ spectrum from 20 GeV to 1 TeV with the Fermi Large Area Telescope. *Phys. Rev. Lett. 102*, 181101.

[10] Abrahamyan, S. et al. (2011, November). Search for a New Gauge Boson in Electron-Nucleus Fixed-Target Scattering by the APEX Experiment. *Physical Review Letters 107*(4), 191804.

[11] Adam Falkowski, Joshua T. Ruderman, Tomer Volansky, Jure Zupan (2010). Discovering higgs boson decays to lepton jets at hadron colliders. *Physical Review Letters 105*(241801).

[12] Adriani, O. et al. (2009). An anomalous positron abundance in cosmic rays with energies 1.5-100 GeV. *Nature 458*, 607.

[13] Adriani, O. et al. (2010). PAMELA Results on the Cosmic-Ray Antiproton Flux from 60 MeV to 180 GeV in Kinetic Energy. *Phys. Rev. Lett. 105*, 121101.

[14] Agakishievg, G. et al. (2014, April). Searching a dark photon with HADES. *Physics Letters B 731*(4), 265–271.

[15] ALICE Collaboration (2008). The ALICE experiment at the CERN LHC. *Journal of Instrumentation 3*(S08002).

[16] Alwall, J., P. Artoisenet, S. de Visscher, C. Duhr, R. Frederix, et al. (2009). New Developments in MadGraph/MadEvent. *AIP Conf. Proc. 1078*, 84–89.

[17] AMS. AMS Experiment, ams.cern.ch.

[18] AMS Collaboration (2014a, September). Electron and positron fluxes in primary cosmic rays measured with the alpha magnetic spectrometer on the international space station. *Physical Review Letters 113*(121102).

[19] AMS Collaboration (2014b, September). High statistics measurements of the positron fraction in primay cosmic rays of 0.5-500 gev with the alpha magnetic spectrometer on the international space station. *Physical Review Letters 113*(121101).

[20] Angloher, G., M. Bauer, I. Bavykina, A. Bento, C. Bucci, et al. (2012). Results from 730 kg days of the CRESST-II Dark Matter Search.

[21] Archillip, F. et al. (2012, January). Search for a vector gauge boson in ϕ meson decays with the KLOE detector. *Physics Letters B 706*(5), 251–255.

[22] Arkani-Hamed, N. and N. Weiner (2008). LHC Signals for a SuperUnified Theory of Dark Matter. *JHEP 0812*, 104.

[23] Arkani-Hamed, N. and N. Weiner (2009). A Theory of Dark Matter. *Phys. Rev. D 79*, 015014.

[24] ATLAS Collaboration (2010a). The atlas inner detector commissioning and calibration. *Eur. Phys. J. C70*, 787–821.

[25] ATLAS Collaboration (2010b). The atlas level-1 trigger system. *Journal of Physics 396*(012010).

[26] ATLAS Collaboration (2011). Luminosity Determination in *pp* Collisions at $\sqrt{s} = 7$ TeV Using the ATLAS Detector at the LHC. *Eur. Phys. J. C71*, 1630.

[27] Aubert, B. et al. (2009, August). Search for Dimuon Decays of a Light Scalar Boson in Radiative Transitions $\Upsilon \to \gamma A^0$. *Physical Review Letters 103*(18), 081803.

[28] Barwick, S. et al. (1997). Measurements of the cosmic ray positron fraction from 1 to 50 GeV. *Astrophys. J. 482*, L191–L194.

[29] Baumgart, M., C. Cheung, J. T. Ruderman, L.-T. Wang, and I. Yavin (2009). Non-Abelian Dark Sectors and Their Collider Signatures. *JHEP 0904*, 014.

[30] Beach, A. et al. (2001). Measurement of the Cosmic-Ray Antiproton-to-Proton Abundance Ratio between 4 and 50 GeV. *Phys. Rev. Lett. 87*, 271101.

[31] Beringer, J. et al. ((2012)). 2012 review of particle physics. *Phys. Rev. D86 010001.*

[32] Bernabei, R. et al. (2010). New results from DAMA/LIBRA. *Eur. Phys. J. C67*, 39.

[33] Bluemlein, J. and J. Brunner (2011, July). New Exclusion Limits for Dark Gauge Forces from Beam-Dump Data. *Physics Letters B 701*(4), 155–159.

[34] Bluemlein, J. and J. Brunner (2014, April). New Exclusion Limits on Dark Gauge Forces from Proton Bremsstrahlung in Beam-Dump Data. *Physics Letters B 731*(4), 320–326.

[35] Bross, A., M. Crisler, S. Pordes, J. Volk, S. Errede, and J. Wrbanek (1991, November). Search for short-lived particles produced in an electron beam dump. *Physical Review Letters 67*(18), 2942.

[36] Chang, J., J. Adams, H. Ahn, G. Bashindzhagyan, M. Christl, et al. (2008). An excess of cosmic ray electrons at energies of 300-800 GeV. *Nature 456*, 362.

[37] Cheung, C., J. T. Ruderman, L.-T. Wang, and I. Yavin (2010). Lepton Jets in (Supersymmetric) Electroweak Processes. *JHEP 1004*, 116.

[38] CMS Collaboration (2008). The CMS experiment at the CERN LHC. *Journal of Instrumentation 3*(S08004).

[39] CMS collaboration (2011). Search for Light Resonances Decaying into Pairs of Muons as a Signal of New Physics. *JHEP 1107*, 098.

[40] CMS Collaboration (2013). Search for a non-standard-model Higgs boson decaying to a pair of new light bosons in four-muon final states. *Phys. Lett. B 726*, 564–586.

[41] Davier, M. and H. N. Ngoc (1989, October). An Unambiguous Search for a Light Higgs Boson. *Physics Letters B 229*(5), 150–155.

[42] Davoudiasl, H., H.-S. Lee, and M. W. J. (2012, November). Dark side of Higgs diphoton decays and muon $g2$. *Physical Review Letters 86*(5), 095009.

[43] Dent, J. B., F. Ferrer, and L. M. Krauss (2012, January). Constraints on Light Hidden Sector Gauge Bosons from Supernova Cooling. (12).

[44] Dreiner, H. K., J.-F. Fortin, C. Hanhart, and L. Ubaldi (2014, May). Supernova constraints on MeV dark sectors from e^+e annihilations. *Physical Review D 89*(16), 105015.

[45] Endo, M., K. Hamaguchi, and G. Mishima (2012, November). Constraints on hidden photon models from electron $g2$ and hydrogen spectroscopy. *Physical Review Letters 86*(27), 095029.

[46] Englert, F. and R. Brout (1964). Broken symmetry and the mass of the gauge vector mesons. *Physical Review Letters 13*(321).

[47] Essig, R., R. Harnik, J. Kaplan, and N. Toro (2010, December). Discovering new light states at neutrino experiments. *Physical Review D 85*(8), 113008.

[48] Falkowski, A., J. T. Ruderman, T. Volansky, and J. Zupan (2010). Hidden Higgs Decaying to Lepton Jets. *JHEP 1005*, 077.

[49] Forum, A. S. Abcd method in searches. `https://twiki.cern.ch/twiki/pub/AtlasProtected/ATLASStatisticsFAQ/ABCD.pdf`.

[50] Gninenko, S. N. (2012, July). Constraints on sub-GeV hidden sector gauge bosons from a search for heavy neutrino decays. *Physical Letters B 713*(9), 244–248.

[51] Griffiths, D. (2008). *Introduction to Elementary Particles* (Second edition ed.). Wiley-VCH.

[52] Higgs, P. (1964). Broken symmetries and the masses of gauge bosons. *Physical Review Letters 13*(508).

[53] Hoekstra, H., M. Franx, K. Kuijken, R. Carlberg, and H. Yee (2003). Lensing by galaxies in cnoc2 fields. *Royal Astronomy Society 340*.

[54] Holdom, B. (1986). Two U(1)'s and ϵ Charge Shifts. *Phys. Lett. B166*, 196.

[55] Lees, J. P. et al. (2014, November). Search for a dark photon in e^+e^- collisions at BABAR. *Physical Review Letters 113*(11), 201801.

[56] LHCb Collaboration (2008). The LHCb Detector at the LHC. *Journal of Instrumentation 3*(S08005).

[57] M. Markevtick, A. H. Gonzalez, D. Clowe, A. Vikhlinin, W. Forman, C. Jones, S. Murray and W. Tucker (2004). Direct constraints on the dark matter self-interaction cross section from the merging galaxy cluster 1e 0657–56. *The astrophysical journal 606*, 819–824.

[58] Merkel, H. et al. (2011, June). Search for Light Gauge Bosons of the Dark Sector at the Mainz Microtron. *Physical Review Letters 106*(22), 251802.

[59] NASA. Bullet cluster, http://apod.nasa.gov/apod/ap080823.html.

[60] PAMELA. PAMELA experiment, http://pamela.roma2.infn.it/index.php.

[61] Planck collaboration (2014). Planck 2013 results. i. overview of products and scientific results. *Astronomy and Astrophysics 571*(A1), 48.

[62] Pospelov, M. (2009, November). Secluded U(1) below the weak scale. *Physical Review D 80*(2), 095002.

[63] Reece, M. and L.-T. Wang (2009). Searching for the light dark gauge boson in GeV-scale experiments. *JHEP 0907*, 051.

[64] Riordan, E. M. et al. (1987, August). Search for short-lived axions in an electron-beam-dump experiment. *Physical Review D 59*(17), 755.

[65] Solodov, E. P. (2010). Study of the e^+e^- to hadrons via isr at babar.

[66] The ATLAS Collaboration (2014, August). Performance of the ATLAS muon trigger in pp collisions at sqrts = 8 TeV. *CERN-PH-EP-2014-154* (14).

[67] Vera C Rubin, W Kent Ford, Norbert Thonnard (1980). Rotational properties of 21 sc galaxies with a large range of luminosites and radii, from ngc 4605 (e=4kpc) to ugc 2885 (r=122kpc). *The astrophysical journal 238*, 471–487.

[68] Zwicky, F. (1937, October). On the masses of nebulae and of clusters of nebulae. *Astrophys. J. 86*, 217.

VITA

Harisankar Namasivayam was born in India. After completing his schooling at Santhome Higher Secondary School in Chennai, India, he joined KCG college of Technology majoring in Electronics and Communications. He earned his Bachelor of Engineering degree from Anna University in the year 2006. During the next two years he worked as a Hardware design engineer at L&T infotech. In the year 2009 he joined the physics graduate school at The University of Texas at Dallas.